APPROVAL SHEET

Title of Dissertation: SPATIAL AND FUNCTIONAL ANALYSIS OF MEMBRANELESS ORGANELLES IN GLUCOSE METABOLIC NETWORK USING LIGHT SHEET MICROSCOPY

Name of Candidate: Erin L. Kennedy
Doctor of Philosophy, 2021

Dissertation and Abstract Approved: _____
Dr. Minjoung Kyoung
Associate Professor
Department of Chemistry and Biochemistry

Date Approved: _____

NOTE: *The Approval Sheet with the original signature must accompany the thesis or dissertation. No terminal punctuation is to be used

ABSTRACT

Title of Document: SPATIAL AND FUNCTIONAL ANALYSIS OF MEMBRANELESS ORGANELLES IN GLUCOSE METABOLIC NETWORK USING LIGHT SHEET MICROSCOPY

Erin L. Kennedy, Doctor of Philosophy, 2021

Directed By: Dr. Minjoung Kyoung, Department of Chemistry and Biochemistry

Metabolic enzymes can arrange into multi-enzyme complexes which regulate metabolic processes. In the glucose metabolism, this multi-enzyme complex has been termed the 'glucosome'. Recently, glucosomes have been reported to direct glucose flux into various other pathways in live human cells, with small-sized glucosomes directing the metabolism through the entirety of glycolysis. However, projected images generated by conventional microscopies are limited in detecting the small-sized glucosomes due to the contrast of the glucosomes against a projected background. Therefore, we have utilized 3-dimensional lattice-light sheet microscopy to observe glucosomes in live cells with better spatial resolution. This analysis led to the characterization of relative density inside of glucosomes which determined that the characteristic concentration of one enzyme, phosphofructokinase-liver type, was dependent on the size of the glucosome, but another enzyme, pyruvate kinase (isoform 2) was independent of size. To better understand the formation of glucosomes, exposing the cells to increased osmotic pressure resulted in an increase in glucosomes via liquid phase separation. With increased osmotic pressure, the quantity and size of glucosomes increased, leading us to conclude that glucosomes are formed through liquid-liquid phase separation and may have an internal structure provided by the oligomeric PFKL. The 3D lattice light sheet microscope also allowed us to observe that a significant portion of glucosomes were in subcellular proximity to the surface of mitochondria. Furthermore, disruptions to the mitochondrial metabolism dramatically affected the small glucosomes that were in proximity with the surface of the mitochondria, demonstrating the functional and spatial relationship shared between glucosomes and mitochondria metabolic compartments. While larger glucosomes were statistically retained, the quantity of small glucosomes associated with the surface of mitochondria were reduced more than 50% when cells were treated with a mitochondria oxidative phosphorylation inhibitor, demonstrating that the physical characteristics of glucosomes are related to their metabolic function inside of cells. Next, glucosomes that were not in proximity to the mitochondria were evaluated for their spatial coordination with another subcellular compartment. The glucosomes were analyzed to observe a high spatial proximity with both microtubules

and actin in the cytoskeleton. Larger and small glucosomes were readily associated with the cytoskeleton, which suggests that glucosomes are regulated in a size-dependent matter with other metabolic pathways. Collectively, this work demonstrates a method to spatially analyze the subcellular proximity of metabolic compartments and provides consistent findings that the glucosome metabolic compartment directs glucose flux in a size-dependent manner.

SPATIAL AND FUNCTIONAL ANALYSIS OF MEMBRANELESS ORGANELLES IN GLUCOSE METABOLIC NETWORK USING LIGHT SHEET MICROSCOPY

By

Erin L. Kennedy

Dissertation submitted to the Faculty of the Graduate School of the
University of Maryland, Baltimore County, in partial fulfillment
of the requirements for the degree of
Doctor of Philosophy
2021

Dedication

To my family that encouraged the importance of education.
To my spouse, Scott, for a cherished home and continuous warmth.
To my grandmothers, Joyce and Greta, who showed me talent is practiced.
To my grandfathers, Robert and James, who seek to answer struggle with a kind heart.
To my parents, Beth and James, that look for opportunity in all aspects of life.
To Sewell and Kathy, my godparents that taught me patience and perseverance.
To my sibling, Ethan, who has kindly believed in me.
To my dear friends, Kady, Patricia, Miji, and Mirelis for keeping the light in my spirit.

Acknowledgements

For support and training of advanced microscopy techniques throughout my dissertation, I would like to thank my advisor, Dr. Minjoung Kyoung. I wish you well in the rest of your tenured career; thank you and congratulations.

To the collaborating lab that trained me in cell culture and other critical techniques, I would like to thank Dr. Songon An and all lab members.

I wish to acknowledge all members of my dissertation committee: Dr. Rachel Brewster, Dr. Marie-Christine Daniel, Dr. Brian Cullum, Dr. Ryan White, Dr. James Fishbein. And for critical help with graduation processes I would like to thank the following administrative staff: Ms. Patricia Gagne, Ms. Justine Johnson, Ms. Nicole Mooney, Ms. Ramona Patel.

I would like to thank all previous and current labmates for their dedication to the projects and feedback: Danielle, Miji, Prakash, Krishna, Noah, Tao, Patricia, Haotian, Spencer, Ashesh, Chen, Sarah, Kristen, Lauren, Vanessa, Chidera, Blake, Anthony, Farhan, Manuel, Asfand, Keynon, Syrena, Rose, Michelle, and Jayo.

I would like to thank the Meyerhoff Graduate community, namely Ms. Justine Johnson and I would like to thank the Indigenous community, namely the BAIC during my life in Baltimore.

Thank you to everyone that has seen me through my education.

Table of Contents

Dedication ii
Acknowledgements iii
Table of Contents iv
List of Figures vi
Chapter 1 vi
Chapter 2 vi
Chapter 3 vi
Chapter 4 vi
Chapter 5 vi
Chapter 6 vii
List of Abbreviations viii
Chapter 1: Enzymes organize into subcellular compartments to perform specific functions 1
1.1 Introduction 1
1.2 Mitochondria: A subcellular compartment for metabolism 1
1.3 Membraneless compartments responsively form to meet demands of the cell 2
1.4 Enzymes in the glucose metabolism 3
1.5 Mitochondrial influence on glucose metabolism in cancer cells 5
1.6 Visualizing membraneless condensates with microscopy 5
1.7 Discussion 6
Chapter 2: 3-Dimensional visualization of the glucose metabolism compartment in living cells 8
2.1 Introduction 8
2.2 Materials and Methods 9
2.2.1 Materials 9
2.2.2 Cell culture and transfection 9
2.2.3 Fluorescence lattice light sheet live cell imaging 10
2.2.4 Assembly size analysis 14
2.3 Results 14
2.3.1 The spatially distinct glucose metabolic assembly includes multiple enzymes of the glucose metabolism 14
2.4 Discussion 18
Chapter 3: Glucosomes form through liquid-liquid phase separation 19
3.1 Introduction 19
3.2 Materials and Methods 22
3.2.1 Increasing osmotic pressure in live cells 22
3.2.2 Glucosomes size analysis with 3-dimensional datasets 22
3.2.3 Fluorescence live cell widefield imaging 22
3.3 Results 23
3.3.1 Widefield population studies showed an increase

to osmotic pressure 23
3.3.2 Lattice light sheet quantification of PFKL inside glucosomes 26
3.3.3 Fusion of glucosomes does not increase the concentration of PFKL within glucosomes 28
3.4 Discussion 30
Chapter 4: High partition coefficient supports that the glucosomes have an internal structure utilizing oligomeric phophofructokinase-1 31
4.1 Introduction 31
4.2 Methods and Materials 31
4.2.1 Partition ratio analysis 31
4.3 Results 32
4.3.1 Phosphofructokinase-1 strongly partitions into liquid-liquid phase separated glucosomes in live cells 32
4.3.2 Small size glucosomes were found to have reduced PFKL partition ratio 35
4.4 Discussion 37
Chapter 5: Glucosomes have a spatial and functional relationship with the mitochondria 38
5.1 Introduction 38
5.2 Methods and Materials 42
5.2.1 Using MitoTracker™ to label cells 42
5.2.2 Treatment with small molecules to disrupt the mitochondria and glucose metabolisms 42
5.2.3 3D spatial analysis 42
5.2.4 Glucosome volume and density analysis 45
5.2.5 Knockdown of hexokinase isoform 2 in Hs578T cells 45
5.3 Glucosomes were found to be spatially associated with the mitochondria 46
5.3.1 Subcellular regions of interest had distinct glucosome behaviors 50
5.4 Small glucosomes in the mitochondria-dense regions of the cell were functionally associated with the mitochondria 52
5.5 Discussion 57
Chapter 6: Future Direction 58
6.1 Glucosomes are spatially associated with the cytoskeleton 58
Chapter 7: Concluding Remarks 63
Appendix 65
Bibliography 88

List of Figures

Chapter 1

Figure 1: Glucose metabolism

Chapter 2

Figure 2: The lattice light sheet microscope for 3-dimensional fluorescence imaging

Figure 3: Colocalization of glucose metabolism enzymes using 3-dimensional datasets showing formation into a subcellular compartment known as the glucosome

Figure 4: No colocalization with other metabolic compartments showing glucosomes are pathway specific metabolic compartments

Chapter 3

Figure 5: A phase diagram for glucosomes which form via liquid-liquid phase separation as modeled by their increased formation during increased osmotic pressure

Figure 6: Phase separation drives the formation of glucosomes using two means of increased osmotic pressure

Figure 7: Increased osmotic pressure and the increased partitioning of PFKL into glucosomes

Figure 8: The characteristic concentration of PFKL remains constant with respect to glucosome volumes

Chapter 4

Figure 9: The partition coefficient of PFKL is larger than the partition coefficient of PKM2

Figure 10: A size-dependent ratio of the partition coefficients of PFKL compared to PKM2 shows that small sizes of glucosomes have a different compositional ratio

Chapter 5

Figure 11: Diagram of the targeted functional connections between the glucose metabolism and mitochondria

Figure 12: Diagram of 3-dimensional cellular heterogeneity and the 3-dimensional vector space data obtained with lattice light sheet microscopy

Figure 13: Histogram showing the edge-to-edge distance bins of glucosomes to the nearest mitochondria which show different population behaviors depending on subcellular locations into mitochondria-dense or mitochondria-sparse regions of interest

Figure 14: Example of subcellular regions showing mitochondria-dense and mitochondria-sparse regions of interest

Figure 15: Subcategorizing glucosomes based on their physical volume showing small-sized glucosomes are more readily associated with the surface of mitochondria, especially in mitochondria-dense regions of interest

Figure 16: Metabolic disruptions using Oligomycin A to disrupt oxidative phosphorylation or a pyruvate dehydrogenase complex inhibitor show decrease in glucosomes in a population of cells

Figure 17: The impact of oligomycin treatment is primarily targeting glucosomes that are associated with the mitochondria, primarily within the mitochondria-dense region

Figure 18: Knockdown of HK2 expression within cells shows a phenotype change in glucosome formation where small glucosomes are decreased and larger glucosomes are more readily associated with the mitochondria

Chapter 6

Figure 19: Histogram of the edge-to-edge distance of glucosomes showing a strong association to the cytoskeleton organelles, microtubules or actin

Figure 20: 3-channel histogram of the edge-to-edge distance of glucosomes, mitochondria, and microtubules or actin showing that glucosomes are almost entirely associated with one of these organelles within live cells

List of Abbreviations

HK2:	hexokinase isoform 2; an enzyme in the glucose metabolism
PFKL:	phosphofructokinase, liver type; an enzyme in the glucose metabolism
PKM2:	pyruvate kinase isoform 2; an enzyme in the glucose metabolism
FBPase:	fructose 1,6-bisphosphatase; an enzyme in the glucose metabolism
mEGFP:	a monomeric green fluorescent protein
mCherry:	a monomeric red fluorescent protein
TC:	tetracycsteine: Sequence of amino acids in format of CCxxCC
ReAsH:	Lumio Red; membrane-permeable fluorescent probe that binds TC sequences
FGAMS:	phosphoribosylformylglycinamidine synthase; an enzyme in the *de novo* purine biosynthesis
LLSM:	lattice light-sheet microscopy
P.C.:	partition coefficient
FRET:	fluorescence resonance energy transfer
FRAP:	fluorescence recovery after photobleaching
ROI:	region of interest defined by physical boundaries
PEG: polymer	polyethylene glycol; cell membrane impermeable, biocompatible
ATP:	adenosine triphosphate; energy-carrying molecule in cells
PDC:	pyruvate dehydrogenase complex; complex of enzymes that converts pyruvate into acetyl-coA
SEM:	standard error of the mean; standard deviation divided by square root of sample size

Chapter 1: Enzymes organize into subcellular compartments to perform specific functions

1.1 Introduction

Throughout the cell, the harmonious regulation of metabolic pathways keeps the cell progressing from division to apoptosis through the flux of metabolites. Metabolic networks are the orchestration of all the metabolic processes in an ever-changing flux within the cell. The proteins that are responsible for performing these metabolic processes are sometimes able to organize into distinct subcellular regions. While these regions are specific to their function, there is also a need for intracellular coordination of metabolic processes which may be observed as a spatial coordination between one or more metabolic compartments. Since diseases are largely related to dysregulated metabolisms, the study of spatial coordination of metabolic compartments can hold new insight for disease therapies. Advancements in the field of 3-dimensional microscopy offers an exciting means to study the functional regulation of the cellular network in living cells with regards to spatial coordination of metabolic compartments.

1.2 Mitochondria: A subcellular compartment for metabolism

The subcellular space of a cell is heterogenous and sectioned into compartments with specified functions. Membrane-bound organelles like the mitochondria utilize compartmentalization to improve production by maintaining the optimal environment specific to their functions (Avalos et al., 2013). With increased production, mitochondria are a hub for metabolic processes. They have been observed to use contact sites to communicate with other organelles to support many cellular functions (Senda and Yoshinaga-Hirabayashi, 1998; Perkins et al., 2001; Lackner, 2019). Some

of these mitochondrial contact sites impact Ca^{2+} transfer and fatty acid trafficking which are linked to resisting apoptosis showing a network that coordinates cellular metabolic processes (Rambold et al., 2015; Rizzuto et al., 1998; Brdiczka et al., 2006). The benefit of subcellular compartmentalization is conserved energy through substrate channeling, or the streamlined production of biomolecules (Hult and Berglund, 2007; Hinzpeter et al., 2017). Since membrane-bound compartments require resources to form and maintain their structure, it is no surprise that other pathways utilize compartmentalization even without the presence of a membrane.

1.3 Membraneless compartments responsively form to meet demands of the cell

Membraneless compartments can perform their processes without the need for a physical barrier which makes it easier for them to form and dissociate as needed by the cell (Aguilera-Gomez and Rabouille, 2017). Membraneless compartments are considered a type of biomolecular condensate, which are distinguishable by a concentration gradient that defines the boundaries of the condensate (Banani et al., 2017). Condensates can respond quickly to changes in physical environments like pH, ion concentrations, and osmotic pressure. They also freely go through mobile processes like fusion and fission (Wei et al., 2020). In some cases, the membraneless compartments assemble to perform a metabolic process that benefits cellular demand (Kojima and Takayama, 2018; Schmitt and An, 2017). The glucose metabolism is highly utilized by cells and the cytosolic enzymes have been observed to reversibly form into multi-enzyme complexes that can content-exchange with the surrounding cytoplasm (Kohnhorst et al., 2017; Jang et al., 2020).

1.4 Enzymes in the glucose metabolism

The glucose metabolism includes two pathways that flux between the production of pyruvate through glycolysis or the production of glucose through gluconeogenesis. The glucose metabolism is central to respiration, making metabolic building blocks, and progressing through the cell cycle (Cai & Tu, 2012; Kalucka et al., 2015; Lee & Finkel, 2013). The enzymes in the glucose metabolism work to process intermediates through the pathways of glycolysis and gluconeogenesis which are then utilized in the production of adenosine triphosphate (ATP) or in other crucial metabolic pathways (De Santis et al., 2018). Since the regulation of the glucose metabolism is essential to many facets of the cell, the study of glycolytic enzymes and how they direct metabolic flux has great biological significance. Rate-limiting enzymes are thought to be an important target in correcting the dysregulated glucose metabolism in cancer cells (Sun et al., 2021). The glycolysis pathway includes rate-limiting enzymes such as hexokinase, phosphofructokinase 1, and pyruvate kinase (Fig. 1). In gluconeogenesis the rate-limiting enzymes are pyruvate carboxylase, phosphoenolpyruvate carboxykinase, fructose 1,6-bisphosphatase, and glucose 6-phosphatase (Fig. 1). Altogether, there is expansive correlation between the control of the glucose metabolic enzymes and the growth of cancer cells. Understanding the glucose metabolism and the response to dysregulated cellular metabolic demands will lead to great therapeutic strategies against cancer. However, the ability for mitochondria to rescue the cell after glycolysis is blocked shows a possibility of a robust and responsive metabolic network in cancer cells.

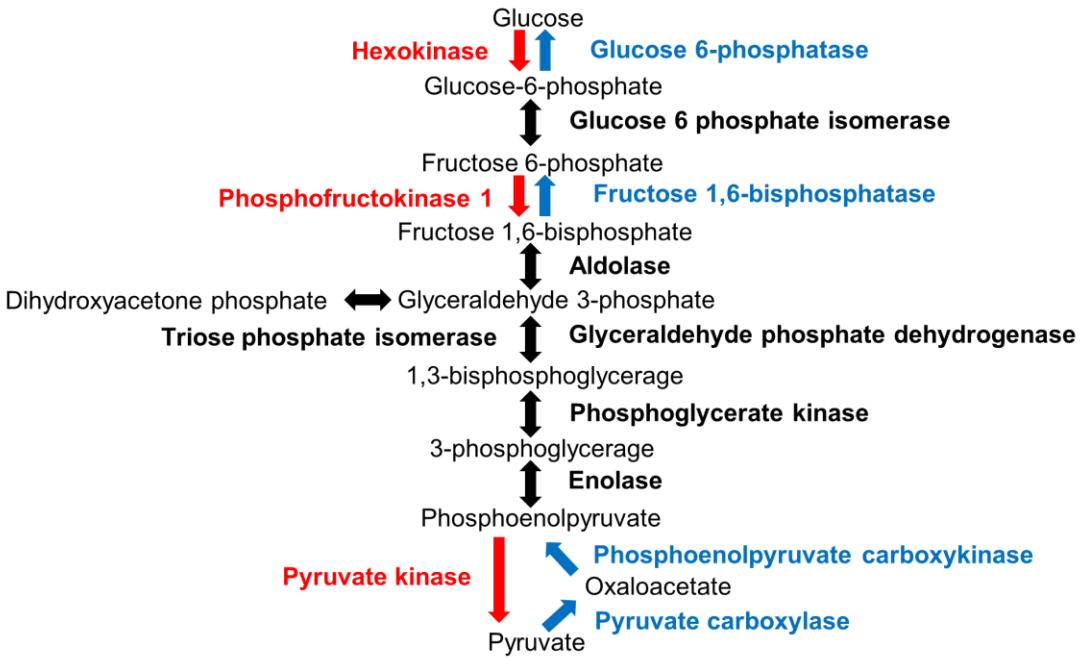

Figure 1: Glucose metabolism. Glycolysis shown as the pathway from glucose to pyruvate, with rate-limiting enzymes shown in red. Gluconeogenesis shown as the pathway from pyruvate to glucose, with rate limiting enzymes shown in blue. Reversible enzymes denoted by black double-directional arrows. Metabolites written in plain text.

1.5 Mitochondrial influence on glucose metabolism in cancer cells

Cancer cells produce significant amounts of ATP through glycolysis in the cytoplasm, however mitochondria are still necessary for supplying building blocks of cell proliferation (Birsoy et al., 2015; Sullivan et al., 2015). Cancer cells adapt to utilize both glycolysis and oxidative phosphorylation as sources of energy depending on the fluctuating cellular conditions (Corbet et al., 2016). Some cancers have an elevated mitochondrial transmembrane potential preventing cell death through toxic microenvironmental conditions (Zhang et al., 2019). This increased coordinated resistance to apoptosis includes higher glycolytic rates which shows a close regulatory link between mutual glycolysis and mitochondrial dysregulation (Bonnet et al., 2007). Cancer cell survival relies heavily on coordination between the glucose metabolism and mitochondria. By visualizing the spatial relationship between the glucose metabolism and mitochondria, additional functional cancer targets may be elucidated.

1.6 Visualizing membraneless condensates with microscopy

Due to the temporal nature of biomolecular condensates, studies of membraneless assemblies utilize live-cell imaging techniques (Alberti et al., 2019; Shakya and King, 2021). As shown by recent studies using the spatial and temporal resolution of live-cell fluorescence imaging, membraneless organelles were observed as they were regulated by membrane-bound organelles (Lee *et al.*, 2020; French *et al.*, 2016). Taken together, metabolic pathways can benefit from the organization into temporary exclusive subcellular compartments that also are able to communicate with organelles, leaving a large field of subcellular metabolic coordination open for study. Advancements in the field of microscopy have led to methodologies that can obtain 3-

dimensional high-spatial resolution and fast temporal resolution images of live cancer cells (Juette et al., 2008; Shao et al., 2011; Chen et al., 2014). Fluorescence microscopy is a versatile technique, especially for observation of live cells and proteins, but the spatial resolution is limited by the properties of light (Bunt and Wouters, 2004; Sednev et al., 2015; Huang et al., 2010). The improvements of super-resolution techniques can increase the spatial resolution beyond the diffraction limit, but the detrimental aspect of super-resolution imaging is that these techniques are often temporally limited and increase photoxicity to the cell, making them less ideal for studies of live cells and stress-sensitive metabolic pathways (Weiss 2000; Huang et al., 2010; Chen et al., 2014). The lattice light sheet microscope (LLSM) offers the best combination of low-photoxicity, 3-dimensional imaging, speed, and spatial resolution (Chen et al., 2014). LLSM provides an optimal means to study the spatial relationships of multiple metabolic pathways in live cells as they undergo metabolic processes.

1.7 Discussion

Individual metabolic pathways coordinate with each other, but the dysregulation of metabolic pathways is a major contributor to disease so there is a terrific need to study the coordination of metabolic networks inside of cells. The dysregulation of the glucose metabolism coordinates with the mitochondria metabolism to resist apoptosis in cancer cells providing support that a functional link is present between the metabolisms. Thus far, the spatial coordination of these metabolisms has not been detailed. Herein, we utilize fluorescence live-cell imaging to characterize glucose metabolic enzymes formed into spatially distinct compartments with the purpose of driving glycolytic flux in cancer cells. Further, we demonstrate that

the glucose metabolic compartments are spatially and functionally linked with the mitochondria by quantifying the spatial relationship from 3-dimensional fluorescence microscopy methodologies. Altogether, this provides insight and instruction into observing metabolic networks and the mechanisms of cancer-specific responses between the glucose metabolism and mitochondria.

Chapter 2: 3-Dimensional visualization of the glucose metabolism compartment in living cells

2.1 Introduction

The antiparallel glycolysis and gluconeogenesis pathways include intermediates that supply building blocks to other metabolic processes such as adenosine triphosphate (ATP) used to supply energy for the cell. For this reason, when cells are proliferating in an uncontrolled manner, the demand for rapid ATP generation as well as other building blocks increases (Zhao et al, 2010; Grasmann et al. 2019). Additionally, cancer-specific mutations have altered the enzymes within the glucose metabolism leading to a change in metabolic flux, lending importance to the study of glucose metabolic enzymes in disease states (Christofk et al., 2008; Vander Heiden et al., 2011; Israelsen et al., 2013). While the glucose metabolism intermediates and enzymes are well-established, the mechanism of coordination for the metabolic pathway was unclear. Multiple studies *in vitro* have shown the formation of glucose metabolism enzymes into a membraneless assembly (Giegé et al., 2003; Ginger et al., 2010; Graham et al., 2007; Mamczur et al., 2005, 2007; Mowbray & Moses, 1976; Pette et al., 1962; Srere, 1987; Sullivan et al., 2003; Wan et al., 2015; Wang et al., 1997). To determine if the same membraneless assembly occurred in live human cells, enzymes within the glucose metabolism were labeled for fluorescence imaging and it was determined that the cytosolic and rate-limiting enzymes of the glucose metabolism colocalized into a multi-enzyme assembly (Kohnhorst et al., 2017). In this chapter, evidence supporting the functional compartmentalization of glucose metabolic

enzymes in live cells is provided. Strong colocalization of enzymes in the glucose metabolism were confirmed in 3D using lattice light sheet fluorescence imaging.

2.2 Materials and Methods

2.2.1 Materials

The cDNAs of the human enzymes involved in glucose metabolism were acquired from the PlasmID Repository, the DNA Resource Core at Harvard Medical School. Most cDNAs, except for the plasmids expressing EGFP-tagged hexokinases (Addgene), were amplified by PCR using *Pfu* DNA polymerase (Stratagene) with pairs of restriction sites on primers. Subsequently, the genes were cloned into either a pmEGFP-N1 plasmid, which possesses an A206K mutation in the EGFP sequence of pEGFP-N1 (Clontech) to produce mEGFP. The resulting cloned plasmids were confirmed by restriction enzyme digestions and DNA sequencing (GeneWiz). In addition, a TC motif of six amino acids (N-CCPGCC-C) was introduced to PFKL-mEGFP, resulting in PFKL-TC-mEGFP and PFKL-TC. Site-directed mutagenesis was also used to either abolish or mimic reported lysine acetylation sites on human PFKL, FBPase, and PKM2. Additionally, the cDNA of PFKL was cut via restriction enzymes from the PFKL-mEGFP construct and inserted into the pmCherry-N1 plasmid expressing the monomeric mCherry red fluorescent protein (mCherry). The following constructs were used in live-cell fluorescence microscopy: liver type phosphofructokinase 1 (PFKL-mEGFP, PFKL-mCherry), liver type fructose 1,6-bisphosphatase (FBPase-mEGFP), pyruvate kinase M2 (mEGFP-PKM2).

2.2.2 Cell Culture and transfection

Human breast carcinoma Hs578T (HTB-126) cell lines were obtained from the ATCC. Hs578T cells were maintained in the RPMI 1640 (Mediatech, Cat # 10-31 040-CV) supplemented with 10% dFBS (Atlanta Biological, Cat # S12850) and 50 µg/ml gentamycin sulfate. Hs578Bst cells were maintained as recommended in Hybri-Care medium (ATCC, Cat # 46-X) supplemented with 1.5 g/liter NaHCO3, 10% FBS, 30 ng/ml mouse EGF (Sigma), and 50 µg/ml gentamycin sulfate. The cells were maintained in a HeraCell CO2 incubator (37 °C, 5% CO2, and 95% humidity). To prepare cells for transfection and subsequent imaging, Hs578T cells were gently removed from the culture flask by replacing the culture medium with trypsin-EDTA (Corning, Cat # 25-053-Cl). Fresh, antibiotic-free growth medium was subsequently used to harvest and resuspend cells that were used to plate either glass bottomed 35-mm Petri dishes (MatTek) or 8-well chambers (LabTek) such that next day confluency was ~70–90%. If 3D imaging was performed using lattice light sheet microscopy, additional 5mm round glass coverslips were added to the MatTek dishes. The following day, the cells were transfected with Lipofectamine 2000 (Invitrogen). For dual transfection, the two plasmids were used in the same transfection mixture whether using Lipofectamine 2000. When using Lipofectamine 2000, the Opti-MEM-I reduced serum medium (Opti-MEM-I; Gibco, Cat # 11058) was used for transfection, but the medium was exchanged with fresh antibiotic free growth medium after a 5 h incubation (37 °C, 5% CO2, and 95% humidity), followed by ~18–24 h of incubation in the incubator.

2.2.3 Fluorescence lattice light sheet live cell imaging

For lattice light sheet imaging: on the day of imaging (~18-24 h post-transfection), the cells were washed with buffered-saline solution for three 10 minute incubations followed by a ~1-2-h incubation at ambient temperature. Additionally, 100-200-nm TetraSpeck^{TM} Fluospheres (Invitrogen) were added to the incubating cell dishes to ensure perfect overlap in all three imaging dimensions. The lattice light sheet microscope was assembled from the design in the publication of Eric Betzig's lab (Chen *et al*., 2014). Several key points are critical to the functionality of the LLSM (Fig. 2) including: multiple laser channels to observe different fluorophores, cylindrical lenses to shape the circular Gaussian laser beam into a rectangular Gaussian beam, a spatial light modulator and annular mask to create the non-diffracting lattice of Bessel beams, and orthogonally placed objectives at the sample chamber to capture 3-dimensional datasets with reduced background illumination. Modifications to the original published lattice light sheet microscope include the addition of flipping blockers at the laser sled to block stray light, and the use of a filter wheel prior to the Orca Flash camera which can be exchanged with multiple filters to best match each fluorophore. The LLSM provides sub-diffraction-limited spatial resolution in the z-dimension, reduced phototoxicity to the sample, and captures 3-dimensional datasets of the subcellular space. The lattice light sheet microscope was aligned by centering the laser beams on a single Bessel beam pattern at the surface of the spatial light modulator and then centering that patten through the annular mask. Minor adjustments were made to objectives so that the sheet of latticed Bessel beams was orthogonal with the detection objective. A point spread function was obtained daily by using TetraSpeck^{TM} microspheres and moving the detection objective and illumination

planes simultaneously. The samples were moved through the stationary illumination plane using a piezo stage. The angle between the sample stage movement and detection plane was calculated and used to deskew the image using a Matlab code designed by the Betzig Lab (Chen et al., 2014). Additionally, 20 iterations of Richardson-Lucy deconvolution were applied to the image to better resolve the image quality without introducing artifacts to the sample, also detailed in the Matlab code designed by the Betzig Lab (Chen et al., 2014). Output images were obtained in 32-bit format and were compressed to 16-bit using ImageJ software for processing.

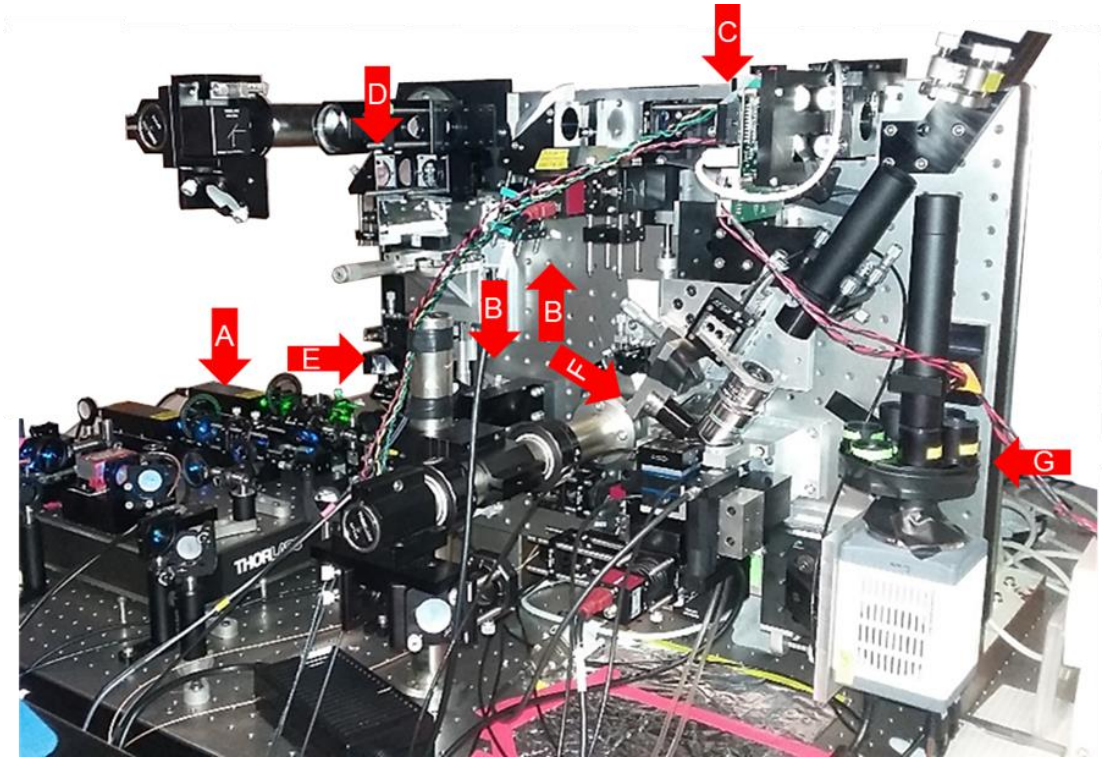

Figure 2: The home-built 3-dimensional lattice light sheet fluorescence imaging microscope. The lasers (A) output a circular Gaussian beam which is then stretched into a rectangular shape through a series of cylindrical lenses (B). The rectangular beam of illumination is then patterned by the spatial light modulator (C) and the selection of first order diffraction by the annular mask (D) forms the final lattice of Bessel beams which are steered by a galvo mirror (E) into the sample chamber (F). Modifications to the microscope in the original publication (Chen et al., 2014) include flip-blocks (not shown in picture) in the individual laser pathways to block stray illumination and a filter wheel (G) prior to the Orca Flash camera which can be exchanged to match the fluorophores of interest.

2.2.4 Assembly Size Analysis

For lattice light sheet imaging, glucosomes were isolated using the 3D Objects Counter plugin in Image J using multiple thresholds to obtain segmentation without artifacts. Colocalization of glucose metabolism enzymes was evaluated using the JACoP and Coloc2 plugins and resulting Pearsons' coefficients.

2.3 Results

2.3.1 The spatially distinct glucose metabolic assembly includes multiple enzymes of the glucose metabolism

Widefield imaging using FBPase-mEGFP, mEGFP-PKM2, and PEPCK1-mEGFP cotransfected with PFKL-mOFP showed formation of colocalized compartments in the cytosol of live Hs578T cells (Kohnhorst et al., 2017). This colocalization was further demonstrated using 3-dimensional microscopy to observe cells cotransfected with mEGFP-PKM2 and PFKL-mCherry, or cotransfected with mEGFP-PKM2 and PFKL-TC-ReAsH. Colocalization was completed using the Coloc2 plugin through ImageJ (Fiji, NIH). Colocalization previously showed strong compartmentalization of multiple glucose metabolic enzymes using 2-dimensional images (Kohnhorst et al., 2017). The degree of colocalization can also be determined using 3D datasets acquired through lattice light sheet imaging (Fig. 3) (An et al., 2021). As a comparison to previous colocalization methods, the dataset of the cell acquired using lattice light sheet microscopy was projected along the z-axis to form a 2-dimensional projection image much like captured by widefield microscopy methods. Colocalization analysis showed that the colocalization between PKM2 and PFKL was high for both the projected and 3-dimensional datasets due to the Pearson's R value

which was close to 1.0, or the level of perfect colocalization. The vastly larger number of voxels in the 3-dimensional dataset did not affect the finding of colocalization, which validates the use of colocalization programs on LLSM datasets.

It is necessary to confirm that the glucosomes are spatially distinct from other cellular bodies to support the findings that the formation of glucosomes is for the regulation of the glucose metabolism. A lack of colocalization between the glucosomes and the other cellular bodies, such as stress granules or aggresomes was confirmed using 2D widefield microscopy (Kohnhorst et al., 2017). Additionally, Coloc2 analysis yielded a Pearson's R value of 0 for the 3-dimensional dataset comparing glucosomes (PFKL) with purinosomes (FGAMS), another distinct subcellular metabolic compartment (Fig. 4). A lack of colocalization with other metabolic pathways supports the findings that glucosomes form exclusive metabolic compartments for the purpose of glucose flux regulation in cells (Kohnhorst et al., 2017; Jeon et al., 2018).

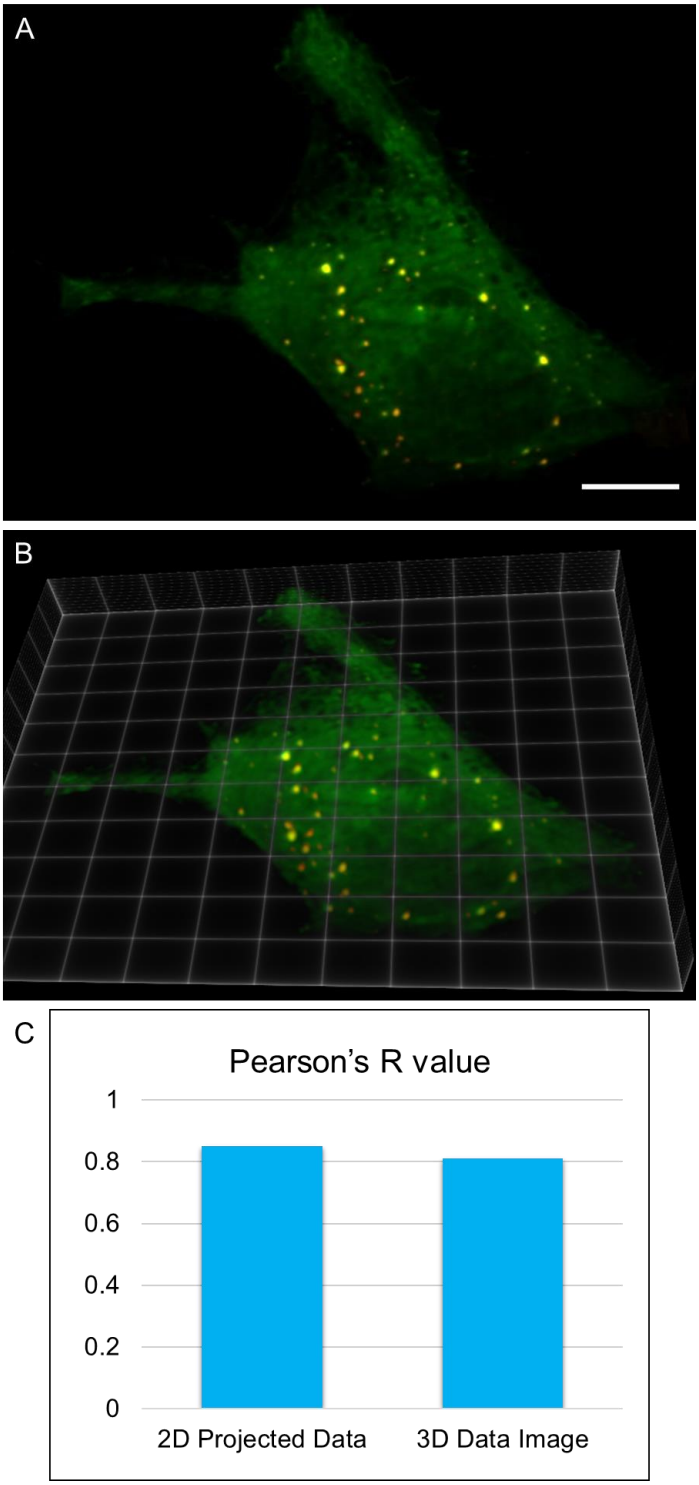

Figure 3: (modified from An et al., 2021) Colocalization of enzymes in the glucose metabolism into cytoplasmic compartments mEGFP-PKM2 (green) and PFKL-mCherry (red) cotransfected in live Hs578T cells. The 2-dimensional projection (A) compared against 3-dimensional dataset (B) of the same cell shows similar Pearson's R value (C) and the high colocalization of PFKL and PKM2 enzymes in both datasets. Scale bar represents 10 μm.

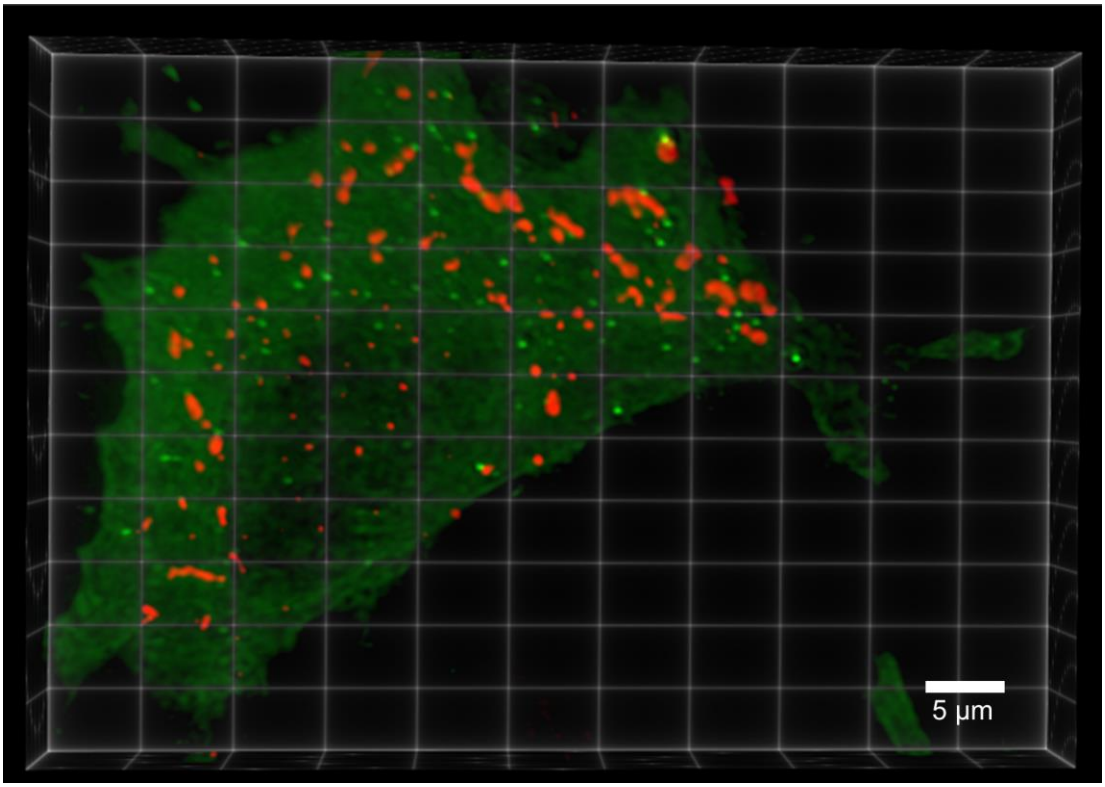

Figure 4: No colocalization of enzymes in the glucose metabolism with other established subcellular compartments. Lattice light sheet imaging of FGAMS-mEGFP (green channel) representing purinosomes and PFKL-TC-ReAsH (red channel) representing glucosomes. Scale bar represents 5 µm.

2.4 Discussion

This work provides visual evidence of the exclusive nature of the subcellular compartments called glucosomes. With the use of Fluorescence Resonance Energy Transfer (FRET), interactions between PFKL and PKM2 were observed, supporting a functional purpose of enzyme organization inside glucosomes (manuscript in preparation). The use of fluorescence microscopy for live-cell imaging continues to advance to the use and evaluation of 3-dimensional datasets. The use of lattice light sheet microscopy is well suited to visualizing glucosomes because of the thin sheets of illumination formed by an array of non-diffracting Bessel beams. The positioning of the orthogonally placed objective lenses means that the illumination of a sample is confined to the plane of detection which reduces background illumination making it easier to distinguish glucosomes as 3-dimensional objects in the cytoplasm of the cell. Both colocalized datasets of other enzymes within the glucose metabolism and non-colocalized datasets of enzymes outside of the glucose metabolism were correctly identified from LLSM datasets. These datasets are more complete representations of the 3-dimensional living cell, which contribute an overall better understanding of spatial compartmentalization. By showing that these compartments spatially organize into a multienzyme complex, and that the glucosome is spatially distinct from other cellular bodies, the glucosomes are formed in a pathway-specific manner.

Chapter 3: Glucosomes form through liquid-liquid phase separation

3.1 Introduction

It has been demonstrated that the glucosomes form in the cytoplasm and are specific to the glucose metabolism (Kohnhorst et al., 2017). However, the mechanism of assembly is still not well known. Because the glucosomes were observed to reversibly form and exchange contents with the surrounding cytosol, it was determined that they were membraneless assemblies. Because the glucosomes were selective to the glucose metabolism and because enzymes in the glucosomes were observed to interact through FRET, it can also be inferred that there is an internal functional structure to glucosomes. Throughout the cell, other membraneless compartments have been observed (Uversky 2017; Alberti 2017). Membraneless compartments are identified as a spatially segregated compartment with a differing phase from the surrounding environment, but still able to content mix with the surrounding environment (Hyman et al., 2014). Glucosomes meet this criterion since they were observed to reversibly assemble, fuse and separate, and content mix with the cytoplasm as observed through Fluorescence Recovery After Photobleaching (FRAP) (Kohnhorst et al., 2017). By inducing a phase change within the cell, the formation of glucosomes was observed when cells were under higher osmotic pressure, providing evidence that glucosomes form via the phenomenon of liquid-liquid phase separation.

Phase separation occurs in heterogenous solutions like that of the cytoplasm. Macromolecules in solution may find it energetically favorable to condense into regions that distinctly separate macromolecule/macromolecule interactions which are

driven by thermodynamic properties like the temperature, pressure, and concentration of the macromolecules (Banani et al., 2017; Harmon et al., 2017; Martin and Mittag, 2018; Ruff et al., 2018). As shown in Fig. 5, there is a critical point where phase separation begins to occur for glucosomes in the cytoplasm of live cells at a constant temperature of 24°C. The demixing regime is the region inside of the cytoplasm where conditions are right for glucosomes to form. There is a minimal concentration to form glucosomes denoted by C_{in} and a maximal concentration where the environmental concentration of enzymes is too high to maintain a distinct liquid-like structure, denoted by C_{out}. The mixing regime is the region outside of this concentration range where the enzymes of glucosomes are unable to form into distinct liquid-like compartments. When osmotic pressure is increased at a steady temperature, the quantity of glucosomes increases as shown by the shift in the tie line to include more of the demixing regime. However, the characteristic concentration of enzymes within glucosomes remained largely similar, as indicated by the minimal distance between C_{out1} and C_{out2}. The concentration inside glucosomes was not observed to change under higher osmotic pressure, yet the fraction of total enzyme in the cell compartmentalized into glucosomes increased, denoted by the horizontal distance between C_{in1} and C_{in2}. The observed cellular response to osmotic pressure is to create more glucosomes through phase separation rather than increasing the concentration of enzymes inside existing glucosomes.

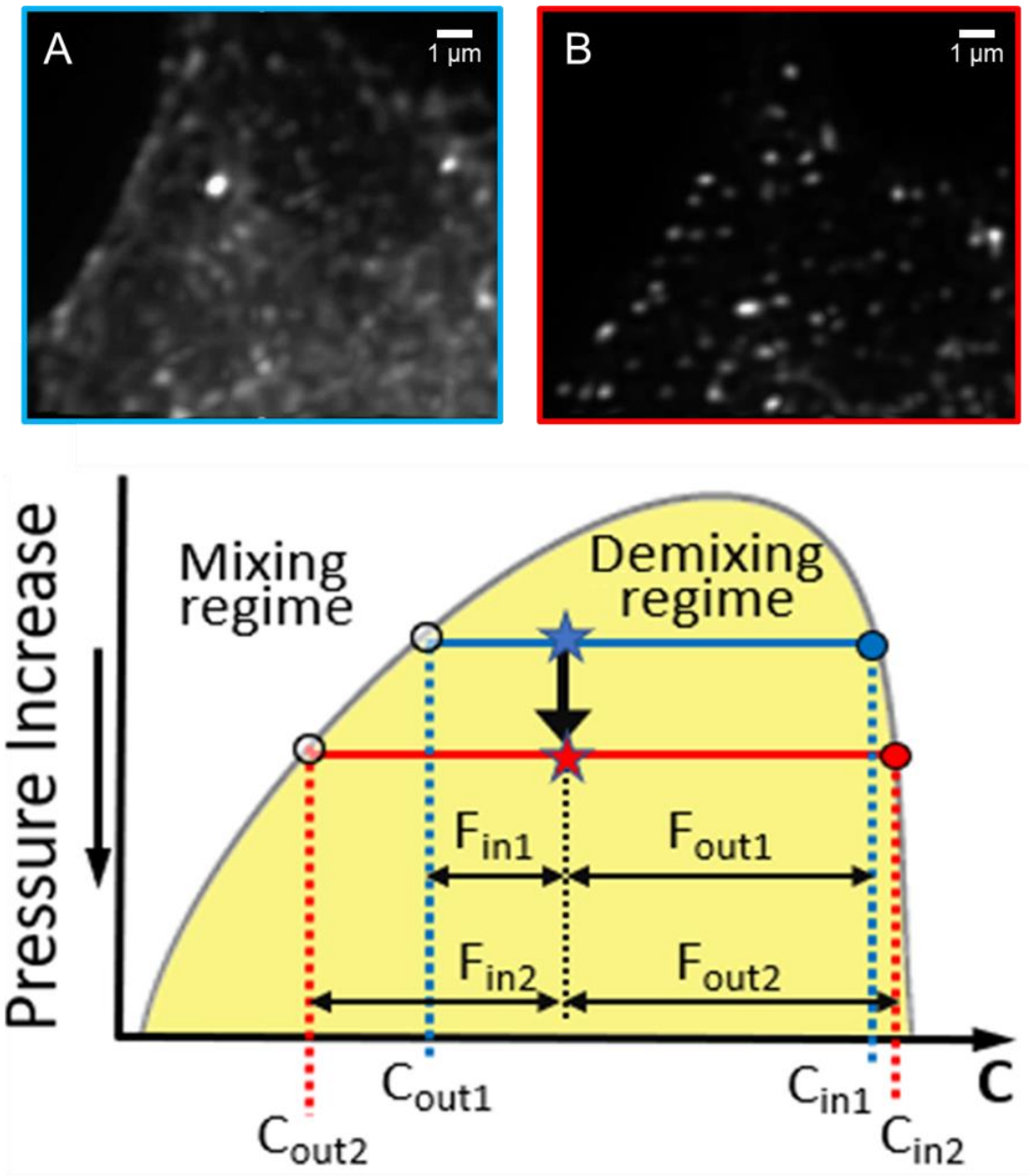

Figure 5: A cell containing glucosomes in normal BSS media (A) had osmotic pressure increased using PEG resulting in an increased quantity of glucosomes (B). The phase diagram of glucosomes shows the demixing regime in yellow where cytoplasmic conditions facilitate glucosome formation. With increased pressure, the necessary concentration to form glucosomes becomes lowered shown by the horizontal distance from C_{out1} to C_{out2}. The internal concentration of PFKL in glucosomes was not appreciably increased under osmotic pressure as shown by the similar position of C_{in1} versus C_{in2}. However, the total portion of cytosolic PFKL partitioned into glucosomes was increased so the tie-line between glucosomes inside and outside of compartments is parallel shifted to denote the increase in the quantity of assembled glucosomes without increase to the internal concentration within individual glucosomes.

3.2 Materials and Methods

3.2.1 Increasing osmotic pressure in live cells

High osmotic pressure was created by using a high-salt 1x BSS media altered to 200 mM NaCl, 20 mM HEPES, pH 7.4, 5 mM KCl, 1 mM $MgCl_2$, 1.8 mM $CaCl_2$, and 5.6 mM glucose. To apply the same osmotic pressure without increasing the concentration of NaCl, 4.4 % w/v polyethylene glycol was added to standard 1x BSS media containing 135 mM NaCl, 20 mM HEPES, pH 7.4, 5 mM KCl, 1 mM $MgCl_2$, 1.8 mM $CaCl_2$, and 5.6 mM glucose (PEG-300, Sigma; 91462).

3.2.2 Glucosomes size analysis with 3-dimensional datasets

The image datasets obtained after deconvolution and deskew processes from lattice light sheet imaging were evaluated using ImageJ software (NIH). The objects were detected using the 3D Objects Counter plugin and manually selecting thresholds that appropriately identified the glucosomes without falsely changing their volume. During training this was evaluated using line-scans and the full width at half maximum intensity. The volume, integrated intensity, and other physical factors were taken from the output of 3D Objects Counter and used to evaluate the size and density of the fluorescent species labeled. The region of interest (ROI) selection tool was used to identify all edges of the cell and nucleus to determine total fluorescence intensity inside of the cytoplasm in order to find the partition ratio between the fluorescently labeled enzyme inside of the glucosomes compared to the total amount of fluorescent enzyme expressed in the cell.

3.2.3 Fluorescence live cell widefield imaging

For widefield and confocal imaging: on the day of imaging (~18–24 h post-transfection), the cells were washed with buffered-saline solution (20 mM HEPES, pH 7.4, 135 mM NaCl, 5 mM KCl, 1 mM MgCl2, 1.8 mM CaCl2, and 5.6 mM glucose) for three 10 min incubations, followed by a ~1–2-h incubation at ambient temperature. All samples were then imaged at ambient temperature (~25 °C) with a 60X 1.45 NA objective (Nikon CFI 32 Plan Apo TIRF) using a Photometrics CoolSnap EZ monochrome CCD camera on a Nikon Eclipse Ti inverted C2 confocal microscope. Wide-field imaging was carried out using the following filter sets from Chroma Technology: mEGFP detection by a set of Z488/10-HC clean-up, HC TIRF dichroic, and 525/50-HC emission filter.

3.3 Results

3.3.1 Widefield population studies showed an increase to osmotic pressure

In order to ascertain that that the liquid droplet like behavior of the glucosomes was caused by phase separation, a readily controllable physical phase factor was manipulated. Hs578T cells expressing PFKL-mEGFP were first imaged for 10-30 minutes at ambient temperature to ascertain the behavior of the individual cells. Then the media was exchanged with 200 mM NaCl high-salt media or a 4.4 % w/v PEG media that would each increase the same amount of osmotic pressure and the cells were observed for an additional 30-60 minutes. Afterwards, the media was rinsed with fresh, standard 1x BSS media and imaged for an additional 30-60minutes. The number of glucosomes in single cells were quantified as ‘stable’, ‘decreasing’, or ‘increasing’ based on the quantity of glucosomes and total volume of glucosomes prior to, during, and after the experimental condition (Fig. 6). Experiments were repeated at least three

times and compared to control studies, which used media exchanges of standard 1x BSS media throughout the same time-course experiment. During treatment with high-salt, 78.8 $\pm$ 7.3 % of cells showed elevated glucosomes during high-salt conditions and decreased glucosomes after removal of high-salt conditions (N = 91) (Fig. 6a). Elevated levels of NaCl can cause stress responses in bacterial cells that increase glucose utilization by increasing the glycolytic activity of phosphofructokinase and other enzymes (Li et al., 2015). To test whether the higher concentration of NaCl influenced the glucose metabolism in the Hs578T cancer cells beyond the physical phase separation, the use of cell-impermeable polyethylene glycol (PEG) was used to show that the increase in glucosomes was primarily from the increase of osmotic pressure. When increasing the osmotic pressure on cells using PEG media, the population of cells showed an increase in glucosomes under higher osmotic pressure in 72.4 $\pm$ 4.7 % of cells (N = 83), and after the removal of osmotic pressure by rinsing with 1X BSS media, glucosomes were likewise reduced in 66.4 $\pm$ 5.3 % of cells (N = 78) (Fig. 6b). These populations were not found to be significantly different as denoted by the overlap in the standard error bars (Fig. 6c,d). Altogether this suggests that the formation of glucosomes is greatly influenced by osmotic pressure, showing that their mechanism of formation is influenced by a physical phase change which is one of the behaviors of liquid phase separated droplets.

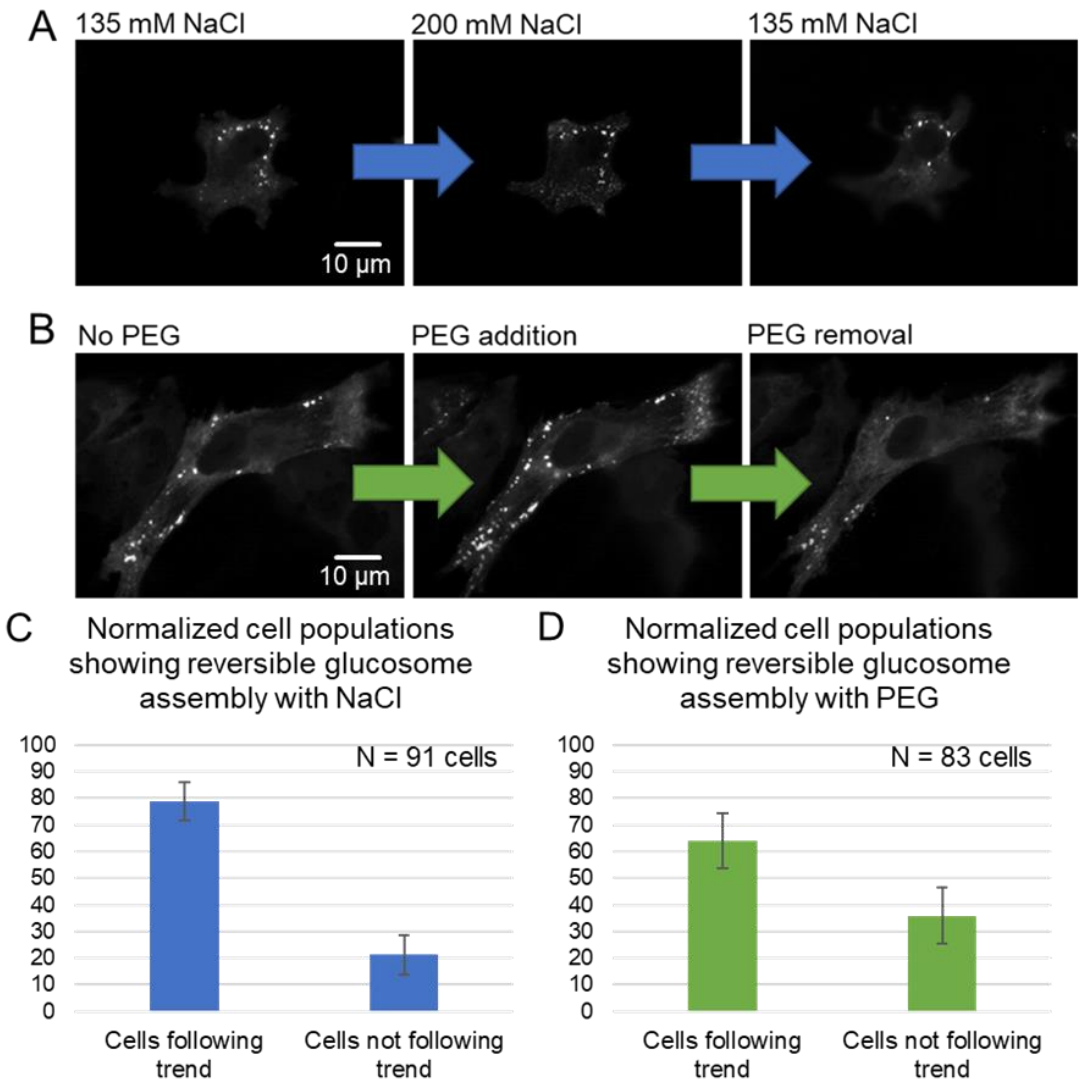

Figure 6: Phase-separation drives the formation of glucosomes. Using widefield fluorescence microscopy, the trends of glucosomes were observed under increased osmotic pressure. Using a high-salt formulation of 200 mM NaCl-BSS media (A) or 4.4 % w/v PEG-BSS media (B) cells were treated for 30-60minutes and quantified as stable if they retained the same amount of glucosomes or as increasing or decreasing if the amount of glucosomes changed during that time. The majority of cells responded to both conditions of high pressure by reversibly forming glucosomes during treatment with 200 mM NaCl-BSS (C) or 4.4 % w/v PEG-BSS (D) demonstrating glucosomes formation could be induced via phase separation.

3.3.2 Lattice light sheet quantification of PFKL inside glucosomes

In addition to the widefield studies, 3-dimensional imaging was performed to study the concentration of PFKL inside glucosomes before and during high osmotic pressure. During the 1-2 hour course of the experiments, no change in the expression of PFKL-mEGFP was observed in cells as shown by the vertical transition of the blue star to red star (Fig. 5). During the experiment, the cellular volume where glucosomes could form was reduced in size by approximately 11 % of the original volume (Fig. 7a). The cumulative volume of glucosomes within that same cellular space more than doubled (Fig. 7b). The presence of PFKL specifically inside glucosomes increased from 100% to 112.3 $\pm$ 18.7 % (N = 1834 glucosomes, std) when using PEG-BSS media conditions (Fig. 7c). The change in glucosome volume fraction (F) was calculated based on the change from $F_{in1}/(F_{in1}+F_{out1})$ to $F_{in2}/(F_{in2}+F_{out2})$, where F_{in} represents the volume fraction of the enzyme of interest inside of glucosomes and F_{out} represents the volume fraction of the enzyme of interest in the cytosol (Fig. 5). The characteristic concentration of PFKL inside glucosomes was similar under higher osmotic pressure, which is why the slope between C_{in1} to C_{in2} was steep (Fig. 5). However, a larger fraction of all PFKL was observed compartmentalized into glucosomes during higher osmotic pressure which led to a larger F_{in2} (Fig. 5). Osmotic pressure increased the volume fraction of cellular PFKL compartmentalized into glucosomes but did not affect the concentration of PFKL within glucosomes. This indicates that the cell responds to increased osmotic pressure by creating more glucosomes through phase separation.

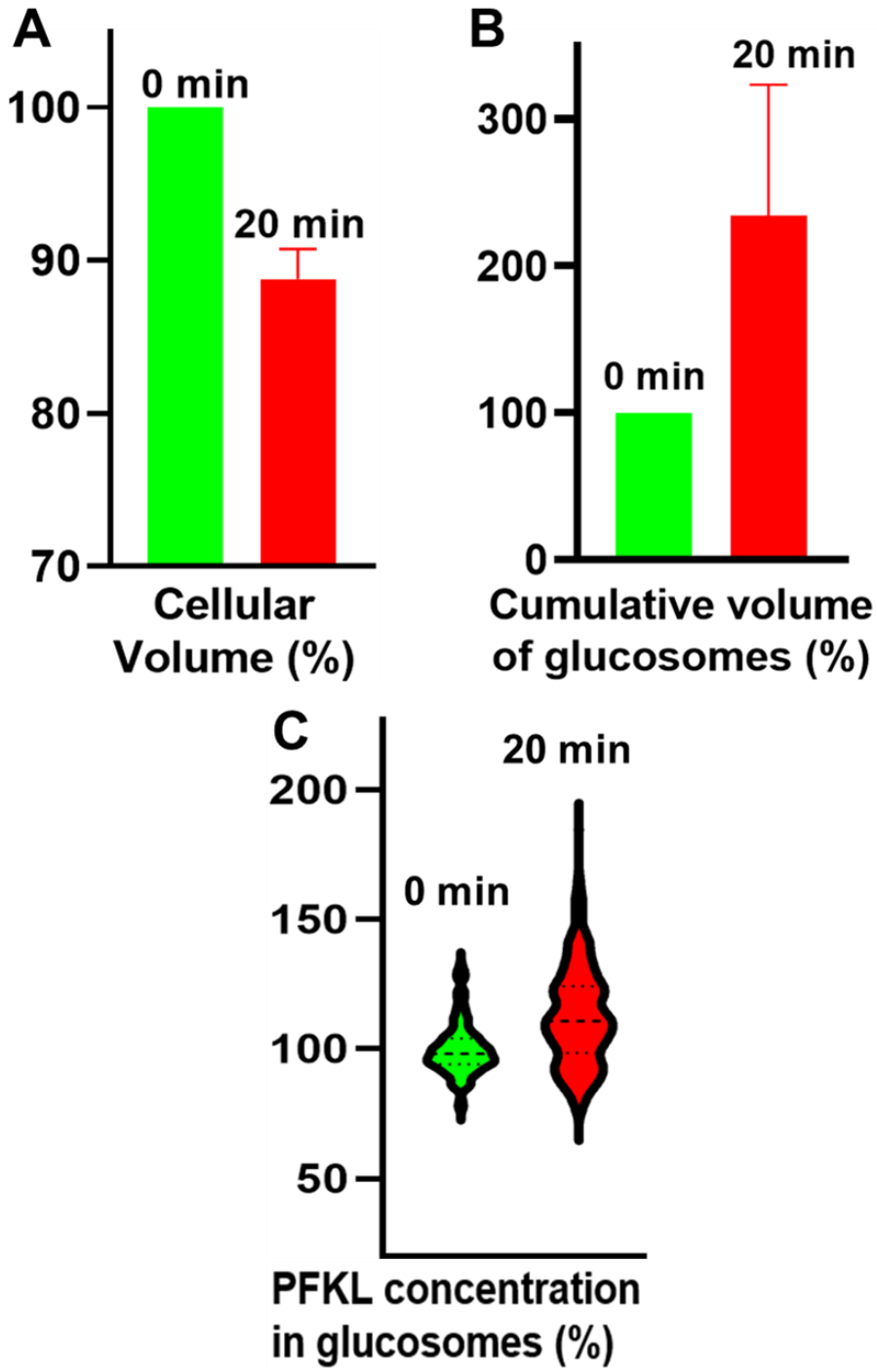

Figure 7: Increased osmotic pressure led to increased partitioning of PFKL into glucosomes. After addition of polyethylene glycol (PEG) which increased osmotic pressure, the cellular volume (A) where glucosomes could form was decreased by approximately 11 %. However, the cumulative volume of glucosomes in that same space more than doubled (B). The concentration of PFKL inside of glucosomes prior to and after increased osmotic pressure remained similar (C) which shows that the cellular response to increased osmotic pressure is to partition enzymes into new glucosomes rather than increasing the concentration inside existing glucosomes.

3.3.3 Fusion of glucosomes does not increase the concentration of PFKL within glucosomes

By observing glucosomes before and after fusion events it was apparent that the characteristic concentration of glucosomes remained consistent with the increased volume of the merged glucosome. The characteristic concentration was calculated using the integrated fluorescence intensity per volume of glucosomes. By tracking glucosomes that merged, the characteristic concentration prior to merge compared to the characteristic concentration after the merging event showed a ratio of 0.94 ± 0.13, indicating that the integrated intensity of the glucosome increased proportionally with the volume. This characteristic volume was observed to be constant for glucosomes of size bins ranging from 228.3 ± 20.3 voxels to 969 ± 46.4 voxels (Fig. 8). This result indicates that the larger sizes of glucosomes behave with consistent molecular characteristics, suggesting that they retain functional properties as they merge. Altogether, these experiments demonstrate several behaviors of liquid-liquid phase separated biocondensates in live cells.

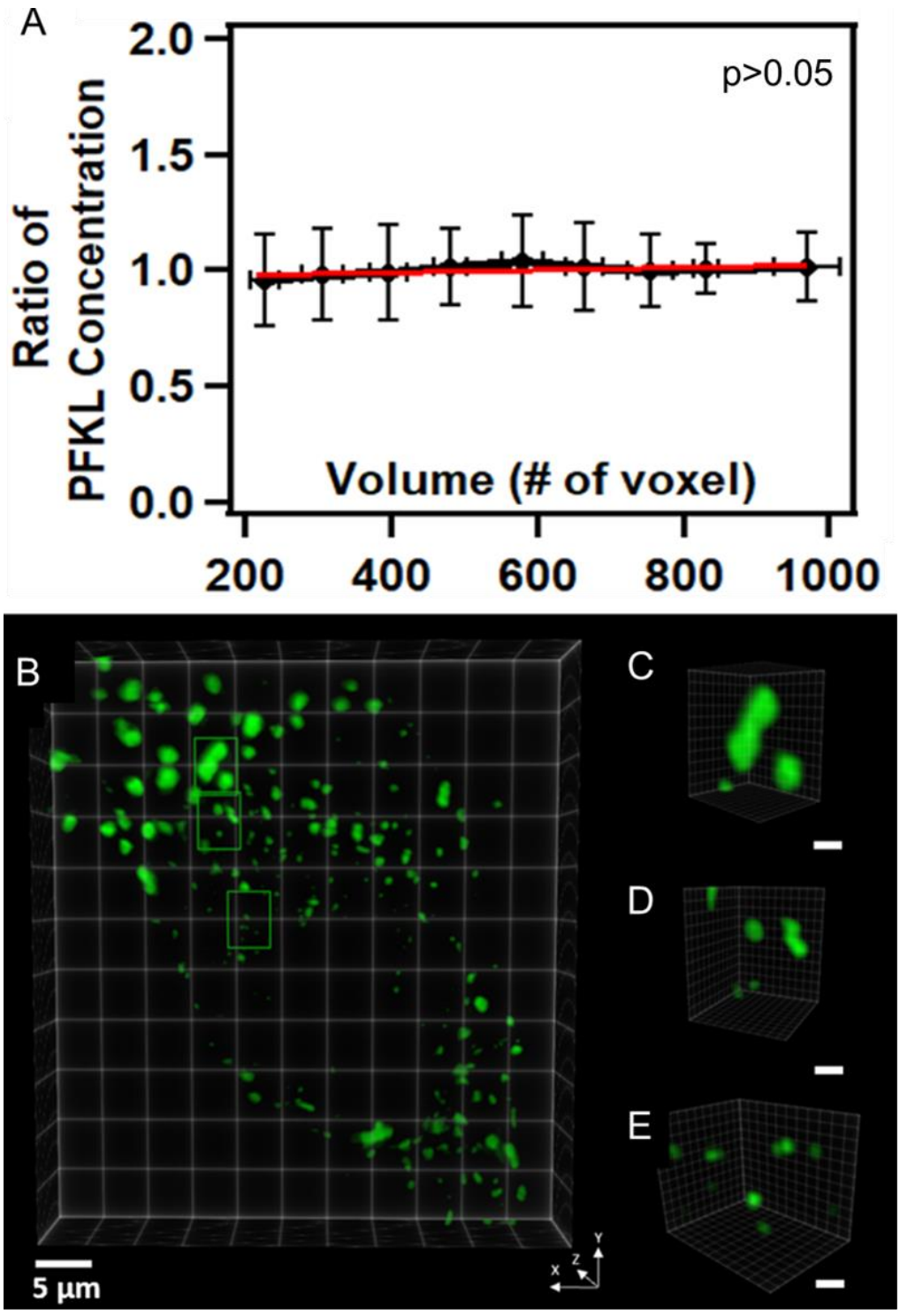

Figure 8: The characteristic concentration of PFKL analyzed with respect to glucosome volume. The characteristic concentration of PFKL was found to be independent of the size of glucosomes for the size bins of 228.3 ± 20.3 voxels to 969 ± 46.4 voxels.

3.4 Discussion

This work demonstrates that the formation of glucosomes is controlled through liquid-liquid phase separation. By increasing the osmotic pressure, the critical concentration needed for cytosolic PFKL to begin to form glucosomes was lowered leading to an increase in glucosome formation (Fig. 5). While the total volume of glucosomes increased over the cell, the concentration of PFKL within the glucosomes remained steady which suggests that after glucosomes initially form, the characteristic concentration of PFKL inside glucosomes remains consistent. This points to live cells maintaining the molecular characteristics of glucosomes after initial formation into membraneless compartments by increased partitions of enzymes into glucosomes rather than increasing the characteristic concentration of enzymes inside of glucosomes in response to hyperosmotic stress. This can be interpreted to mean that the internal characteristics of glucosomes are necessary to their function even during events of cellular stress.

Chapter 4: High partition coefficient supports that the glucosomes have an internal structure utilizing oligomeric phophofructokinase-1

4.1 Introduction

The propensity to phase separate has been linked with multivalency, including for glycolytic enzymes observed in yeast, *C. elegans*, and mammalian tissues (Jin et al., 2017; Jang et al., 2021; Li et al., 2012). A previous study showed active phosphofructokinase-1 formed filaments *in vitro* while inactive PFKL did not (Webb et al., 2017). By using fluorescence resonance energy transfer (FRET) in a cell with PFKL-mEGFP and PFKL-mOFP dually transfected, it was observed that PFKL formed higher-ordered structures inside of live cells as well (Kohnhorst et al., 2017; unpublished). Additionally, FRET has identified interactions between PFKL and other enzymes in glucosomes, but it is not well understood how enzymes in the glucose metabolism partition into glucosomes. Herein lattice light sheet microscopy is used to compare the partition ratio of enzymes in glucosomes and shows that PFKL is a more highly partitioned enzyme in glucosomes due to its higher multivalent oligomer state.

4.2 Methods and Materials

4.2.1 Partition Ratio Analysis

The Image J 3D Objects Counter was used as previously described. In some cases, multiple intensity thresholds and size categories were applied to a cell in order to accurately identify all glucosomes of various sizes. The output binary objects maps were combined into one 8-bit objects map file. Additionally, the Allen Center Cell & Structure Segmenter was sometimes used to identify assemblies in the PFKL image

dataset volumes. In either case, the output binary object maps were applied to the 16-bit data files of both PFKL and PKM2 image datasets using the ImageJ 3D Objects Counter tool. This preserved raw intensity values from the original data while providing sensitive glucosome selection. The volume and integrated density of glucosomes versus the total volume and fluorescence intensity of the entire cytoplasm were used to calculate the partition coefficient of each enzymes image dataset. These partition values were also categorized in a size-binned manner.

4.3 Results

4.3.1 Phosphofructokinase-1 strongly partitions into liquid-liquid phase separated glucosomes in live cells

The partition coefficient is a measure of the total enzyme inside of a glucosome compared to the enzyme in the surrounding cytoplasm. Using lattice light sheet microscopy and a segmentation tool, glucosomes were selected as regions of interest. The regions of interest were applied to both the PFKL and PKM2 image datasets to determine the total intensity, size, and density of either enzyme in the glucosomes. Additionally, the entire cell was analyzed for total intensity, size, and density of either enzyme for the entire cytoplasm. Then the partition coefficients (P.C.) were analyzed to show the ratio of enzyme density inside the assembly versus the density of enzyme in the cytoplasm (Fig. 9). It was observed that PFKL partitioned into glucosomes with a $P.C._{PFKL} = 22.02 \pm 2.29$ (N = 39), and PKM2 partitioned into glucosomes with a $P.C._{PKM2} = 2.24 \pm 0.08$ (N = 40). The partition coefficient is 9.8 times higher for PFKL which is consistent with reports that higher multivalent oligomeric states result in higher partition efficiency (Banani et al., 2016). Given that PFKL is known to

oligomerize *in vitro*, the higher partition coefficient ratio of PFKL could suggest organization of that enzyme into higher ordered filamentous structures in live cells (Webb et al., 2017).

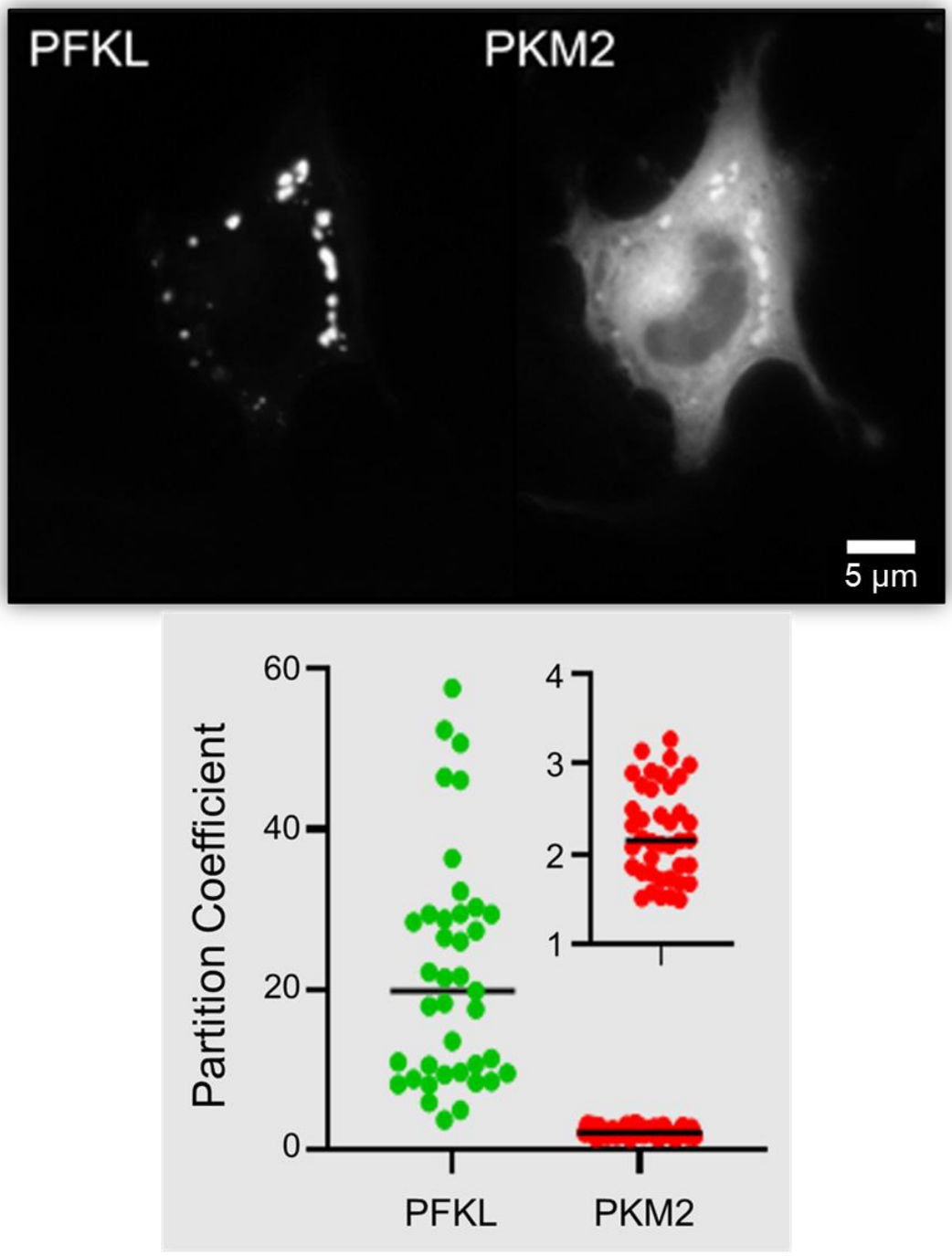

Figure 9: The partition coefficient of PFKL compared to PKM2. The amount of enzyme partitioned into glucosomes was calculated for cells expressing both PFKL and PKM2 as the ratio of the enzyme inside of the glucosomes compared to the enzyme in the cytoplasm. PFKL is partitioned into glucosomes ~10 x more than PKM2

4.3.2 Small size glucosomes were found to have reduced PFKL partition ratios

Small size glucosomes are difficult to visualize against cytoplasm using techniques like widefield microscopy that takes a projected image. This is because the projected image will include a larger z-dimension that has been compounded into a 2-dimensional image which can diminish the appearance of small glucosomes against the freely diffusing enzymes in the cytoplasm. Therefore, 3D imaging techniques like lattice light sheet microscopy are well suited for studying smaller sized glucosomes. It was determined through control experiments using 100 nm fluorescent beads that 89 voxels was a physical cutoff to include all small sized glucosomes. By subcategorizing the partition coefficients of PFKL and PKM2, it was observed that the smallest category of glucosomes showed a significant reduction in the PFKL:PKM2 ratio ($p>0.05$). The partition coefficient of PKM2 remained relatively constant no matter the size of the glucosome, but the PFKL ratio was about 25% lower only in glucosomes smaller than 89 voxels. This result showed that glucosomes under this size had a distinctly different compositional ratio of PFKL and PKM2 (Fig. 10). The size of glucosomes can be used to predict the direction of glucose flux (Jeon et al., 2018). A higher compositional ratio of PKM2 would suggest that small glucosomes preferentially promote glycolysis. Given the higher sensitivity of LLSM 3-dimensional imaging for small glucosome quantification, this defined behavior adds to previously published research showing the larger sizes of glucosomes preferentially direct glucose flux into building block biosynthesis (Jeon et al., 2018).

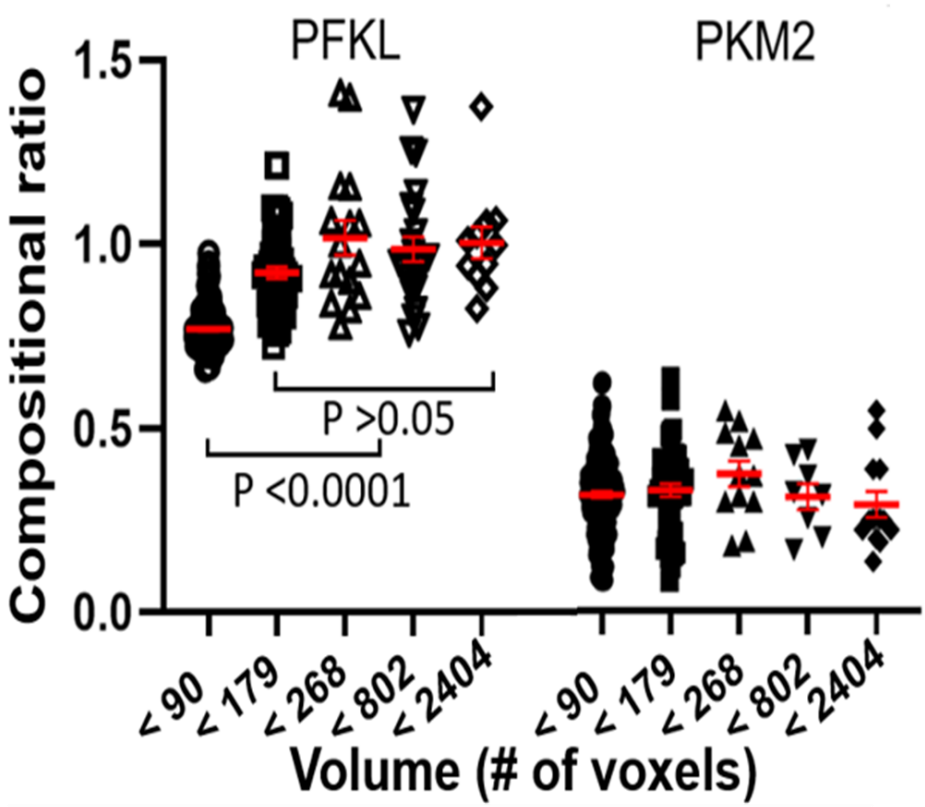

Figure 10: The size-dependent partition coefficient of PFKL compared to PKM2. While PKM2 retained the same partition coefficient regardless of the volume of the glucosome, PFKL has lower partition coefficients at lower volumes.

4.4 Discussion

Based on these findings, the reports that PFKL forms filamentous structures inside of glucosomes in live cells is heavily supported by the consistently high partition rate of PFKL compared to other enzymes in the glucosome (Webb *et al*., 2017). Additional unpublished FRET studies through a collaboration have also brought support that filamentous PFKL may act as a scaffold inside glucosomes in live cells. Lastly, detection of the increased ratio of PKM2 to PFKL inside small glucosomes demonstrates robust quantification of glucosomes of all sizes. The proximity of multiple enzymes in specific ratios seem point to a process similar to metabolic channeling, where the compartmentalization of specific enzymes direct metabolic flux through a series of biochemical reactions. The glucose metabolism has multiple alternative pathways where the metabolic intermediates can be shunted at certain steps in glycolysis. A higher ratio of PKM2 to PFKL can indicate that small glucosomes have an increased affinity to the pathway of glycolysis due to the higher ratio of PKM2, which catalyzes the last step in glycolysis. This demonstrates that the distinct enzyme stoichiometry in glucosomes may impact their function with respect to metabolic flux inside of living cells.

Chapter 5: Glucosomes have a spatial and functional relationship with the mitochondria

5.1 Introduction

The glucose and mitochondria metabolisms are intertwined especially in respect to disease (Liemburg-Apers et al, 2015; Fogg et al., 2011; Sivitz and Yorek, 2010). Cancer cells suffer from dysregulated metabolism resulting in uncontrolled proliferation and resistance to apoptosis (Hanahan and Weinberg, 2011; Mohammad et al., 2015). The cancer cell metabolism upregulates the production of adenosine triphosphate, a major supply of energy throughout the cell, using the glycolysis pathway even under aerobic conditions (Simonnet et al., 2002). This phenomenon of upregulated glycolysis is known as the Warburg effect (Warburg et al., 1927; Locasale et al., 2011). The production of ATP is redirected to occur in the subcellular region of the cytoplasm more predominantly than the mitochondria which is a specific subcellular compartment efficient at producing ATP under anaerobic conditions (Zheng, 2012). While original publications reported that mitochondria were not essential to cancer cell metabolism due to the increased production of ATP through glycolysis, this has recently been shown to be incorrect as the mitochondria function differently in cancer cells but are not inactivated (Cassim et al., 2020). More recently reported, the mitochondria can provide escape pathways to cancer therapeutics targeting glycolysis, so understanding the relationship between the glucose metabolism and mitochondria is critical for overcoming limitations in cancer therapies (Lopez and Tait, 2015; Shiratori et al., 2019).

Enzymes in the glucose metabolism are overexpressed in cancers. Hexokinase isoform 2 (HK2) is one of those overexpressed enzymes and contributes to the Warburg effect, which is the common dysregulation of the glucose metabolism found in cancer cells (Hu et al., 2014; Wilson, 2003; Zhang et al., 2016). HK2 is the first enzyme in glycolysis and can be located on the surface of mitochondria (Mathupala et al., 2009). Phosphofructokinase 1 is a powerful regulator of glycolysis in all cells, but the liver type isoform (PFKL) is highly expressed in rapidly proliferating cells and acts as a switch for glycolysis (Zancan et al., 2010; Feng et al., 2020; Ausina et al., 2018; Mor et al., 2011). Pyruvate kinase is found in all types of human cells in various isoforms. The pyruvate kinase muscle type 2 isoform (PKM2) is overexpressed in rapidly proliferating cells and can form monomers, dimers, and tetramers as needed, with the tetrameric form of PKM2 being active in glycolysis (Jiang et al., 2014; W. Yang et al., 2012). Aldolase is found in three isoforms, A, B, and C, throughout all cells. It has been demonstrated that upregulation of aldolase B provides fuel for cells during cancer proliferation (Bu et al., 2018). Mitochondrial function was restored by inhibiting the pyruvate dehydrogenase kinase which reprograms the glucose metabolism and restores cell death by mitochondrial stress (Deng et al., 2020). Additionally, the detachment of hexokinase 1 and 2 from the surface of mitochondria also showed similar recovery of cell apoptosis (Goldin et al., 2008). Lastly, the product of glycolysis, pyruvate, is imported into the mitochondria to start the TCA cycle, and both metabolisms work to generate ATP (Shiratori et al., 2019).

The physical intersections between the glucosome and mitochondria can therefore provide additional insight into their metabolic network. A similar

characterization has been applied to another membraneless compartment, the purinosome, which was found to be spatially associated with the mitochondria using 3-dimensional super-resolution imaging (French et al., 2016). Lattice light sheet fluorescence imaging similarly captures 3D live-cell data and was used to observe the spatial behavior of the glucosomes in living cells compared to the mitochondria. Here it is presented that the glucosomes have a spatial link with the mitochondria which is stronger in regions of densely populated mitochondria and stronger for small sized glucosomes. Additionally, disrupting the glucose and mitochondria metabolism at several key points showed support that the functional relationship impacts the spatial relationship between mitochondria and glucosome (Fig. 11). The functional relationship between glycolysis and mitochondria were interrupted at the beginning of glycolysis by knockdown expression of hexokinase 2, at the transport of pyruvate into the mitochondria by inhibiting the pyruvate dehydrogenase complex, and lastly at the end of oxidative phosphorylation by inhibiting ATP synthase. By interrupting the functional relationship between the glucose and mitochondria metabolisms at these locations, it was observed that glucosomes changed their spatial relationship with the mitochondria in response, suggesting that glucosomes are functionally organized throughout the cell.

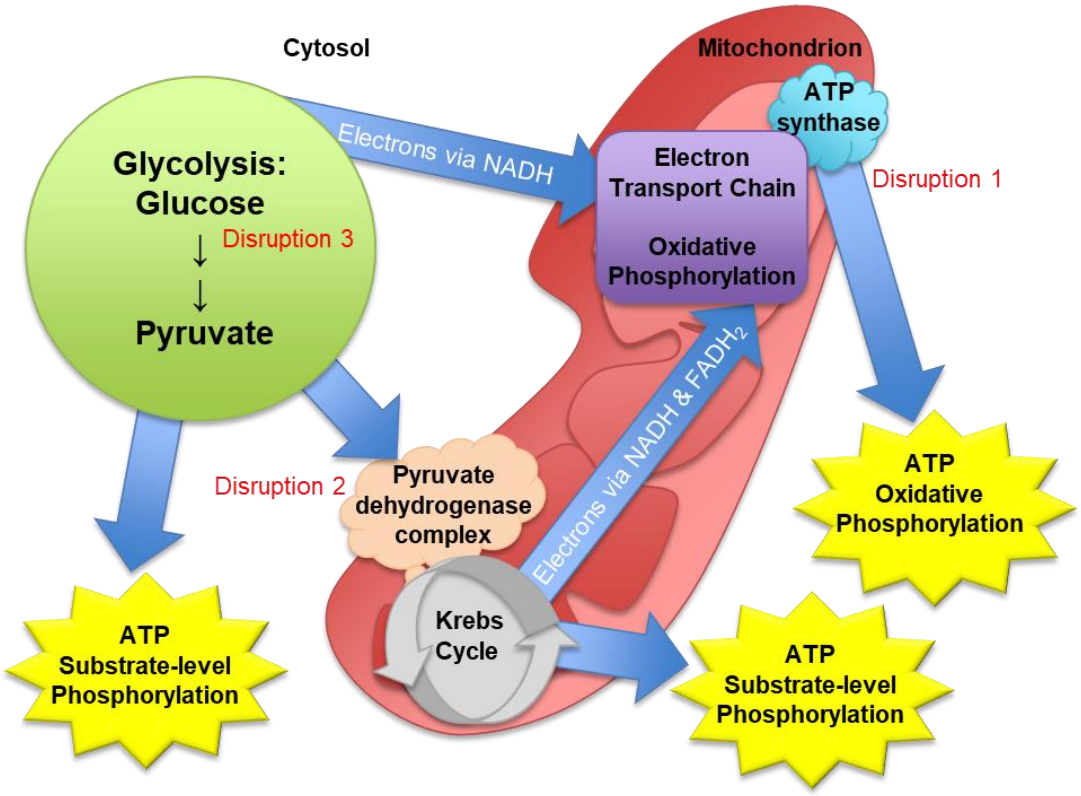

Figure 11: The connections between the glucose metabolism and mitochondria. Disruptions were added through use of small-molecule inhibitors or the knockdown of enzyme expression. Disruption 1 uses Oligomycin A to impair oxidative phosphorylation at the mitochondria. Disruption 2 inhibits the pyruvate dehydrogenase complex. Disruption 3 is a knockdown of hexokinase M2 expression.

5.2 Methods and Materials

5.2.1 Using MitoTracker™ to label cells

Following cell culture and transfection methods, addition of 50 nM MitoTracker™ Green or Red (Invitrogen) was performed prior to adding TetraSpeck™ fluospheres. Cells were incubated with the MitoTracker for 5-10minutes and then rinsed with 1x BSS. Tetraspeck beads were added as usual, and the cells were allowed to incubate at room temperature for 1-2 hours prior to imaging.

5.2.2 Treatment with small molecules to disrupt the mitochondria and glucose metabolisms

Various small molecules were dissolved in dimethyl sulfoxide (DMSO) solution and added to 1X BSS imaging media. The cell culture grade dimethyl sulfoxide (DMSO) was purchased from Sigma-Aldrich (Cat# 276855). Oligomycin A was purchased from Enzo Life Sciences (Cat# BML-CM111-0005) at a final working concentration of 10 µM. CPI 613 (6,8-Bis[(phenylmethyl)thio]octanoic acid is a PDC and KGDH inhibitor was purchased from Tocris Bioscience (Cat# 5348) at a final working concentration of 200 µM. Control experiments were conducted using an equal volume of the vehicle.

5.2.3 3D Spatial Analysis

TetraSpeck™ microspheres were used to align multiple color channels using an in-house Matlab code for sub-pixel corrections in 3D (An et al., 2019). Binary object maps of each color channel were generated using the ImageJ processing software (National Institutes of Health), particularly the ImageJ 3D Objects Counter plugin

(Bolte & Cordelières, 2006), or the Allen Cell Structure Segmenter (Chen et al., 2018). 3D distance analysis was performed on these binary segmented object maps using an in-house Matlab code that determined the minimal distance in 3-dimensions between surfaces in the red and green channels. The in-house code uses the segmented maps of 3D objects in one color channel to perform edge-to-edge measurements of objects in the other color channel. The output is a single 3D distance measurement to the nearest neighbor of each object in the primary color channel based on the voxel-edges of the objects (Fig. 12). To have statistical relevance, the data was collected from multiple locations within a single cell, and from multiple cells imaged from at least 3 replicated experiments.

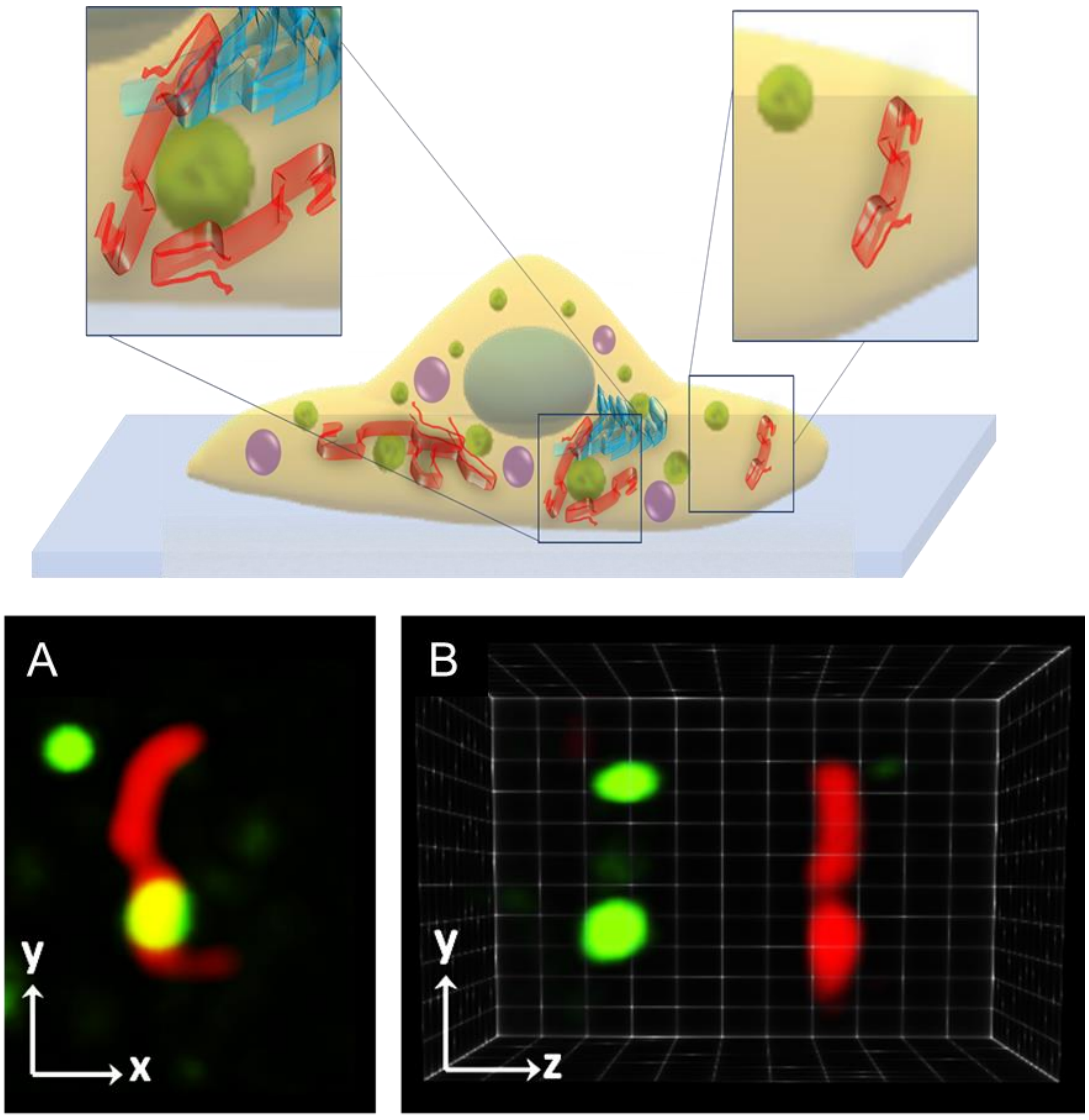

Figure 12: Spatial analysis shows the edge-to-edge distance between objects in 3-dimensional vector space as occurs in the diagram of a live cell. The output is a vector distance between the closest edges or faces the objects. While some colocalization is observed in 2-dimensions (A), the 3-dimensional view gives a more complete measure of spatial distances showing no colocalization (B) demonstrating the power of 3-dimensional imaging for spatial analysis.

5.2.4 Glucosome volume and density analysis

Glucosome data was processed using ImageJ processing software (National Institutes of Health), particularly the ImageJ 3D Objects Counter plugin (Bolte & Cordelières, 2006). The deconvolved TetraSpek beads were used to determine that glucosomes smaller than 89 voxels should be considered "small" as is matching with previously reported size categories (Kohnhorst et al., 2017). The physical characteristics of the assemblies obtained from the 3D object counter or other segmentation methods were used to analyze the density of assemblies. In order to compare between cells, the smallest assemblies (which are present in virtually all cells) were used as a standard or normalization which allowed for multi-cell comparisons regardless of fluorescent plasmid expression.

5.2.5 Knockdown of hexokinase isoform 2 in Hs578T cells

The knockdown cells were obtained from the An lab. Lentiviral pGFP-shHK2 vector encoding human sh-HK2 and non-silencing control pGFP-C-shLenti vector were purchased from OriGene Technologies Inc (Rockville, MD, USA). To knockdown HK2 protein, Hs578T cells ($1X10^6$) were cultured in 30 mm dishes containing previously described RdF cell culture medium without antibiotics overnight (Kohnhorst et al., 2017). Medium was changed with Opti-MEM medium before transfection with 1 µg plasmid DNA per 30 mm dish with pGFP-shHK2 (Cat# TL312415) and non-silencing control pGFP-C-shLenti plasmid (Cat# TR30023) by using Lipofectamine 2000 reagent (Invitrogen). After 5 hours of transfection, Opti-MEM medium was replaced with antibiotic free regular medium (RdF) and incubated overnight. After 24 hours of transfection, RdF media supplemented with $1\ \mu g\ ml^{-1}$

puromycin (Sigma, Cat# P8833) was used for a selection period of 48 hours. After 48 hours of puromycin selection, cells were washed with cold PBS and 130µl of RIPA buffer along with protease (Pierce, Cat# 88666) and phosphatase inhibitors (Pierce, Cat# 88667) were added directly into the dishes. Samples were collected into the microcentrifuge tubes and efficacy of sh-HK2 protein inhibition was verified by western blotting.

5.3 Glucosomes were found to be spatially associated with the mitochondria

This distance of spatial association was defined to be 275 nm since it is the averaged measure of spatial resolution across all three dimensions for both color channels. Each glucosome was isolated using Image J or Allen Cell Segmenter tools to create 3D object maps. The use of an edge-to-edge distance program written in Matlab resulted in the distance to the surface of the nearest mitochondria for every detected glucosome. These distances were then plotted as a histogram showing the population of glucosomes per cell versus the distance to the nearest mitochondria. Glucosomes in a whole cell showed a spatial association in 37.8 $\pm$ 7.9 % of glucosomes to be within 275 nm of the glucosome (N = 7 cells, 2147 glucosomes) (Fig. 13). Because the distribution of the histogram fit within a double-exponential function, this indicated that two populations were represented in the histogram (Fig. 13). One population represents the glucosomes that are spatially associated with the mitochondria, which is a non-random spatial association within 275 nm with a mean distance of 65.4 $\pm$ 25.8 nm. The other population is spread further away from the mitochondria, at distances greater than 275 nm with a mean distance of 988.7 $\pm$ 41.9 nm. Collectively, these two spatially distinct populations demonstrate that one population of glucosomes is strongly

spatially associated with the mitochondria while the other population is dispersed stochastically further from the mitochondria. By categorizing subcellular regions of the cell based on the presence of mitochondria, these two trends become more apparent. Mitochondria-rich regions of the cell were defined as areas occupied by approximately 8.7 $\pm$ 1.3 % mitochondria, by volume (Fig 12). Mitochondria-sparse regions were similarly defined with 1.8 $\pm$ 0.5 % mitochondria by volume (Fig. 14). Subcellular regions with higher presence of mitochondria are populated by glucosomes that are strongly spatially associated with the mitochondria, while subcellular regions of sparse mitochondria demonstrate the stochastic spatial relationship between glucosomes and mitochondria (Fig. 13). The number of glucosomes distributed in mito-dense and mito-sparse regions were statistically the same, but 61.2 $\pm$ 5.3 SEM % of glucosomes in the mito-dense regions were associated with the mitochondria while 13.8 $\pm$ 3.4 SEM % of glucosomes in the mito-sparse regions were associated. This demonstrates that the glucosome metabolic compartments have a distinct spatial relationship to the mitochondria.

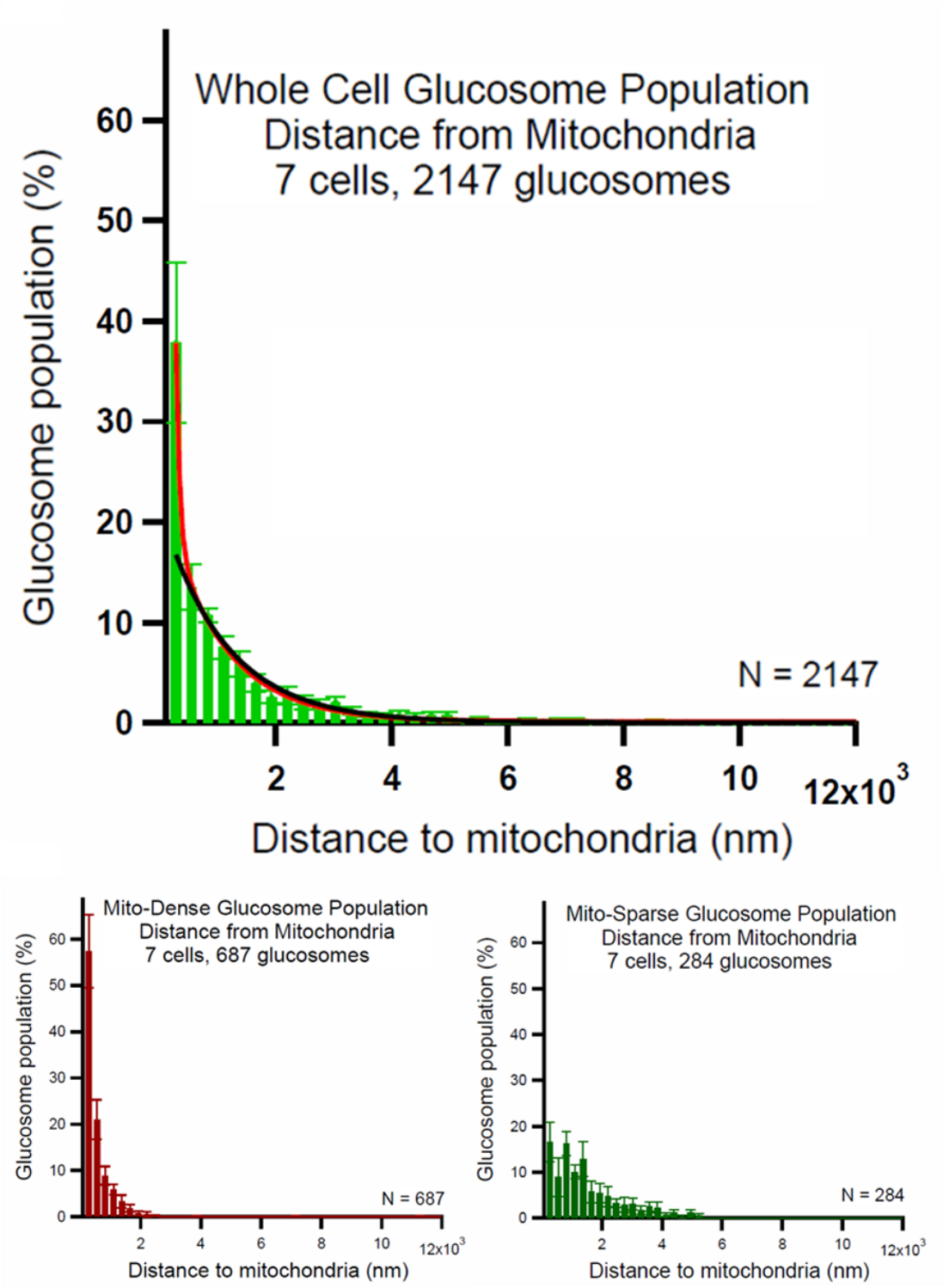

Figure 13: Histogram of all glucosomes shown as a population per cell, distributed as a measure of distance from the mitochondria surface. Data represents 2147 glucosomes with standard error bars. Data fit with double exponential decay (red line) or single exponential decay (black line).

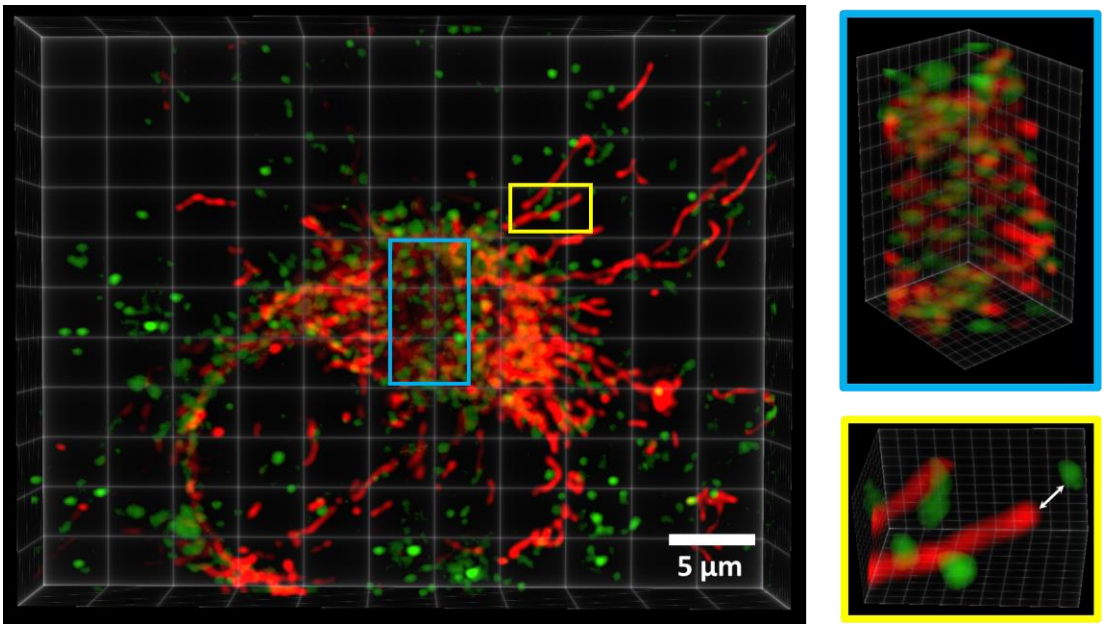

Figure 14: Subcellular regions of interest were defined as mitochondria-rich (blue) or mitochondria-sparse (yellow) based on the volume of the region occupied by mitochondria.

5.3.1 Subcellular regions of interest had distinct glucosome behaviors

Given that previous findings showed small-sized glucosomes might preferentially direct glucose flux through glycolysis, glucosomes were further sorted based on their sizes, with 89 voxels being used to sort glucosomes into a small category consistent with previously published small-sized glucosomes (Kohnhorst et al., 2017). It was observed that small-sized glucosomes demonstrated the same trend of spatial distribution throughout the cell (Fig. 15). Additionally, of all mito-dense glucosomes that were associated with the mitochondria, 66.5 $\pm$ 12.1 SEM % of them were defined as small-sized glucosomes (Fig. 15). These results indicate that a significant population of glucosomes in the cell are spatially close to the mitochondria and have a stronger association within the subcellular regions of dense mitochondria. Given the previous findings that small glucosomes showed an affinity for glycolysis, the findings that small glucosomes were more readily associated with the mitochondria is consistent with the concept of metabolic channeling between glycolysis and the mitochondria metabolism. Additionally, in the crowded cytoplasm of the cell, regions with dense mitochondria were found to have a prevalence of small glucosomes which were strongly associated with the surface of mitochondria. This shows that the regulation of metabolic processes in the cell is done with respect to subcellular environment, pointing to a spatial and functional regulation between the glucose metabolism and mitochondria.

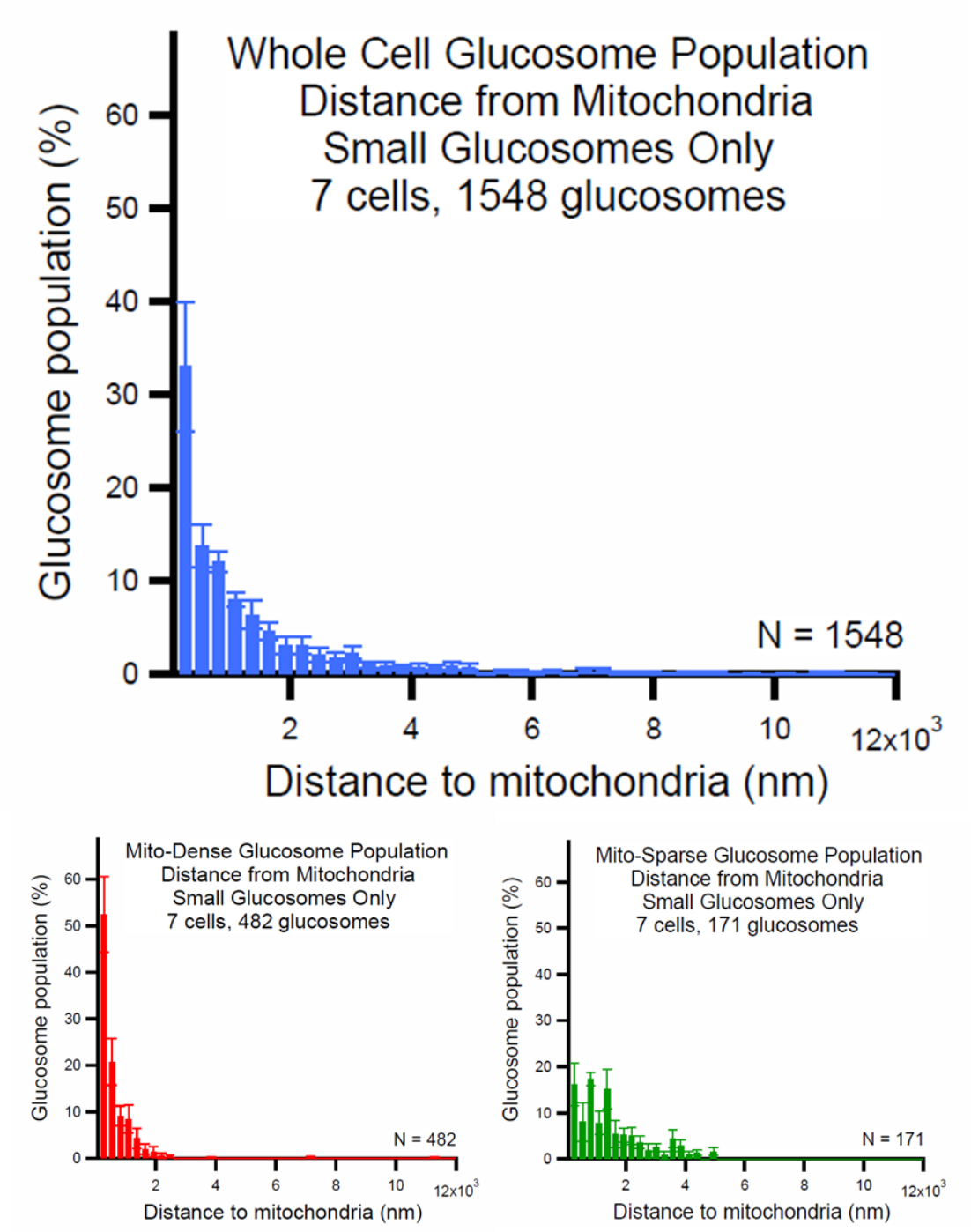

Figure 15: Small-sized glucosomes are more readily associated with the surface of mitochondria as defined by a distance less than 275 nm. In regions of dense mitochondria this trend of association was significantly stronger.

5.4 Small glucosomes in the mitochondria-dense regions of the cell were functionally associated with mitochondria

To determine if the spatial relationship was an indication of a functional relationship, three points in the glucose metabolism and mitochondria were interrupted. First treatment with Oligomycin A was used to impair mitochondrial oxidative phosphorylation (Fig. 5). This resulted in a 55.4 $\pm$ 7.1 % reduction of glucosomes in widefield cell population studies (Fig. 16). At the subcellular level, small and mitochondria-associated glucosomes (63.5 $\pm$ 6.3 % small glucosomes associated with mitochondria) were the most significantly impacted after treatment with oligomycin (22.5 $\pm$ 8.8 % small glucosomes associated with mitochondria) (Fig. 17c,d). Other categories did not show this reduction. Large and unassociated glucosomes were not shown to be impacted by oligomycin since their distributions remained statistically similar (Fig. 17e).

Another disruption to the connection between the glucose metabolism and the mitochondria was performed using the pyruvate dehydrogenase complex inhibitor CPI 613. After 1 hr treatment at 500 nM, 82.3 $\pm$ 12.6 % (N = 74 cells) of the cells had a reduction in the number of glucosomes as observed in whole cell populations by means of widefield microscopy (Fig. 16).

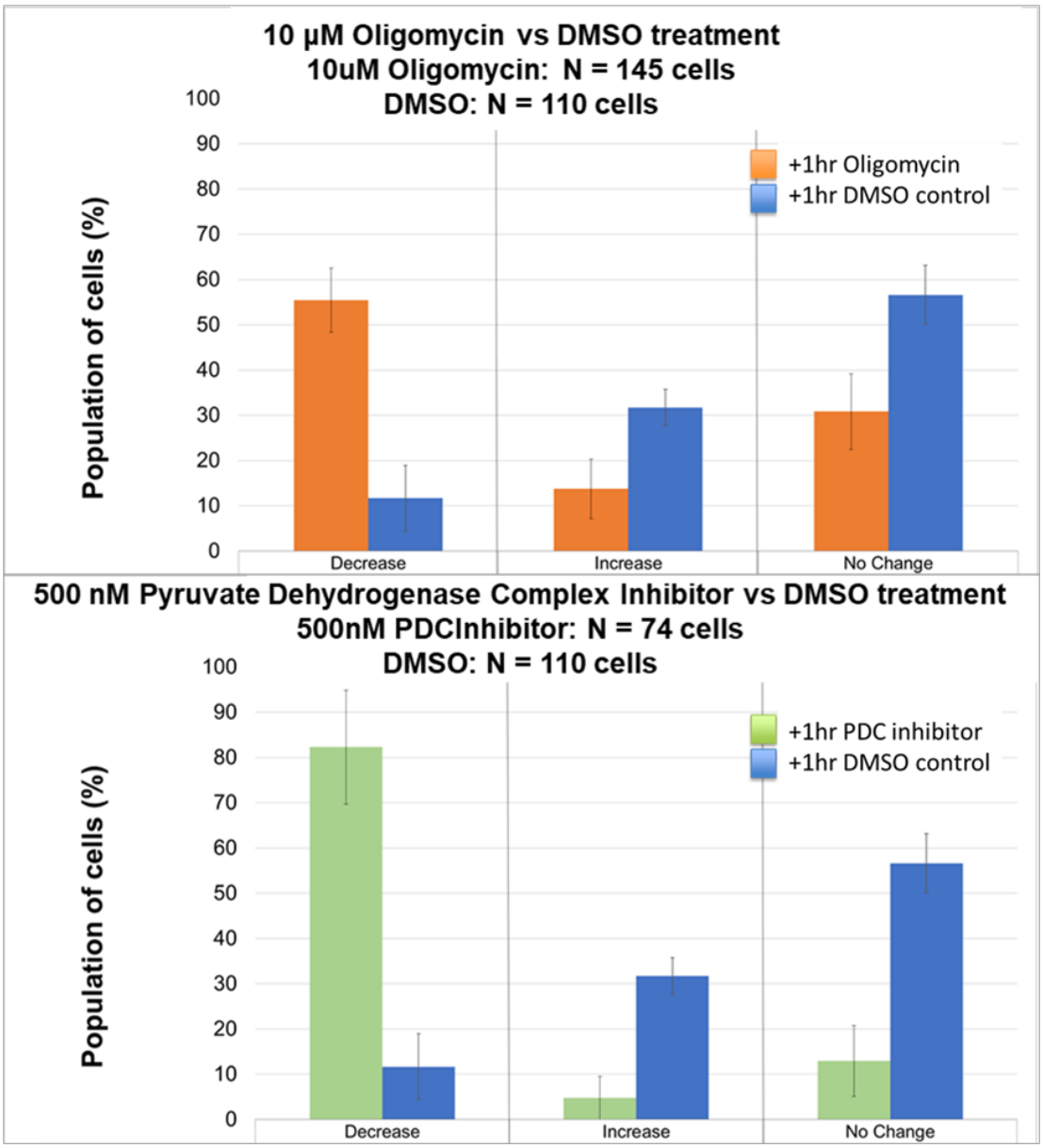

Figure 16: The impact of metabolic disruptions on the cell population using widefield microscopy. The trends of glucosomes were observed under treatment with a small-molecule inhibitor. Using 10 µM Oligomycin A to disrupt oxidative phosphorylation (top) or 500 nM CPI 613 as a pyruvate dehydrogenase complex inhibitor (bottom) cells were treated for 30-60minutes and quantified as stable if they retained the same amount of glucosomes or as increasing or decreasing if the amount of glucosomes changed during that time.

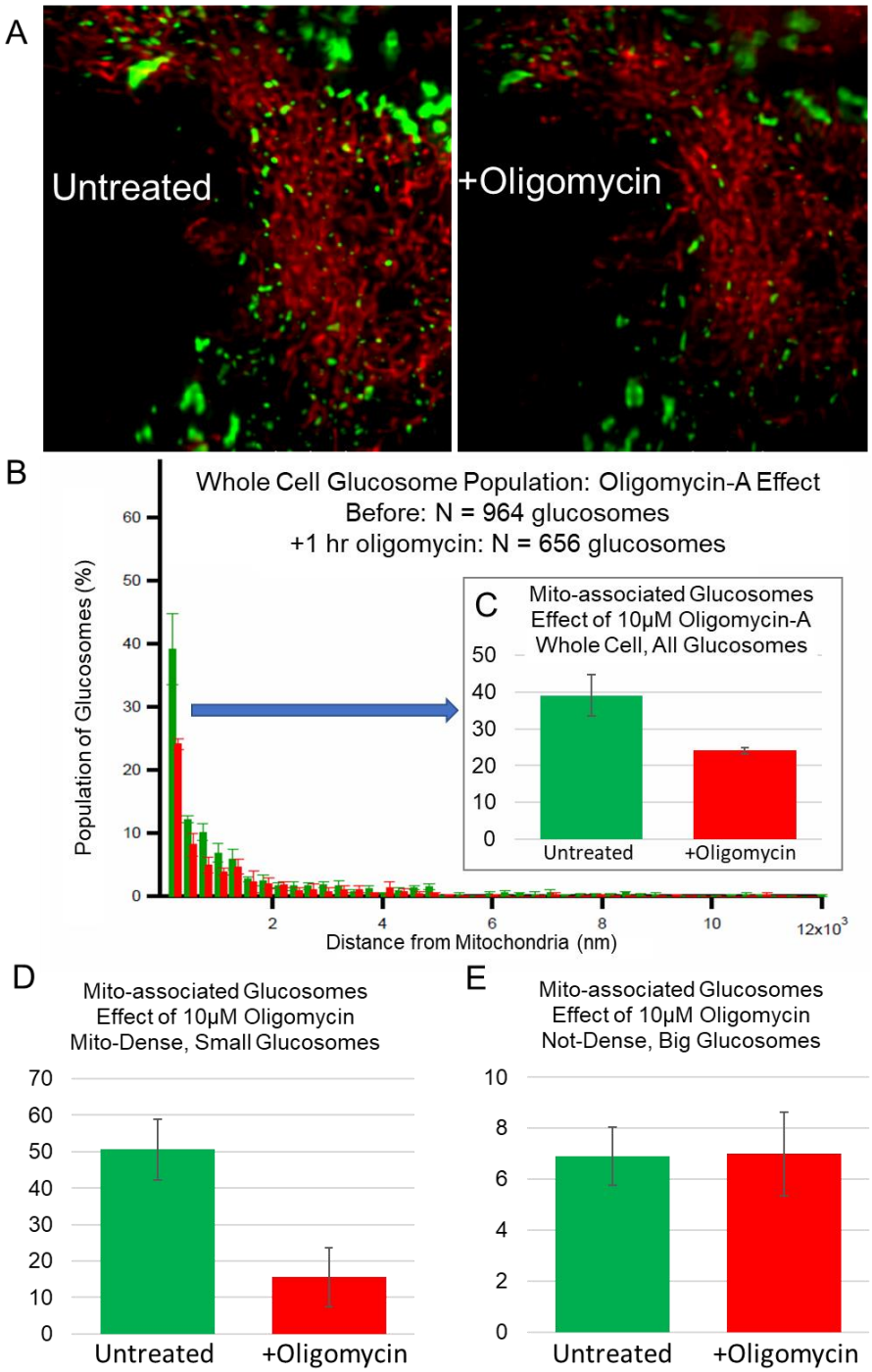

Figure 17: The impact of metabolic disruptions on the subcellular distribution of glucosomes. Treatment with 10 μM Oligomycin A to disrupt oxidative phosphorylation resulted in a reduction of glucosomes (A). The whole-cell spatial distribution showed an overall decrease in the population of glucosomes (B). The mitochondria-associated glucosomes were most effected by treatment with oligomycin (C). A drastic decrease was seen in the small-size and mitochondria-associated populations in the mito-dense region of the cell (D) while the larger glucosomes outside of the mito-dense region were largely unaffected by oligomycin (E).

The last disruption to the metabolism was performed using a knock-down cell line expressing less hexokinase 2 (HK2). This enzyme impacts the first step of glycolysis at the location of the outer membrane of mitochondria. In these knockdown cells, the small-sized glucosomes were diminished by 70.7 $\pm$ 19.0 % of cells (N = 122 cells) (Fig. 18). Altogether the functional decoupling of the mitochondria and glucose metabolism at these three points showed a critical impact on small and mitochondria-associated glucosomes, lending support to the small glucosomes directing glucose flux through glycolysis and ATP production in cancer cells.

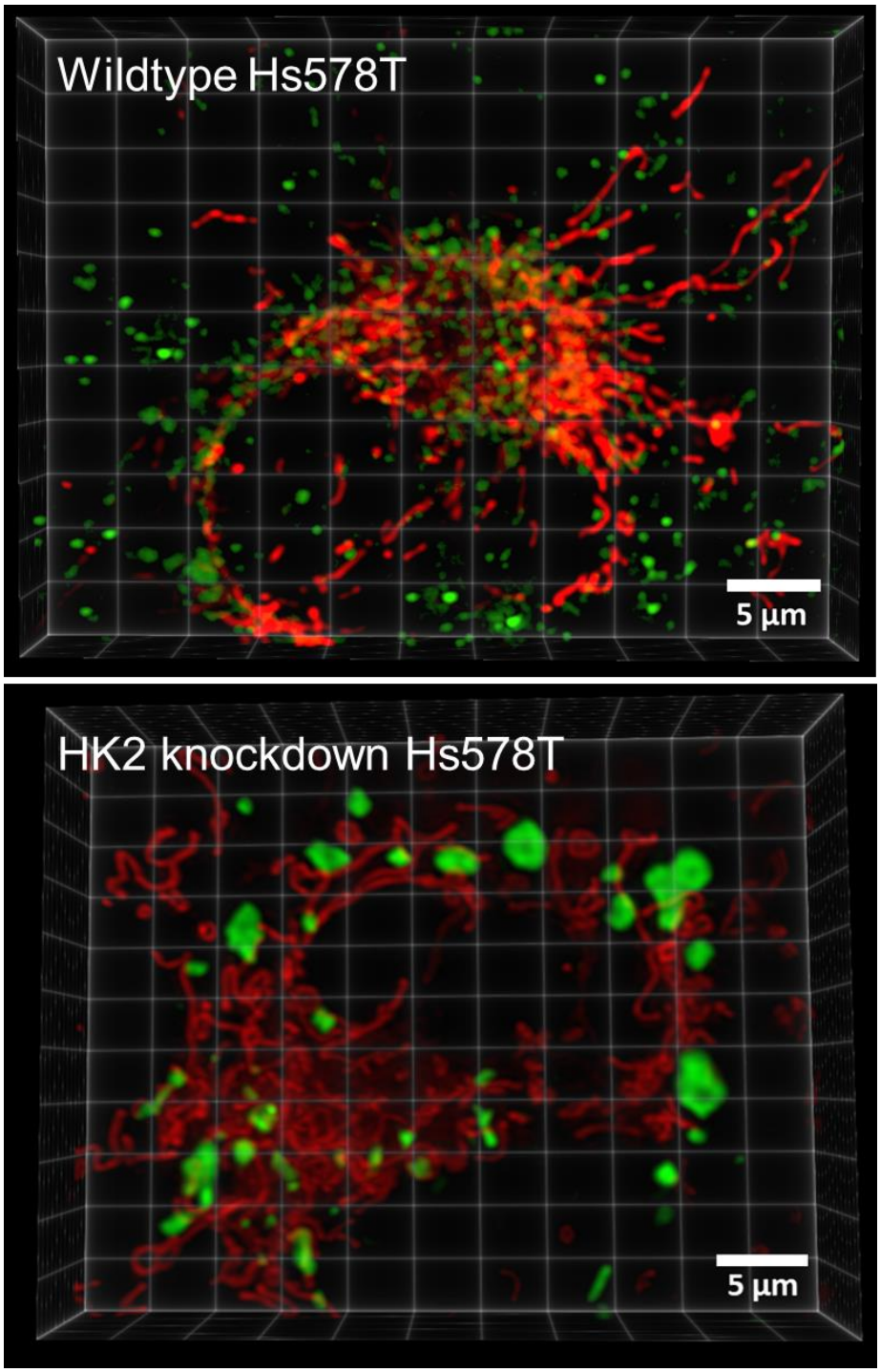

Figure 18: The impact of metabolic disruptions on the glucosome subcellular distribution using lattice light sheet microscopy. The spatial distribution of glucosomes were observed in cells expressing endogenous levels of hexokinase 2 and a knock-down level of hexokinase 2. Small-sized glucosomes were greatly reduced, but larger glucosomes were observed with increased spatial association with the mitochondria.

5.5 Discussion

This work provides compelling evidence that the spatial link between glucosomes and mitochondria is related to the functional link between the glucose metabolism and mitochondrial metabolism. These findings support that small-sized glucosomes direct glucose flux through the glycolysis pathway, which is spatially biased to the surface of mitochondria. Taken with the reports from the previous chapter, the connection between small glucosomes and glycolysis for ATP production has now been demonstrated using both functional and physical characterizations. The production of pyruvate from small glucosomes is utilized by the mitochondria, and when the mitochondria metabolism is impacted the small glucosomes are more effected than larger sized glucosomes. The spatial association of small glucosomes to the mitochondria further supports the concept of metabolic channeling between two pathways. This demonstrates that the glucose metabolism and mitochondria metabolism are functionally regulated in space and time by membraneless compartments. Demonstration of this metabolic network leads to additional questions of how other sizes of glucosomes direct metabolic flux in living cells. The development of a quantitative method to evaluate functional and spatial relationships opens the door to identifying subcellular coordination of other compartments in the cellular metabolic network.

Chapter 6: Future Direction

The cytoskeleton is an architectural organelle inside of the cell that is linked to glycolysis through interactions with phosphofructokinase and aldolase (Park et al., 2020; Hu et al., 2016). In normal cells, these interactions are a way for cells to sensitively respond to microenvironments, but in dysregulated cancer cells the high glycolytic rates are enhanced by f-actin bundling and remodeling (Park et al., 2020; Hu et al., 2016). Evidence of this metabolic coordination led to the exploration of a spatial link between glucosomes and the cytoskeleton. Here we show preliminary support of a spatial link by observing that glucosomes are highly associated with the cytoskeleton.

6.1 Glucosomes are spatially associated with the cytoskeleton

Cells were transfected with PFKL-mCherry and mGFP-EB1 to visualize glucosomes and microtubules. It was observed that 59.75 $\pm$ 5.97 % of all glucosomes associated with the microtubules (Fig. 19). Cells were also dual transfected with PFKL-mEGFP and LifeActin-RFP to visualize glucosomes and actin, and 69.51 $\pm$ 5.68 % of all glucosomes were associated with actin (Fig. 19). Taken together the high association of PFKL with microtubules and actin show a high association of PFKL with the cytoskeleton.

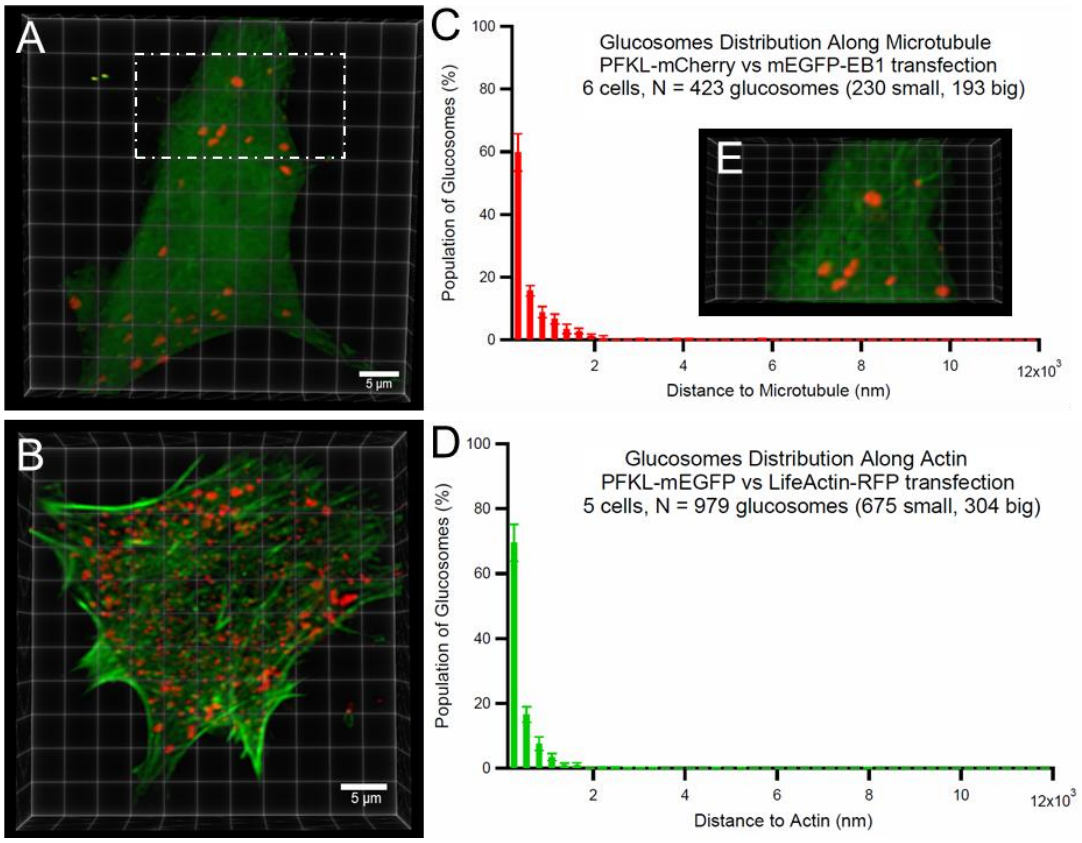

Figure 19: Histogram of all glucosomes shown as a population per cell, distributed as a measure of distance from the cytoskeleton surface. Data represents 6 cells comparing glucosomes to microtubules: 59.75 ± 5.97 % of glucosomes associate with microtubules (top). Data represents 5 cells comparing glucosomes to actin: 69.51 ± 5.68 % of glucosomes associate with actin (bottom).

Furthermore, glucosomes were evaluated for their association with either cytoskeleton of mitochondria by employing 3-color imaging. While this data showed 89.04 $\pm$ 1.76 % association of glucosomes with mitochondria or microtubules, and 75.87 $\pm$ 4.59 % of glucosomes associated with at least mitochondria or actin, the spatial distribution of glucosomes with the mitochondria changed slightly from what we had previously observed (Fig. 20). This can be seen in the 63.7 % or 53.8 % of glucosomes associated with both mitochondria and microtubules or actin, respectively, which is higher than the previously reported 37.8 % associated between glucosomes and mitochondria. This could indicate that the triple-labeling method was too toxic to the cell leading to unintentional changes to the metabolism. Better biocompatible labeling schemes should be explored.

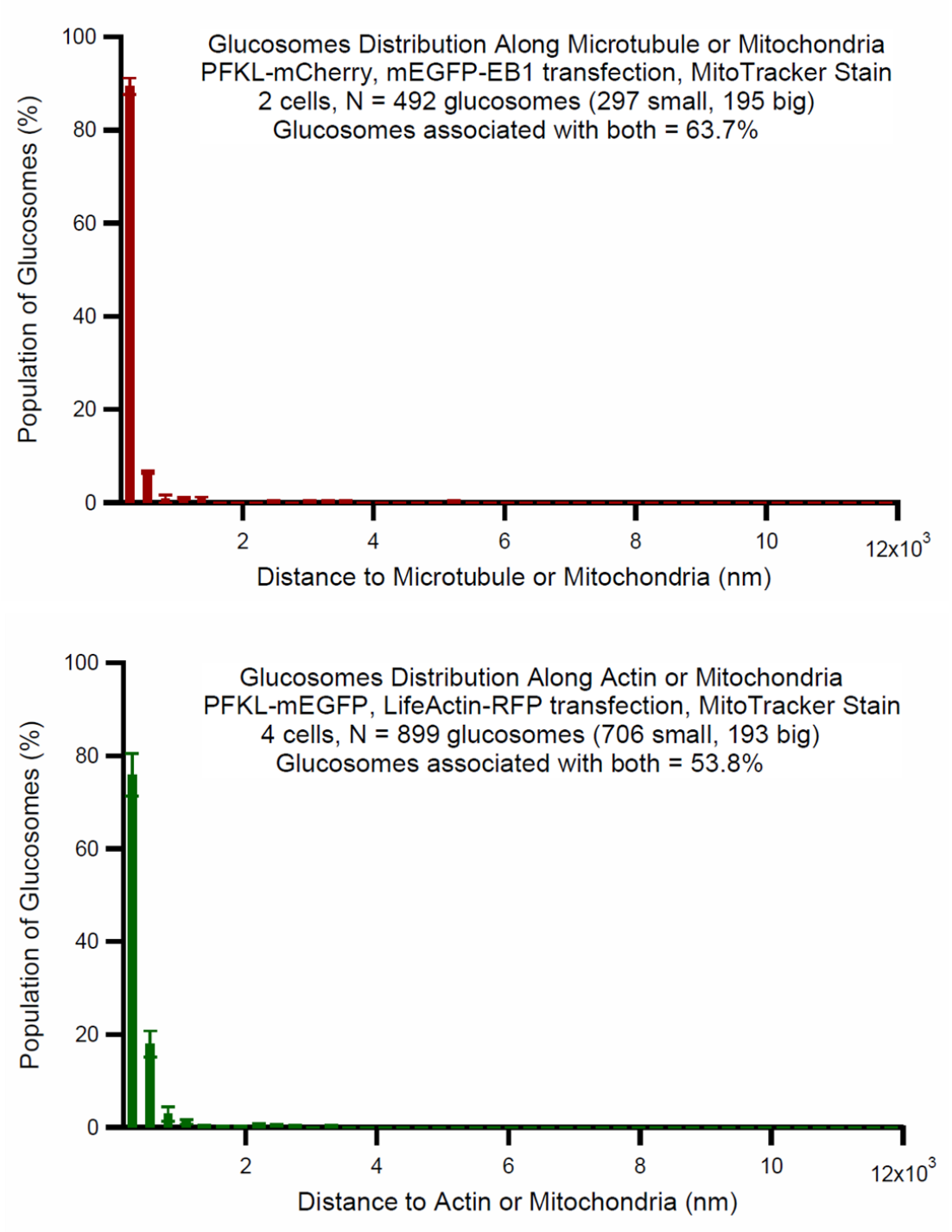

Figure 20: Histogram of glucosomes shown as a population per cell, distributed as a measure of distance from the cytoskeleton and mitochondria surfaces. Data represents 2 cells labeled with PFKL-mCherry and mEGFP-EB1, and MitoTracker DeepRed: 89.04 ± 1.76 % glucosomes associate with either mitochondria or microtubules, and 63.7 % of glucosomes associate with both. Bottom graph represents 4 cells labeled with PFKL-mEGFP and LifeActin-RFP and MitoTracker DeepRed: 75.87 ± 4.59 % of glucosomes associate with either mitochondria or actin, and 53.8 % of glucosomes associate with both.

Taken together these findings of association of glucosomes with both cytoskeleton and mitochondria demonstrate the existence of a broader metabolic network that is spatially regulated throughout living cells. These findings can be further expanded by studying the effect of functional regulation of metabolic flux between glucosomes and the cytoskeleton. Investigating additional spatial coordination with other metabolisms or organelles could serve as a basis to explore unknown metabolic regulatory mechanisms in cells.

Chapter 7: Concluding Remarks

Chapter 1 established the importance of compartmentalization for the benefit of metabolic pathways. Chapter 2 established that the glucose metabolism organizes into a spatially and functionally distinct metabolic compartment known as a glucosome. Chapter 3 showed that the formation of glucosomes is driven through liquid-liquid phase separation. Chapter 4 provided support that PFKL forms a filamentous scaffold in larger assemblies, providing insight to the internal structure of the glucosome. Chapter 5 showcased that the glucosomes have a spatial and functional relationship with the mitochondria. Chapter 6 discussed the preliminary studies that have laid the groundwork for characterizing the spatial relationship of glucosomes with the cytoskeleton. Initial observations show that the glucosomes are spatially associated with actin and microtubules.

Historically, the cytoplasmic region of the cell was considered a mixture of biomolecules with the exceptions of distinct organelles. Due to transient properties of some membraneless subcellular compartments which could not withstand harsh laboratory techniques, they were not identified until more recently with the use of live-cell imaging. The identification of metabolic compartments like the glucosome led to more questions about their purpose and mechanism of formation. Previous models of the metabolic network focused on biochemical reactions and did not account for the 3-dimensional and temporal subcellular environment of living cells. This thesis shows the responsive network of glucosome metabolic compartments as they are spatially and functionally linked to mitochondria. The size of the glucosomes has been shown to influence the spatial distribution through a specialized ratio of enzymes in the glucose

metabolism which can direct the glucose metabolism into a specific pathway. The size-specific organization supports the concept of metabolic channeling between compartments in living cells which reconceptualizes our understanding of the intricate metabolic network inside of cells with respect to compartmentalization and subcellular organization.

This thesis work also provides methodical approaches to categorizing the physical characteristics of phase-separated biomolecular compartments with 3-dimensional lattice light sheet imaging which can be applied to other subcellular compartments *in vivo*. Using 3D measures of volume and fluorescence and colocalization analysis, the partition of enzymes into subcellular compartments can be calculated and compared for various enzymes, providing insight to the composition of biomolecular compartments. Edge-to-edge vector distance analysis can quantify the spatial relationships between compartments which can be further probed to demonstrate functional relationships. By applying this quantitative approach to the evaluation of cellular response, the developed methods offer insight into the identification of metabolic diseases and effective therapies at the lab bench.

Appendix 1: Matlab script for color channel correction

```
This code is to correct color channels to the same coordinate plane

clc, clear all, close all;
fname1='[replace text with file name].tif';
info1=imfinfo(fname1);
num_images1=numel(info1);
for k=1:num_images1
     GreenChannel(:,:,k)=uint16(imread(fname1, k, 'Info', info1));
end
%
CorrectedGreenImage=imtranslate(GreenChannel(:,:,:), [X.XX Y.YY
Z.ZZ]);
%replace X.XX with x-dimension correction factor, Y.YY with y-
dimension,Z.ZZ with z-dimension
for frame=1:num_images1
    imwrite(CorrectedGreenImage(:,:,frame), '[replace text with
file name]Corr[replace text with coordinate correction
factors].tif','tif','WriteMode','append','compression','none');
end
% File will be written in the same folder used to open the image
```

Appendix 2: Matlab script for spatial analysis processing

```
This code is to calculate the vector distance between two 3-
dimensional datasets and output the vector distance of the objects
in each channel for the closest edge-to-edge

function [ RedChannel,   ThreshImage, Coordinates, CC, S,label] =
SPORT_ETE_A( fname, T, B )
% SPORT = SubPixel Ordinal Regional Correction Technique
% This Scipt is develop in collabration with S. An Lab and Kyoung
Research
% Groups. This Script is to be executed on Light Sheet Microscopy
Image for
% volumetric image processing.
warning('off','all');
fname1=fname;
info1=imfinfo(fname1);
num_images1=numel(info1);
for k=1:num_images1
     RedChannel(:,:,k)=uint16(imread(fname1, k, 'Info', info1));
end
%
ThreshImage=RedChannel;
ThreshImage(ThreshImage < T)=0;
%
Bw=im2double(ThreshImage(:,:,:));
Morph=bwareaopen(mat2gray(Bw),B);
%
CC=bwconncomp(Morph);
S=regionprops(CC,'Centroid','Area');
numPixels=cellfun(@numel, CC.PixelIdxList);
[biggest, idx]=max(numPixels);
```

```
Morph(CC.PixelIdxList{idx})=0;
%
[D1, IDX]=bwdist(Morph);
LabelMatrix=labelmatrix(CC);
Coordinates=cell(max(max(max(LabelMatrix))),1);
for i=1:max(max(max(LabelMatrix)))
    im=bsxfun(@eq,LabelMatrix,i);
    ZProj=sum(im,3);
    x_min=find(sum(ZProj,2)>0,1,'first');
    x_max=find(sum(ZProj,2)>0,1,'last');
    y_min=find(sum(ZProj,1)>0,1,'first');
    y_max=find(sum(ZProj,1)>0,1,'last');
    Z_planes=sum(sum(im,1),2);
    Z_planes=Z_planes(:);
    z_min=find(Z_planes>0,1,'first');
    z_max=find(Z_planes>0,1,'last');

    test=bwperim(im(x_min:x_max, y_min:y_max, z_min:z_max));
    bwhite=false(size(im));
    bwhite(x_min:x_max, y_min:y_max, z_min:z_max)= test;
    [x, y, z]=ind2sub(size(bwhite),find(bwhite));
    Coordinates{i}=[x y z];
end
label=bwlabeln(Morph);
end
```

Appendix 3: Matlab script of automated excel file output of spatial analysis matrix

```
This code is used to retain the object size, object coordinates,
and only the minimal edge-to-edge distance of each object in each
color channel as an output excel file

%TIF2TEXT Takes user input and .tif files, outputs text information
%regarding objects found in .tif files.

%Requires SPORT_ETE_A.m, ComputeDistance.m, and dataToText.m to run
%properly

redChannelFile = input('Please enter the name of the red channel
file.\n', 's');
redThreshold = input('Please enter the threshold used for the red
objects.\n');
redMinimum = input('Please enter the minimum red object size.\n');

[ RedChannel,   RedThreshImage, RedCoordinates, RedCC,
RedS,RedLabel] = SPORT_ETE_A( redChannelFile, redThreshold,
redMinimum);

fprintf('\nRed channel object acquisition complete.\n')

greenChannelFile = input('Please enter the name of the green
channel file.\n', 's');
greenThreshold = input('Please enter the threshold used for the
green objects.\n');
```

```
greenMinimum = input('Please enter the minimum green object
size.\n');

[ GreenChannel,   GreenThreshImage, GreenCoordinates, GreenCC,
GreenS,GreenLabel] = SPORT_ETE_A( greenChannelFile, greenThreshold,
greenMinimum);

fprintf('\nGreen channel object acquisition complete.\n')

[DistanceArray] = ComputeDistance(RedCoordinates,
GreenCoordinates);

fprintf('\nDistance array created.\n')

choice = input('\nWould you like to create an excel file or text
file? Please enter excel or text.\n', 's');

if strcmp(choice, 'text')
    DataToText(DistanceArray, RedS, GreenS)

    fprintf('\nText files generated.\n')

elseif strcmp(choice, 'excel')
    DataToExcel(DistanceArray, RedS, GreenS)

    fprintf('\nExcel file generated.\n')
end
```

Appendix 4: Matlab script to automate multi-image deconvolution in a folder

```
This code is to deconvolve multiple files in one folder using the
Matlab deconvolution processes

function LoopDeconvb(psf, background, nIter, dz_psf, dz_data, ...
    zalign, zalignParams, rotateByAngle, xypixelsize, bRotFinal,
...
    cropFinal, bFlipZ, resizeFactor, scalingThresh, varargin)

%RLdecon: Matlab function to deskew, deconvolve and rotate LLS data
%   input_folder: Folder name to pull all TIFF files for processing
%   input_tiff: input TIFF file name
%   psf: psf array in 'double'
%   background: backgroud to subtract
%   nIter: number of iterations
%   zalign: is 1 when de-skewing is needed for sample-scan data
%   zalignParams: parameters related to de-skewing [extrashift
reverse mean saveAligned]
%   rotateByAngle: angle used in deskewing and rotating final
results
%   bRotFinal: 1 to rotate the final result to make horizontal
plane
%   correspond to coverslip plane
%   zCropFinal: [lower upper] to crop the final result in Z; if
```

```
%   upper==lower then no cropping will be done

% Define a starting folder.
start_path = fullfile(matlabroot, '\toolbox\images\imdemos');
% Ask user to confirm or change.
input_folder = uigetdir(start_path);
if input_folder == 0
    return;
end
% Get list of all subfolders.
allSubFolders = genpath(input_folder);
% Parse into a cell array.
remain = allSubFolders;
listOfFolderNames = {};
while true
    [singleSubFolder, remain] = strtok(remain, ';');
    if isempty(singleSubFolder)
        break;
    end
    listOfFolderNames = [listOfFolderNames singleSubFolder];
end
numberOfFolders = length(listOfFolderNames)

% Process all image files in those folders.
counter = 1;
for k = 1 : numberOfFolders
    % Get this folder and print it out.
    thisFolder = listOfFolderNames{k};
    fprintf('Processing folder %s\n', thisFolder);

    % Get TIF files.
    filePattern = sprintf('%s/*.tif', thisFolder);
    baseFileNames = dir(filePattern);
    numberOfImageFiles = length(baseFileNames);
    % Now we have a list of all files in this folder.

    if numberOfImageFiles >= 1
        % Go through all those image files.
        for f = 1 : numberOfImageFiles
            fullFileName{counter} = fullfile(thisFolder,
baseFileNames(f).name);
            fprintf('Processing image file %s\n',
fullFileName{counter});
            input_tiff = fullfile(thisFolder,
baseFileNames(f).name);
            if ischar(dz_psf)
                dz_psf=str2double(dz_psf);
            end
            if ischar(dz_data)
                dz_data=str2double(dz_data);
            end

            if ischar(zalign)
                bZAlign = logical(str2double(zalign));
            else
                bZAlign = logical(zalign);
```

```
            end

            if ischar(rotateByAngle)
                rotateByAngle = str2double(rotateByAngle);
            end

            if ischar(xypixelsize)
                xypixelsize = str2double(xypixelsize);
            end

            bReverse = false;
            if bZAlign
                if ischar(zalignParams)
                    zalignParams = str2num(zalignParams);
                end
                extraShift = zalignParams(1);
                bReverse = logical(zalignParams(2));
                mean = zalignParams(3);
                bSaveRawT = logical(zalignParams(4));

                dz_data_ratio = sin(rotateByAngle*pi/180);
            else
                dz_data_ratio = 1;
            end

            if ischar(psf)
                [a,b,suffix]=fileparts(psf);
                if strcmp(suffix, '.mat')
                    load(psf, 'psf');
                else
                    if strcmp(suffix, '.tif')
                        psf=psf_gen(psf, dz_psf,
dz_data*dz_data_ratio, 24);
                    end
                end
            end

            if ischar(background)
                background=str2double(background);
            end
            if ischar(nIter)
                nIter=str2num(nIter);
            end


            nTapering = 0;

            for k = 1 : length(varargin);
                switch k
                    case 1
                        % number of pixel for x-y tapering
                        if ischar(varargin{k})
                            nTapering = str2num(varargin{k});
                        else
                            nTapering = varargin{k};
```

```
                        end
                    otherwise
                        disp('Unknown varargin index')
                end
            end

            rawdata = loadtiff(input_tiff);

            % rawdata = hpbuster(rawdata, background, 2, 1);

            nz = size(rawdata, 3);

            rawdata = single(rawdata) - background;

            % soften the x-y borders if requested
            if nTapering > 0
                taperKernel = fspecial('gaussian', nTapering+30,
nTapering);
                for iz=1:nz
                    rawdata(:,:,iz) = edgetaper(rawdata(:,:,iz),
taperKernel);
                end
            end

            % de-skew data if requested
            if bZAlign
                rawdata = shear3DinDim2(rawdata, rotateByAngle,
bReverse, ...
                    dz_data, xypixelsize, extraShift, 0.);
                if bSaveRawT
                    write3Dtiff(single(rawdata),
strrep(input_tiff,'.tif','_zAligned.tif'));
                end
            end

            % call Richardson-Lucy
            if nIter>0
            rawdata(rawdata<0.0) = 0.0;
            deconvolved = deconvlucy(rawdata, psf, nIter) *
numel(rawdata);
            else deconvolved=rawdata;
            end
            % Rotate the decon result if requested
            if bRotFinal
                if bReverse
                    sign = -1;
                else
                    sign = 1;
                end
                deconvolved = rotate3D(deconvolved, sign *
rotateByAngle, ...
                    dz_data*dz_data_ratio/xypixelsize);
            end

            if ischar(bRotFinal)
```

```
                bRotFinal = logical(str2double(bRotFinal));
            end

            if ischar(bFlipZ)
                bFlipZ = logical(str2double(bFlipZ));
            end

            if bFlipZ
                deconvolved = flipdim(deconvolved, 3);
            end

            % Z-crop the decon result if requested
            if ischar(cropFinal)
                cropFinal = str2num(cropFinal);
            end

            if cropFinal(2) > cropFinal(1)
                deconvolved =
deconvolved(cropFinal(1):cropFinal(2),:,:);
            end
            if cropFinal(4) > cropFinal(3)
                deconvolved =
deconvolved(:,cropFinal(3):cropFinal(4),:);
            end
            if cropFinal(6) > cropFinal(5)
                deconvolved =
deconvolved(:,:,cropFinal(5):cropFinal(6));
            end

            % construct output file name

            decon_filename_tail = '_decon.tif';
            decon_folder = 'matlab_decon/';
            thumnail_folder = 'downsampled_data/';

            output_tiff = strrep(input_tiff, '.tif',
decon_filename_tail);
            inds1=strfind(output_tiff, '/');
            inds2=strfind(output_tiff, '\');
            inds=[inds1;inds2];
            if any(inds)
                l0=inds(length(inds));
                l1=length(output_tiff);
                datafolder = output_tiff(1:l0);
                mkdir([datafolder,decon_folder]);
                output_tiff1 = strcat(output_tiff(1:l0),
decon_folder, output_tiff(l0+1:l1));
                output_tiff2 = strcat(output_tiff(1:l0),
[decon_folder,thumnail_folder], output_tiff(l0+1:l1));
            else
                datafolder = './';
                output_tiff1 = strcat(decon_folder, output_tiff);
                output_tiff2 =
strcat([decon_folder,thumnail_folder], output_tiff);
            end
```

```
            write3Dtiff(deconvolved, output_tiff1);

            % generate thumbnails in "downsampled_data"
            if ischar(resizeFactor)
                resizeFactor = str2double(resizeFactor);
            end

            if ischar(scalingThresh)
                scalingThresh = str2double(scalingThresh);
            end

            if resizeFactor ~= 1
                deconvolved = rescale_resample(deconvolved,
resizeFactor, scalingThresh);
                mkdir([datafolder,decon_folder,thumnail_folder]);
                write3Dtiff(deconvolved, output_tiff2);
            end
             counter = counter+1;
        end
    else
        fprintf('Folder %s has no image files in it.\n',
thisFolder);
    end
end
```

Appendix 5: Protocol of daily operation of the lattice light sheet microscope

Daily maintenance of LLSM is necessary to obtain useable data.
Protocol developed for use in Kyoung Lab: focus on eliminating bleedthrough and cross-talk illumination.
Notes:

- If LLSM is in daily use, maintain objectives in water in the sample chamber to reduce alignment shifting.
- Ensure no corrosion or film in sample chamber. It is a sign of damage to the coating of the objectives. Do not operate until repaired.
- Yearly login to Matlab are necessary with university license using a university email address.
- Powering ON must go in the listed order of Step 2, and Powering OFF must go in the reverse order. This will avoid damage to electronic components and proper connection with the computer.

1. Getting started: Sample holder must be removed from sample chamber. Piezo stages cannot be calibrated while sample holder is in sample chamber or damage to objectives and piezos will occur.
2. Turn on electric components in order: (* = May be left running indefinitely)
   2.1. *Acopian custom power supply, located at bottom of computer tower
   2.2. *Galvo adapter, located above Acopian power supply on computer tower
   2.3. *SIM9000 AOTF controller, located below computer on computer tower
   2.4. Computer, located on tower. Login before proceeding.

2.5. Camera: Hamamatsu ORCA Flash, located on microscope table. Wait for orange light to signal connection with computer is ready.
2.6. SLM power supply, located on microscope table. Allow 10 seconds to stabilize as seen by a slight increase to AMP readout. Readout should be between 27-34 AMP. Iff lower (~19AMP) power cycle the SLM power supply.
2.7. Power supply for all piezo stages, located underneath the microscope table.
2.8. Laser power supplies, located on computer tower or below microscope table. Can be turned on separately. Load the laser controller GUI and select the correct COM port connection through the computer. Wait for lasers to reach stable temperature before proceeding.

3. Begin the program to run the LLSM-SPIM software. This will detail the Labview operation, but it is possible to operate via an executable program (also downloaded)
   3.1. Ensure lasers are correctly assigned to the COM ports in the computer by noting the bottom line text in the GUI visual.
      3.1.1. 488 laser = COM1
      3.1.2. 560 laser = COM6
      3.1.3. 639 laser = separate laser/computer interface program. Switch from 'remote' to 'local' to use computer control settings
   3.2. Start the Labview program by clicking on the LLSM labview icon.
      3.2.1. Wait for libraries to load
      3.2.2. Click 'SPIM LV' folder and choose 'SPIM MAIN.vi'
      3.2.3. Wait for additional libraries to load
   3.3. Press play arrow to initiate SPIM program.
      3.3.1. This will query electronic connections and the status bar will read 'Connecting with FPGA' and eventually 'Ready'
      3.3.2. Piezo stages will reference: SAMPLE HOLDER MUST NOT BE IN SAMPLE CHAMBER
      3.3.3. Open 'Motion Console' from the Utility tab and observe piezo stages have correctly referenced. Positions will be ~9 for X and Y stages. Z will be ~5.
         3.3.3.1. If incorrectly referenced, exit program and reload. If error still occurs exit Labview and power cycle the piezo stages only.
      3.3.4. Set piezo stage movements to 0.5um stepsize and 30nm/us speed for XY piezos. Set stage movement to 0.5um stepsize and 10nm/us speed for Z piezo stage
      3.3.5. Lower Z-piezo to ~9.5um position to prepare for sample holder. This position should be lower than the objectives to safely load sample holder. If too close to the objectives, re-evaluate major alignment and stage position before proceeding. (It may not be wrong but check well to avoid damage to piezos and objectives)
4. Align the lasers roughly using the t-shirt shaped alignment tool
   4.1. Align the first laser channel by making minor adjustments to the microscope lens components.

4.1.1. Use ‘Continuous Scan’ mode, without dithering the galvos, with single Bessel beam pattern loaded in the SLM.
4.1.2. Set t-shirt tool between the last cylindrical lens and before the SLM.
4.1.3. Adjust prism/mirror after first cylindrical lens so laser beam is well overlapped with vertical line on t-shirt tool.
4.1.4. Adjust hidden mirrors below the SLM to ensure that the beam after the t-shirt tool is well centered on the SLM pattern
4.1.5. Turn on the Guppy Camera and fold down the flip mirror before the Back Focal Plane gluppy.
4.1.6. Use mirror knobs on protruding arm before the annular mask to ensure that the single Bessel beam is well centered on annular mask
4.1.7. Use T-shirt tool prior to bottom protruding arm before the objectives and before the guppy. Adjust mirrors on the protruding arm and prism stage translation prior to illumination objectives. Ensure that the back focal plane image is well centered at the protruding arm, and entering the BFP Guppy camera.
4.1.8. Raise flip mirror prior to illumination objective.
4.1.9. Load fluorescent dye solution into the sample chamber. Observe the shape exiting the illumination objective. There should be a cone of illumination that looks like an hourglass. Use the flip mirror knobs to adjust the shape to a roughly symmetrical shape.
4.1.10. Watching the LLSM computer camera channel, gently adjust the detection objective travel stage to bring the illumination into focus. The result should be a strong central Bessel beam with several beams above and below it (beams travel along the x-dimension in the camera so additional weaker beams will be above/below in the y-axis).
4.1.11. If beams are uncentered in the x-dimension, gently move the travel stage of the illumination objective
4.1.12. Ensure that there is visibly space between the illumination and detection objectives. If not, adjust the position of the detection objective and then use the flip mirrors to slightly change the direction of the focus through the illumination objective. Repeat as necessary.
4.1.13. If beam is crooked in the X- and Y- planes of the computer camera, use the mirror knobs on the protruding arm before the objectives to adjust slightly. The outer pair of knobs are partnered. The inner pair of knobs are partnered.
4.1.14. Change the LLSM scanning mode to a z-stack continuous. Do not dither the galvos. Do not move the detection objective (Z-piezo objective stage).
4.1.15. Draw two thin-vertical rectangles on the right camera screen so that the left and right ends of the Bessel beam are each inside one rectangle.
4.1.16. Observe the Stack intensity and adjust the travel stage of the flip mirror so that the left and right sides of the Bessel beam focus and defocus at the same time to achieve orthogonal illumination plane.

4.2. Align addition laser channels

4.2.1. The next laser channels are adjusted only by moving the prism stages or mirrors on the individual laser channels at the laser combiner. Make small adjustments to observe that they are well overlapped at the SLM and then at the annular mask with the BFP guppy. Any minor plane focus differences will be adjusted with the channel specific galvo offsets later.

5. Precisely align the color channels using the z-galvo calibrations
   - 5.1. Prepare the beads solution by using sonication to break up resting beads. Do not heat. Sonicate ~5-10minutes.
   - 5.2. If necessary, dilute beads ~10x-100x using autoclaved filtered MilliQ water. These beads will also be added to cell solution so maintain good laboratory practices to avoid contamination
   - 5.3. Place a droplet of bead solution on a clean sample cover glass. Allow to rest for 10minutes. Beads will adhere to the glass surface automatically.
   - 5.4. Load bead-coverslip into sample holder.
   - 5.5. Gently add sample holder to the sample chamber with a downturned motion by aligning the pins in the rectangular portion with the pin-holes on the sample-piezo stage. Finger-tighten a screw to the sample holder and piezo. DO NOT OVERTIGHTEN. It will damage the piezo.
   - 5.6. Use the motion console to raise the coverslip with beads into the illumination plane. This will be observable with a dark vertical line and spots of bright illumination. A typical position in the motion console is around 8.7, 8.7, 8.7 for X, Y, and Z stages
   - 5.7. Once a bead is in focus, position it to the center of the camera using the stage step jog. Reduce camera ROI size to 64x64 ROI and centered on the bead.
   - 5.8. Ensure the z-galvo and Channel galvo settings are all set to 0.
   - 5.9. Using the ‘Autofocus Bead’ acquisition mode, scan each of the channels and record the specific z-galvo positions. Use these values to set the AOTF channel-specific z-galvo calibrations. Repeat the Autofocus scan one more time to set the autofocus of the entire microscope.
6. Obtain the daily point spread function (PSF)
   - 6.1. Switch acquisition to the ‘Z-stack’ single scan mode, dither (step size 100nm), and move z-galvo and z-piezo (objective) together in matching step sizes
   - 6.2. Center bead, ensure the AOTF is set to the correct channel, and the correct filter set is allowing the correct beam through.
   - 6.3. Acquire and save stack with the proper label
   - 6.4. Repeat for any additional laser channels
7. Before imaging, rinse chamber well by using MilliQ water (3x), 1X BSS buffer (3x), Imaging media (typically 1X BSS) (3x)
8. Throughout imaging it will be necessary to repeat the Autofocus bead to correct the small changes to the system. This is the global galvo setting and not the color channel corrections. The color channels should retain their offsets in relation to each other.

Appendix 6: Protocol for deconvolution and data preparation

This protocol is to standardize data handling from the LLSM microscope. Experimentation determined that 20 iterations of Richardson-Lucy deconvolution was sufficient and did not induce artifacts in the data.
The angle of illumination is determined during the major alignment but can be quickly checked by forming a 3D Project stack along the Y-axis. At the slice where the bead is the widest, draw several lines from the tip of one bead to the next and measure the angle. It should be close to the measured angle during the major alignment, but small variations may accrue over time. If deconvolved data appears to travel along the x-axis it is possible that the deconvolution angle needs to be adjusted.

1. Sort data into folders depending on the detection wavelength and illumination pattern used
2. Open to the folder containing the LoopDeconvb.m Matlab project. This will loop the parameters for all images within a folder using the RLdecon.m file obtained from the Betzig lab
3. Adjust the pathway of the point spread function to match the point spread function collected for the day
    3.1. The point spread function file cannot be in the looped deconvolution folder or else an error may occur
4. Ensure that the angle of deconvolution, the wavelength, the magnification, and any other factors are correctly set based on the experimental parameters determined during the major alignment
    4.1. Time and memory can be saved by reducing the Zmin and Zmax stack slices but be careful to capture the entirety of the data in the cropped dimensions.
5. Run the Matlab program and select the folder that includes the data of interest.
6. Repeat with any remaining color channels
7. An example of the dataset parameters follows:
    LoopDeconvb('c:\...\DailyPointSpreadFunctionStack.tif', 100, 20, .100, .187, 1, [0,0,0,1], 31.5, .104, 1,[0,0,0,0,120,240], 0)
    This will treat all datasets in the selected folder with the Daily PSF, subtract 100 background counts, perform 20 iterations of Richardson-Lucy deconvolution, 100nm stepsize of the PSF, 187nm step size of the sample piezo, perform z-alignment, [no extrashift, no reverse, no mean, save the z-alignment], deskew at an angle of 31.5 degrees, magnify 1 pixel dimension to 104nm, rotate the final image, [auto Xmin, auto Xmax, auto Ymin, auto Ymax, 120 Zmin, 240 Zmax], no varargin.

Appendix 7: Protocol for 3D Object Counter processing in ImageJ

This protocol is to standardize spatial analysis. This process will take time and consultation with other lab members and past datasets. It is important not to over-

estimate or underestimate the dimensions of subcellular bodies, but also utilize segmentation methods which are not as sensitive as the human eye.

1. Covert datasets to 16-bit so that they maintain intensity information aligned with the range of the Orca Flash camera in use on the LLSM.
    1.1. Open the 32-bit padded datasets post-deconvolution using ImageJ
    1.2. Use the Autofocus→Reset feature and verify that the intensity range is between 0-65535. If not, navigate to the brightest point in the 3D sample and select Reset again.
    1.3. Save file as 16-bit in a folder that is easy to navigate and clearly marks the date of data collection. It may be useful to trim the data title, but be sure to include the Cell Name, date, time, color channel, laser intensity, camera exposure, and any identifying experimental features.
2. Perform necessary spatial correction on different color channels
    2.1. Open the images and combine then with the Image→Color→MergeChannel option.
    2.2. Isolate a TetraSpeck™ fluorescent bead and crop around it.
    2.3. Separate the color channels and use the 3D Objects Counter to quickly segment the bead. The automatic threshold selection will typically be sufficient.
    2.4. Use the centroid measurements to find the difference between the different color channel beads
    2.5. Use these x-, y-, and z-offsets as the correction parameters in the ImageCorrection Matlab project.
    2.6. Save the resulting file with the correction factor.
    2.7. To reduce influence on glucosome size data, it is best to adjust the non-glucosome color channels whenever possible. This allows the intensity, volume, and integrated intensity values to remain unchanged for glucosome datasets.
    2.8. Image color channel correction should never be performed on anything by the raw data files. It is particularly artifact-prone for 8-bit binary files like the segmented files and should never be applied to those due to changes in volume of the objects.
3. Segment the 16-bit globular bodies files using ImageJ
    3.1. With the image file open in ImageJ, navigate to the Analyze→3D OC Options.
        3.1.1. Ensure that all Parameters to Calculate are turned on. If memory is an issue, it is necessary to calculate Volume, Integrated Density, and Centroid.
        3.1.2. Neither Image Parameters are necessary, but images may be closed while processing to save memory.
        3.1.3. Turn off the Maps' parameters so that numbers do not appear in the objects map.
        3.1.4. ResultsTable Parameters may also be left off.
        3.1.5. Do not Redirect the objects map.
    3.2. Navigate to Analyze→3D Objects Counter and a user interface will pop up

3.2.1. Adjust the threshold so that the entire edge of the objects of interest are captured. First focus on the brightest objects to determine the maximal threshold. Medium threshold is about ½ this value. Smallest threshold is about 1/3 to 1/8 of the maximal threshold value.

3.2.1.1. Minimal size threshold is 15 voxels (as experimentally determined by 3 standard deviations from experimentally acquired 100nm fluorescent beads).

3.2.1.2. Maximal threshold is left unlimited when using the maximal threshold. It is set to 500 voxels for the medium threshold, 135 or 65 voxels for the smallest thresholds.

3.2.1.3. All listed parameters are generalized for the PFKL identification of glucosomes. It is necessary to optimize the same general parameters for each fluorescent probe

3.2.2. It may be necessary to crop the image into regions with high background and low background in order to more easily identify the objects with high sensitivity and low artifacts

3.2.2.1. Use the Polygon Selection tool in ImageJ to draw those regions and save to the Analyze→Tools→ROI Manager.

3.2.2.2. Duplicate the 3D dataset and apply the ROI to both images.

3.2.2.3. Use the Edit→Clear or Edit→ClearOutside and apply to all slices in the stack.

3.3. Recombine the analyzed Objects Maps by using the Image→Color→Merge Channels option. Then select Image→Type→RGB Color to combine the channels into one. Then Image→Type→8-bit.

3.3.1.1. Adjust the Image→Adjust→Brightness/Contrast so that the file is a binary 8-bit files and save this by adding '3DOCMap' or similar label to the file title.

4. Segment the 16-bit files using Allen Center Cell Segmenter Tool

4.1. Installation and operational instructions can be found via the bioRxiv preprint paper and website: https://www.allencell.org/segmenter.html

4.2. Open the Allen Center Cell Segmenter notebooks through GitHub by utilizing Anaconda Prompt window.

4.3. Command ">activate segmentation" and observe that the program says "(segmentation)"

4.4. Navigate to the correct folder containing the 'lookup_table_demo' by typing '>cd C:\...\aics-segmentation\lookup_table_demo' and substituting the correct folder pathway as set up during installation

4.5. Launch the jupyter notebook which will prompt a web browser to open to the code on GitHub by typing ">jupyter notebook"

4.6. Utilize the Lookup Table on the website to determine which notebook best suits the needs of the project.

4.6.1. For example, playground_filament3d is an appropriate notebook for structures like actin and mitochondria.

4.7. Substitute the image filename and location as directed in the form 'D:/Folder Location/…/filename.tif'

4.8. Again referencing the lookup table, decide which parameters are a good first iteration of the Pre-Processing steps. Substitute those numbers as directed.
  4.8.1. Process the image through this step to obtain recommended scaling parameters. Those may be substituted before proceeding.
4.9. The lookup table will also recommend parameters to apply for the Core Algorithm Filter.
  4.9.1. These filters will need to be adjusted multiple times to optimize the segmentation
4.10. Ensure that the program will save a processed file by confirming there is an active code line reading 'final_seg = final_seg >0'. Other code may vary in this section depending on the notebook, but any save-file errors may be explored here. Rename the filename and location in the format 'D:/Folder Location/…/filename_ACSf3dv1.tiff'
  4.10.1. Each iteration will require an update to the filename number to avoid overwriting the previous file.
  4.10.2. Parameters will not be saved automatically, so use the Print Preview screen to easily record the parameters used to obtain each segmentation
4.11. The final output is a binary 8-bit file that can be used as a mask to be applied in ImageJ over the raw datafile, or in Matlab as the object map file for the 3D spatial analysis

Appendix 8: Protocol for performing 3D spatial analysis

This protocol is to perform the spatial analysis which is a comparison of the surface of all objects in one channel to the nearest object in the other color channel.

1. This protocol requires the binary objects maps and the SPORT_ETE matlab project
   1.1. An update to the SPORT_ETE file includes the generation of excel datasets automatically which greatly speeds the process of spatial analysis
2. Run the simplified spatial analysis Matlab project.
3. Input the green channel object map when prompted. Since this is a binary object map, select 1 as the minimal threshold and 1 as the minimal voxel size.
4. Repeat for the red channel as prompted.
5. Wait for the generation of a matric dataset.
6. Select method of file saving when prompted. Typically an Excel file is easiest.
7. Type the name of the file followed by '.xlsx' for Excel files.
8. Open the excel file and identify the glucosome sheet based on the object number which was found during the object map generation.
9. The third Excel sheet will contain a matrix of the distances of all glucosomes compared to all objects of the other channel. The minimum distances per object are the bottom-most row and the right-most column.
10. Copy and paste the distances into a new column next to the glucosome datasheet.

11. Use the Histogram function to bin the dataset with the appropriate size. Since 275nm was observed to be the average point spread function measurement, it was used as the distance bin size.
12. Subcategorize by selecting for glucosomes of a certain volume or a certain region of interest in the cell. Both of these identifiers are found in the excel sheet with the "Area" or volume column, and the centroid columns.
13. It is most appropriate to compare the whole-cell behavior of cells. This is why the population of glucosomes in cells is what is combined for analysis.

Appendix 9: Protocol for semiannual major alignment

This protocol is to perform the 4–6-month major alignment needed for optimal illumination with the LLSM.

1. Microscope deconstruction
    1.1. Prepare a clean, dust-free workspace to keep the protected lenses in order
    1.2. When applicable, remove all lenses and keep them ordered as they should be placed along the laser pathway
    1.3. For the lenses just after the lasers, it is easiest to remove the entire cage system that focuses the light. These may be immediately replaced with a small alignment procedure as follows:
        1.3.1. Place a mirror so that the light is reflected some distance away. Remember to angle the mirror so that there is no chance the laser will be reflected into any person's eyes. Follow all laser recommended protocols of safety and keep laser output low.
        1.3.2. Unscrew the lenses from the cage system and remount the cage system with the lens adaptors already on the metal pegs. Use the t-shirt tool to note where the laser lands without lenses, and mark where the laser lands as it is reflected on the wall.
        1.3.3. Add in the lens in the adaptor closest to the laser and confirm that the beam is not clipped by the edge of the lens (ringed pattern). Place the T-shirt at a distance to see the focus of the beam and use the knobs on the lens holder to center the beam.
        1.3.4. Add the second lens into the mount and slide the mount so that the beam is made collimated. This can be judged by the equal size of the beam near the lenses and far away as well as observing there is no point of focus within the laser pathway between those points
        1.3.5. Use the knobs on the second lens to re-direct the collimated beam to the marking on the wall.
        1.3.6. Ensure that there is no clipping of the beam through the lens pair and proceed with alignment. This lens pair acts to collimate the laser through the entire travel path of the lattice microscope, so it is best that they are added before all other lenses even though the general rule of lattice light sheet alignment is to add lenses closest to the sample plane first.
    1.4. Remove objectives, sample chamber, piezos, and annular mask and keep them safely stored

1.5. Redo the silicon seal on the sample chamber
    1.5.1. Remove all screws
    1.5.2. Scrape away old silicon.
    1.5.3. Pry the covers away from the pieces of the sample chamber and remove internal silicon
    1.5.4. Wash well with a gentle brush so as not to scratch the metal surfaces. Rinse well with DI water and dry thoroughly for strong silicone reapplication
    1.5.5. Add dots and lines of silicone along the edges to prevent water from leaking out of the sample chamber. If using the sample chamber with liquid flow-through, ensure that the tubing and connections are clean of buildup and leak-free. If using the sample chamber as a stagnant pool of media, stopper the inlet and outlet holes in the bottom of the chamber with silicone.
    1.5.6. Add dots of silicone and a fresh glass piece (Warner Instruments, 12mm round CS-12R glass). Press gently to seal the glass into the ridge at the bottom of the sample chamber.
    1.5.7. Wait for the sample chamber to cure for 24hrs and ensure that it does not leak. Repeat the cleaning and sealing process to ensure no mold grows in the sample holder. DO NOT try to cover holes as it will trap water inside that can weaken the silicone seals and leak during experiments

2. Alignment without lenses
    2.1. Throughout the following procedure work in pairs of reflected optics. Stage translations will adjust the position of the laser beam nearby while angle knobs will adjust the position of the laser beam far away. When working with pairs of angle knobs, consider that the final goal is to have the laser beam with consistently straight pathway with ~90-degree angles at reflected surfaces. The microscope uses rigid structures which are useful for consistent illumination and provide a limited range for alignment using the T-shirt and centering tools. Pieces of laser paper are also useful for tracking the beam through the microscope pathway but do not scrape sensitive equipment or lenses.
    2.2. Using the T-shirt tool work from the collimated laser through the Epi-objective pathway with the flip mirror lowered. The AOTF must be directed to allow the laser channel through. Failure to do so will result in the alignment of the wrong order of light and complete misalignment of the system.
        2.2.1. Utilize the placement of irises and adjust the knobs or travel stages on mirrors to direct the laser beam through the AOTF in a way that the right-side 1st order beam is not clipped, patterned, and has good output efficiency
        2.2.2. Ensure that the laser travels on a consistent z-path and utilize the T-shirt tool in the Epi path cage system.

2.2.3. Observe the position of the beam and add back the Epi Objective lens. Use the translational stages to navigate the Objective into a parallel position that does not bend the laser beam.

2.2.4. Add a droplet of Immersol W objective oil which is formulated to be like the refractive index of water. Replace and secure the clean and resealed sample chamber bottom and ensure that the objective is not pressing on the glass coverslip in the bottom.

2.2.5. Gently raise the objective so that the droplet of Immersol spreads along the bottom of the sample chamber glass coverslip.

2.2.6. Add in the other lenses and ensure that the light path does not change. If it does, adjust the translational knobs on the lens adapters so that the center of the lens is positioned exactly intersecting the laser beam.

2.2.7. Fill the sample chamber with a dye solution and observe that the focus of the Epi pathway is balanced and not tilted. Minor adjustments may be necessary at the Objective lens translational stages.

2.3. Alignment through the plane illumination pathway

2.3.1. Flip the mirror up

2.3.2. Use the T-shirt tool and the 12.5mm small round target tool to ensure that the laser beam is centered until just before the SLM.

2.3.3. Starting with the translational and angle knobs on the flip mirror work to keep the beam centered and with 90-degree angles.

2.3.4. Run the SLM MetroCon program to project a single Bessel beam, exactly centered on the SLM. There are angle knobs hidden below the polarized beam splitting cube that are used to center the beam exactly on the pattern.

2.3.5. Carefully and minimally adjust the knobs on the back of the SLM. If too much pressure is applied the SLM could be damaged. Do not pass the limitations of the angle knobs. Any un-centered imperfection can be compensated for in the next steps

2.3.6. Aim for 90-degree angles in the protruding arm before the annular mask holder. There is an iris mounted on the mirror cage just after the annular mask that can assist

2.3.7. The next steps require that the lattice light sheet microscope be running, so reinstall the piezo stages since the Epi objective and sample chamber are already reattached. Disconnect from SLM MetroCon and return AOTF control to the computer program (External Mode). Open the LLSM SPIM file as normal.

2.3.8. Loosen the screws on the galvo mirror holders and wear gloves to gently turn them as needed for optimal alignment. The small round alignment tool is useful at this step as well as the T-shirt tool placed before the Sample Guppy preview camera.

2.3.9. The final protruding arm has two mirrors that will also compensate for any angular misalignment. Ensure that the laser is at optimal 90-degree angles on those mirrors to start, but they will likely not remain

that way. The beam splitting cube makes a big difference in final focus position so ensure that it is well centered.

2.3.10. Keep the flip mirror near the objective down and align the laser through the Back Focal Plane Guppy preview camera. The lenses on this guppy preview camera are not necessary to remove, but if they are, replace them so that the first lens focuses the beam onto the camera, and the second lens collimates the beam. This will mimic the optimal positioning of the illumination objective.

3. Aligning the digital controlled optics
    3.1.1. Using gloves, gently push in the galvos so that the edge of the mount is visible in the camera (it will be hard to see until lenses are placed but a shadow may be seen). DO NOT push the galvos in too far as the corners will catch on the cage and damage the galvos. Use a flashlight to ensure that you are safely moving them a small amount. Also ensure that the angle does not change by observing the laser beam pathway.
    3.1.2. Add in lens closest to the objective (prior to the flip mirror) and position it so that the laser beams focus on the camera. Adjust any translational positions so that the lens is well centered over the laser pathway.
    3.1.3. Add in the next lens which occurs between the sample camera splitting cube and the galvo. Adjust the position of this lens along the cage system so that the edge of the galvo mount is brought into clear focus on the camera. This is how the back focal planes are conjugated on the galvos so that there is no blurring of the lattice light sheet while dithering or scanning. It is critical that the back focal plane is on the galvo surface.
    3.1.4. Similarly work backwards to add the lens for the previous galvo
4. Placing annular mask
    4.1.1. Add in the annular mask to the holder and use the iris to ensure that the annular mask is well centered
    4.1.2. Add lenses back to the annular mask and observe the edge of the annular mask for a crisp focus. Note that the annular mask, galvos, and back focal plane preview camera are all conjugate with the back focal plane of the illumination objective. There will be focal points in between these surfaces in the laser pathway that form the sample plane.
    4.1.3. With a glove, gently pull out the galvos so that the edge is not visible inside of the annular mask and ensure that the alignment of the beam has not changed. Move one at a time carefully to avoid ruining alignment.
    4.1.4. The SLM is the sample plane that imprints the pattern. There is one lens added to the pathway between the annular mask and the SLM on the protruding arm. Move this lens into position until the illumination of the annular mask ring is crisp. This lens is large and can minorly impact alignment so after addition it may be necessary to change the

lower mirror on the extruding arm with the annular mask to adjust for this minor pathway change. The annular mask is well aligned, so trust that position as fixed.

5. Objective placement
   - 5.1. Before installing the objectives, it is necessary to turn off the piezo stages so that there is no electronic signal passing through the objective piezo when loading it. Search for any damage to the objectives by examining their surfaces and the protecting sealant in the water-dipping portion. Turn on the microscope as usual once the objectives are placed.
   - 5.2. Move the objective holders far from each other using the translational stages. Move the objective stage higher away from the sample chamber using the translational stage knob near the Back focal plane guppy.
   - 5.3. Put the adapter on the objectives, and then mount the adapter onto the translational stage or piezo holes as necessary. DO NOT try to screw the objectives into the mounted adapters because it is too easy to mishandle the objectives in this order.
   - 5.4. Dry the sample chamber and place an objective lens paper on the bottom of the chamber as a buffer between the objectives and the bottom of the sample chamber.
   - 5.5. Begin to move the objective lenses towards each other and place a lens paper between them. By eyes, the objectives should be visibly separate but close. The lens paper should be able to move in between them
   - 5.6. Lower the objectives stage and make sure that the lens paper can easily move. The stage may need to move up and down during the sensitive alignment so raise the stage slightly to have more room to adjust later. If an objective is touching the bottom, then the piezo or objective can be damaged so be mindful of this in the next steps.
   - 5.7. Remove the lens papers
6. Alignment with dye solution
   - 6.1. Add dye to the sample chamber.
   - 6.2. Flip up the mirror behind the illumination objective.
   - 6.3. Use the translational stage and knobs on the flip mirror to straighten the beam as it focuses out of the illumination objective. Makes sure that the back focal plane remains well positioned on the rear of the objective.
   - 6.4. Using the Epi preview guppy camera, move the illumination objective and the objective stage so that the center of the illumination focus is well positioned in the center of the epi camera (centered through the epi objective)
   - 6.5. Ensure that there is no obstruction to the objective from the sample chamber. If there is, it may be necessary to raise the stage, and also the Epi objective higher. Reevaluate the pathway of light through the illumination objective in case it needs to be angled differently after these changes.
   - 6.6. Carefully, raise the intensity of the laser and begin aligning through the detection pathway.
   - 6.7. Move the detection objective far away and use a laser paper to observe the position of the “X” focused beam in the back focal plane of the detection

objective. If it is off centered horizontally this is adjusted by the knob on the flip mirror. If it is off centered vertically, this is adjusted with small movements to the translation stage of the illumination objective.

6.7.1. If the illumination objective stage is moved, the epi objective stage will also be moved slightly to compensate for the focus shift.

6.8. Move the detection objective closer and the focus "X" will travel along the detection pathway. Move it to the mirror in the far top corner of the vertical mounting board. Adjust any centering by minimally moving the knobs on the flip mirror or translation stage of the illumination objective. Again, movements should be immediately compensated in the epi pathway so the focus between the three objectives continuously overlaps.

6.9. Continue moving the objective until it focuses well on the camera, and use the mirror knobs in the detection pathway to center where the detection and the translation stage of the camera to center the beam on the camera chip (as seen with the SPIM program camera)

6.10. Move the translation stage of the detection objective until the beam is the thinnest most focused on the camera. Draw a box around it.

6.11. Add the focus lens and readjust the translation stage of the detection objective until it is in focus.

6.12. Adjust the translational knobs to position the beam as it was centered in the drawn box.

6.13. Straighten the beam horizontally by adjusting the mirrors on the protruding arm. The outer knobs partner and the inner knobs partner. Minor adjustments can also be made on the flip mirror.

6.14. Change the acquisition mode to continuous z-scan without dithering the x-galvo. Only move the z-galvo and keep the objective stationary. This will move the sample plane through the detection objective. Use the stage translation on the flip mirror to straighten the illumination plane so that the sample plane is well focused in the detection objective plane.

6.14.1. Draw two long skinny boxes along the left and right ends of the single beam. The stack profile should show overlapped lines that sharply focus and defocus into a "v" shape (upside down)

6.14.2. Ensure that the Epi camera is still in focus and make minor adjustments to the epi objective position (Epi is less of a priority)

7. Piezo limits

7.1. Empty the sample chamber.

7.2. Carefully add the sample holder after there is no danger of referencing. DO NOT overtighten the sample holder into the piezo. It will damage the piezo.

7.2.1. If at any point the piezos start to make a screaming noise it is because they are physically inhibited. Use the Motion Console "jump to setting" feature to lower them away from the objectives. Lowering the z-piezo to around 9.5 will usually solve this problem but it may be necessary to move the x and y positioning piezos to ~8.8 positions. If they do not move, raise the stage with the objectives manually and use a block to keep the objectives far away from the piezo stages. DO

NOT try to physically remove the sample holder while screaming is still occurring. Turn off the piezos as soon as possible if they do not move freely under the motion console command. This will prevent physical damage to the stages.

7.3. Use clean lens paper and move it between the sample holder, objectives, and sample chamber as needed to determine the limits of the piezo stages.

7.4. Close the program and edit the piezo limits in the .ini file. Setting these limits after every major alignment will prevent damage to the piezos and objectives.

7.5. When exchanging sample or removing the sample holder, lower the piezo stages away from the objectives to avoid damaging them

8. Alignment with beads

8.1. Create a sample of fluorescent beads by sonicating them and then adding a droplet on a clean coverslip and allowed to adhere for ten minutes.

8.2. Add this coverslip to the sample holder by removing the sample holder, using tweezers, and replacing the sample holder.

8.3. Raise the piezo slowly so that the beads are in focus as is done during the daily alignment.

8.4. Use the z-stack scan with dithering and move the z-piezo and z-galvo together. If there is any crookedness to the point spread function adjust the angle of the detection pathway by moving the bead in one direction and correcting the alignment as follows.

8.4.1. Recenter with the mirror of the detection pathway.

8.4.2. Readjust the angle of the illumination so the bead is brightest

8.4.3. Refocus the detection objection translational stage

8.4.4. Move in one direction at a time until you are certain it is correct or incorrect

8.5. Using the XZ PSF acquisition mode to visualize how the cross section of the sample plane looks. This will show any crookedness of the illumination objective and it may be necessary to make small movements to the objectives stage height and angle into the illumination objective.

8.6. Using the z-stack acquisition, adjust the correction collar on the detection objective in order to remove any ring-like structure when focusing or defocusing.

9. Cylindrical Lenses

9.1. Add in the cylindrical lens pairs by working farther from the SLM to closest to the SLM. Place a T-shirt alignment tool in the cage area before the SLM. The white center line will be vertical.

9.2. In order to manage two sets of cylindrical lenses, prepare for the second and third cylindrical lenses to be rotated around one of the cage systems beams. This will prevent you from needing to remove the focused second cylindrical lens in order to add the third lens. The third will simply rotate in place. The other cage system beams can be unscrewed and moved into and out of the holes of the cylindrical lens holder and re-screwed to secure.

9.3. The first cylindrical lens is added and turned so that the single beam is stretched along the vertical center line.

9.4. Add the second cylindrical lens and remove the protective covering over the polarized beam splitting cube. Turn the cylindrical lens so that the stretched beam is still aligned with the white center line.
9.5. Then position the lens along the cage mounting to collimate the stretched beam. The height of the beam should be similar close to the PBS cube and farther away. To be certain of the focus, use the BFP guppy camera and observe that the lines of a square or hex pattern on the SLM are the thinnest.
9.6. Rotate the third cylindrical lens adapter into place and turn the lens as needed to align it with the center of the T-shirt tool.
9.7. Add the final cylindrical lens and rotate to the center line. Slide the last cylindrical lens as well. Again, ensure that the BFP guppy has the thinnest lines possible to focus.
9.8. Add dye to the sample chamber and observe that all Bessel beams along the SLM are in focus at the same time. Minor adjustments to the angle of the SLM pattern will correct any defocused beams, and minor adjustments to the final cylindrical lens with make sure the entire sample plane of illumination is orthogonal to the detection plane.

10. Final excitation pathway magnification and angle
    10.1. With a bead positioned in focus, move the y-position piezo a set amount and capture the position of the bead before and after. Do this approximately 5 times and consider the piezo movements to be exact.
    10.2. Calculate the difference in the pixel of highest intensity, and then compare it to the difference in the piezo position. This ratio will be the magnification factor and should be around 63X which would make one pixel dimension ~107nm.
    10.3. Angle can be determined by moving the piezo stage in X and observing the transition in the camera for several steps. With the magnification factor, this angle should be calculated ~29-33 degrees.
11. Multiple lasers
    11.1. To align the next laser channel, repeat the alignment through the lenses by using a moveable mirror and observing the position near and far.
    11.2. Use the T-shirt tool to center the beam through the lenses well and verify that there are no clipping patterns.
    11.3. Using only the translation stage on the prism or the knobs on the emission filter mount, adjust the position of the first diffraction beam through the AOTF and until the SLM. At this point it should be very parallel with the other laser channels.
    11.4. Minor adjustments can be programed in the galvo offset settings just like during daily point spread alignment protocol.

Bibliography

Aguilera-Gomez, A., & Rabouille, C. (2017). Membrane-bound organelles versus membrane-less compartments and their control of anabolic pathways in Drosophila. *Developmental biology*, 428(2), 310–317. https://doi.org/10.1016/j.ydbio.2017.03.029

Alberti S. (2017) Phase separation in biology. *Current Biology*, 27 (20) R1097-R1102. https://doi.org/10.1016/j.cub.2017.08.069

Alberti, S., Gladfelter, A., & Mittag, T. (2019). Considerations and Challenges in Studying Liquid-Liquid Phase Separation and Biomolecular Condensates. *Cell*, 176(3), 419–434. https://doi.org/10.1016/j.cell.2018.12.035

An, S., Jeon, M., Kennedy, E.L., & Kyoung, M. (2019). Phase-separated condensates of metabolic complexes in living cells: Purinosome and glucosome. *Methods Enzymol*, 628, 1-17.

An, S., Parajuli, P., Kennedy, E.L., & Kyoung, M. (2021). Multi-dimensional fluorescence live-cell imaging for glucosome dynamics in living human cells. *Methods in Molecular Biology (Multienzymatic Assemblies: Methods and Protocols)*. Pre-print.

Ausina, P., Da Silva, D., Majerowicz, D., Zancan, P., & Sola-Penna, M. (2018). Insulin specifically regulates expression of liver and muscle phosphofructokinase isoforms. *Biomedicine & pharmacotherapy = Biomedecine & pharmacotherapie*, 103, 228–233. https://doi.org/10.1016/j.biopha.2018.04.033

Avalos, J. L., Fink, G. R., & Stephanopoulos, G. (2013). Compartmentalization of metabolic pathways in yeast mitochondria improves the production of branched-chain alcohols. *Nature biotechnology*, 31(4), 335-341.

Banani, S. F., Lee, H. O., Hyman, A. A., & Rosen, M. K. (2017). Biomolecular condensates: organizers of cellular biochemistry. *Nature reviews. Molecular cell biology*, 18(5), 285–298. https://doi.org/10.1038/nrm.2017.7

Birsoy, K., Wang, T., Chen, W. W., Freinkman, E., Abu-Remaileh, M., & Sabatini, D. M. (2015). An essential role of the mitochondrial electron transport chain in cell proliferation is to enable aspartate synthesis. *Cell*, 162(3), 540-551.

Bolte, S., & Cordelières, F. P. (2006). A guided tour into subcellular colocalization analysis in light microscopy. *Journal of microscopy*, *224*(Pt 3), 213–232. https://doi.org/10.1111/j.1365-2818.2006.01706.x

Bonnet, S., Archer, S. L., Allalunis-Turner, J., Haromy, A., Beaulieu, C., Thompson, R., ... & Michelakis, E. D. (2007). A mitochondria-K+ channel axis is suppressed in cancer and its normalization promotes apoptosis and inhibits cancer growth. *Cancer cell*, 11(1), 37-51.

Brdiczka, D. G., Zorov, D. B., & Sheu, S. S. (2006). Mitochondrial contact sites: their role in energy metabolism and apoptosis. *Biochimica et biophysica acta*, *1762*(2), 148–163. https://doi.org/10.1016/j.bbadis.2005.09.007

Bu, P., Chen, K. Y., Xiang, K., Johnson, C., Crown, S. B., Rakhilin, N., Ai, Y., Wang, L., Xi, R., Astapova, I., Han, Y., Li, J., Barth, B. B., Lu, M., Gao, Z., Mines, R., Zhang, L., Herman, M., Hsu, D., Zhang, G. F., … Shen, X. (2018). Aldolase B-Mediated Fructose Metabolism Drives Metabolic Reprogramming of Colon Cancer Liver Metastasis. *Cell metabolism*, 27(6), 1249–1262.e4. https://doi.org/10.1016/j.cmet.2018.04.003

Bunt, G., & Wouters, F. S. (2004). Visualization of molecular activities inside living cells with fluorescent labels. *International review of cytology*, 237, 205–277. https://doi.org/10.1016/S0074-7696(04)37005-1

Cai, L., & Tu, B. P. (2012). Driving the cell cycle through metabolism. *Annual review of cell and developmental biology*, 28, 59–87. https://doi.org/10.1146/annurev-cellbio-092910-154010

Cassim, S., Vučetić, M., Ždralević, M., & Pouyssegur, J. (2020). Warburg and Beyond: The Power of Mitochondrial Metabolism to Collaborate or Replace Fermentative Glycolysis in Cancer. *Cancers*, 12(5), 1119. https://doi.org/10.3390/cancers12051119

Chen, J., Ding, L., Viana, M.P., Hendershott, M.C., Yang, R., Mueller, I.A., & Rafelski, S.M. (2018) The Allen Cell Structure Segmenter: a new open source toolkit for segmenting 3D intracellular structures in fluorescence microscopy images. *bioRxiv*, 491035; https://doi.org/10.1101/491035

Chen, B-C., Legant, W.R., Wang, K., Shao, L., Milkie, D.E., Davidson, M.W., Janetopoulous, C., Wu, X.S., Hammer III, J.A., Liu, Z., … & Betzig, E. (2014) Lattice light-sheet microscopy: Imaging molecules to embryos at high spatiotemporal resolution. *Science*, 346 (3208), https://doi.org/10.1126/science.1257998

Christofk, H. R., Vander Heiden, M. G., Wu, N., Asara, J. M., & Cantley, L. C. (2008). Pyruvate kinase M2 is a phosphotyrosine-binding protein. *Nature*, 452(7184), 181–186. https://doi.org/10.1038/nature06667

Corbet, C., Pinto, A., Martherus, R., de Jesus, J. P. S., Polet, F., & Feron, O. (2016). Acidosis drives the reprogramming of fatty acid metabolism in cancer cells through changes in mitochondrial and histone acetylation. *Cell Metabolism*, 24(2), 311-323.

De Santis, M. C., Porporato, P. E., Martini, M., & Morandi, A. (2018). Signaling Pathways Regulating Redox Balance in Cancer Metabolism. *Frontiers in oncology*, 8, 126. https://doi.org/10.3389/fonc.2018.00126

Deng, X., Wang, Q., Cheng, M., Chen, Y., Yan, X., Guo, R., Sun, L., Li, Y., & Liu, Y. (2020). Pyruvate dehydrogenase kinase 1 interferes with glucose metabolism reprogramming and mitochondrial quality control to aggravate stress damage in cancer. *Journal of Cancer*, 11(4), 962–973. https://doi.org/10.7150/jca.34330

Engelman, J. A., Chen, L., Tan, X., Crosby, K., Guimaraes, A. R., Upadhyay, R., ... & Wong, K. K. (2008). Effective use of PI3K and MEK inhibitors to treat mutant Kras G12D and PIK3CA H1047R murine lung cancers. *Nature medicine*, *14*(12), 1351-1356.

Feng, Y., Zhang, Y., Cai, Y., Liu, R., Lu, M., Li, T., Fu, Y., Guo, M., Huang, H., Ou, Y., & Chen, Y. (2020). A20 targets PFKL and glycolysis to inhibit the progression of hepatocellular carcinoma. *Cell Death & Disease*, 11(89), https://doi.org/10.1038/s41419-020-2278-6

Fogg, V. C., Lanning, N. J., & Mackeigan, J. P. (2011). Mitochondria in cancer: at the crossroads of life and death. *Chinese journal of cancer*, 30(8), 526–539. https://doi.org/10.5732/cjc.011.10018

French, J.B., Jones, S.A., Deng, H., Pedley, A.M., Kim, D., Chan C.Y., Hu, H., Pugh, R.J., Zhao, H., Zhang, Y., Huang, T.J., Fang, Y., Zhuang, X., and Benkovic, S.J. (2016) Spatial colocalization and functional link of purinosomes with mitochondria. *Science*, 12 (351), 733-737, https://doi.org/10.1126/science.aac6054

Giegé, P., Heazlewood, J. L., Roessner-Tunali, U., Millar, A. H., Fernie, A. R., Leaver, C. J., & Sweetlove, L. J. (2003). Enzymes of glycolysis are functionally associated with the mitochondrion in Arabidopsis cells. *The Plant cell*, 15(9), 2140–2151. https://doi.org/10.1105/tpc.012500

Ginger, M. L., McFadden, G. I., & Michels, P. A. (2010). Rewiring and regulation of cross-compartmentalized metabolism in protists. *Philosophical transactions of the Royal Society of London. Series B, Biological sciences*, 365(1541), 831–845. https://doi.org/10.1098/rstb.2009.0259

Goldin, N., Arzoine, L., Heyfets, A., Israelson, A., Zaslavsky, Z., Bravman, T., ... & Flescher, E. (2008). Methyl jasmonate binds to and detaches mitochondria-bound hexokinase. *Oncogene*, 27(34), 4636-4643.

Graham, J. W., Williams, T. C., Morgan, M., Fernie, A. R., Ratcliffe, R. G., & Sweetlove, L. J. (2007). Glycolytic enzymes associate dynamically with mitochondria in response to respiratory demand and support substrate channeling. *The Plant cell*, 19(11), 3723–3738. https://doi.org/10.1105/tpc.107.053371

Grasmann, G., Smolle, E., Olschewski, H., & Leithner, K. (2019). Gluconeogenesis in cancer cells - Repurposing of a starvation-induced metabolic pathway?. *Biochimica et biophysica acta. Reviews on cancer*, 1872(1), 24–36. https://doi.org/10.1016/j.bbcan.2019.05.006

Hanahan, D., & Weinberg, R. A. (2011). Hallmarks of cancer: the next generation. *Cell*, 144(5), 646-674.

Harmon, T. S., Holehouse, A. S., Rosen, M. K., & Pappu, R. V. (2017). Intrinsically disordered linkers determine the interplay between phase separation and gelation in multivalent proteins. *eLife*, 6, e30294. https://doi.org/10.7554/eLife.30294

Hinzpeter, F., Gerland, U., & Tostevin, F. (2017). Optimal Compartmentalization Strategies for Metabolic Microcompartments. *Biophysical journal*, 112(4), 767–779. https://doi.org/10.1016/j.bpj.2016.11.3194

Hu, H., Juvekar, A., Lyssiotis, C. A., Lien, E. C., Albeck, J. G., Oh, D., Varma, G., Hung, Y. P., Ullas, S., Lauring, J., Seth, P., Lundquist, M. R., Tolan, D. R., Grant, A. K., Needleman, D. J., Asara, J. M., Cantley, L. C., & Wulf, G. M. (2016). Phosphoinositide 3-Kinase Regulates Glycolysis through Mobilization of Aldolase from the Actin Cytoskeleton. *Cell*, 164(3), 433–446. https://doi.org/10.1016/j.cell.2015.12.042

Hu, J. W., Sun, P., Zhang, D. X., Xiong, W. J., & Mi, J. (2014). Hexokinase 2 regulates G1/S checkpoint through CDK2 in cancer-associated fibroblasts. *Cellular signalling*, 26(10), 2210–2216. https://doi.org/10.1016/j.cellsig.2014.04.015

Huang, B., Babcock, H., & Zhuang, X. (2010). Breaking the diffraction barrier: super-resolution imaging of cells. *Cell*, 143(7), 1047–1058. https://doi.org/10.1016/j.cell.2010.12.002

Hult, K., & Berglund, P. (2007). Enzyme promiscuity: mechanism and applications. *Trends in biotechnology*, 25(5), 231-238.

Hyman, A. A., Weber, C. A., & Jülicher, F. (2014). Liquid-liquid phase separation in biology. *Annual review of cell and developmental biology*, 30, 39–58. https://doi.org/10.1146/annurev-cellbio-100913-013325

Icard, P., Fournel, L., Wu, Z., Alifano, M., & Lincet, H. (2019). Interconnection between Metabolism and Cell Cycle in Cancer. *Trends in biochemical sciences*, 44(6), 490–501. https://doi.org/10.1016/j.tibs.2018.12.007

Israelsen, W. J., Dayton, T. L., Davidson, S. M., Fiske, B. P., Hosios, A. M., Bellinger, G., Li, J., Yu, Y., Sasaki, M., Horner, J. W., Burga, L. N., Xie, J., Jurczak, M. J., DePinho, R. A., Clish, C. B., Jacks, T., Kibbey, R. G., Wulf, G. M., Di Vizio, D., Mills, G. B., … Vander Heiden, M. G. (2013). PKM2 isoform-specific deletion reveals a differential requirement for pyruvate kinase in tumor cells. *Cell*, 155(2), 397–409. https://doi.org/10.1016/j.cell.2013.09.025

Jang, S., Xuan, Z., Lagoy, R. C., Jawerth, L. M., Gonzalez, I. J., Singh, M., Prashad, S., Kim, H. S., Patel, A., Albrecht, D. R., Hyman, A. A., & Colón-Ramos, D. A. (2021). Phosphofructokinase relocalizes into subcellular compartments with liquid-like properties in vivo. *Biophysical journal*, 120(7), 1170–1186. https://doi.org/10.1016/j.bpj.2020.08.002

Jeon, M., Kang, H. W., & An, S. (2018). A Mathematical Model for Enzyme Clustering in Glucose Metabolism. *Scientific reports*, 8(1), 2696. https://doi.org/10.1038/s41598-018-20348-7

Jiang, Y., Li, X., Yang, W., Hawke, D. H., Zheng, Y., Xia, Y., Aldape, K., Wei, C., Guo, F., Chen, Y., & Lu, Z. (2014). PKM2 regulates chromosome segregation and mitosis progression of tumor cells. *Molecular cell*, 53(1), 75–87. https://doi.org/10.1016/j.molcel.2013.11.001

Jin, M., Fuller, G. G., Han, T., Yao, Y., Alessi, A. F., Freeberg, M. A., Roach, N. P., Moresco, J. J., Karnovsky, A., Baba, M., Yates, J. R., 3rd, Gitler, A. D., Inoki, K., Klionsky, D. J., & Kim, J. K. (2017). Glycolytic Enzymes Coalesce in G Bodies under Hypoxic Stress. *Cell reports*, 20(4), 895–908. https://doi.org/10.1016/j.celrep.2017.06.082

Juette, M.F., Gould, T.J., Lessard, M.D., Mlodzianoski, M.J., Nagpure, B.S., Bennett, B.T., Hess, S.T., Bewersdorf, J. (2008) Three-dimensional sub-100nm resolution fluorescence microscopy of thick samples. *Nature Methods*, (5) 527-529.

Kalucka, J., Missiaen, R., Georgiadou, M., Schoors, S., Lange, C., De Bock, K., Dewerchin, M., & Carmeliet, P. (2015). Metabolic control of the cell cycle. *Cell cycle* (Georgetown, Tex.), 14(21), 3379–3388. https://doi.org/10.1080/15384101.2015.1090068

Kaplon, J., van Dam, L., & Peeper, D. (2015). Two-way communication between the metabolic and cell cycle machineries: the molecular basis. *Cell cycle* (Georgetown, Tex.), 14(13), 2022–2032. https://doi.org/10.1080/15384101.2015.1044172

Kastritis, P. L., & Gavin, A. C. (2018). Enzymatic complexes across scales. *Essays in biochemistry*, 62(4), 501–514. https://doi.org/10.1042/EBC20180008

Kohnhorst, C. L., Kyoung, M., Jeon, M., Schmitt, D. L., Kennedy, E. L., Ramirez, J., Bracey, S. M., Luu, B. T., Russell, S. J., & An, S. (2017). Identification of a multienzyme complex for glucose metabolism in living cells. *The Journal of biological chemistry*, 292(22), 9191–9203. https://doi.org/10.1074/jbc.M117.783050

Kojima, T., & Takayama, S. (2018). Membraneless Compartmentalization Facilitates Enzymatic Cascade Reactions and Reduces Substrate Inhibition. *ACS applied materials & interfaces*, 10(38), 32782–32791. https://doi.org/10.1021/acsami.8b07573

Lackner L. L. (2019). The Expanding and Unexpected Functions of Mitochondria Contact Sites. *Trends in cell biology*, 29(7), 580–590. https://doi.org/10.1016/j.tcb.2019.02.009

Lee, I. H., & Finkel, T. (2013). Metabolic regulation of the cell cycle. *Current opinion in cell biology*, 25(6), 724–729. https://doi.org/10.1016/j.ceb.2013.07.002

Lee, J.E., Cathey, P.I., Wu, H., Parker, R., & Voeltz, G.K. (2020) Endoplasmic reticulum contact sites regulate the dynamics of membraneless organelles. *Science*, 367 (6477), https://doi.org/10.1126/science.aay7108

Li, C., Sun, J., Qi, X., & Liu, L. (2015). NaCl stress impact on the key enzymes in glycolysis from Lactobacillus bulgaricus during freeze-drying. *Brazilian journal of microbiology : [publication of the Brazilian Society for Microbiology]*, *46*(4), 1193–1199. https://doi.org/10.1590/S1517-838246420140595

Li, P., Banjade, S., Cheng, H. C., Kim, S., Chen, B., Guo, L., Llaguno, M., Hollingsworth, J. V., King, D. S., Banani, S. F., Russo, P. S., Jiang, Q. X., Nixon, B.

T., & Rosen, M. K. (2012). Phase transitions in the assembly of multivalent signalling proteins. *Nature*, 483(7389), 336–340. https://doi.org/10.1038/nature10879

Li, X., Li, T., Liu, Z., Gou, S., & Wang, C. (2017). The effect of metformin on survival of patients with pancreatic cancer: a meta-analysis. Sci Rep 7: 5825.

Liemburg-Apers, D. C., Willems, P. H., Koopman, W. J., & Grefte, S. (2015). Interactions between mitochondrial reactive oxygen species and cellular glucose metabolism. *Archives of toxicology*, 89(8), 1209–1226. https://doi.org/10.1007/s00204-015-1520-y

Locasale, J. W., Grassian, A. R., Melman, T., Lyssiotis, C. A., Mattaini, K. R., Bass, A. J., Heffron, G., Metallo, C. M., Muranen, T., Sharfi, H., Sasaki, A. T., Anastasiou, D., Mullarky, E., Vokes, N. I., Sasaki, M., Beroukhim, R., Stephanopoulos, G., Ligon, A. H., Meyerson, M., Richardson, A. L., … Vander Heiden, M. G. (2011). Phosphoglycerate dehydrogenase diverts glycolytic flux and contributes to oncogenesis. *Nature genetics*, 43(9), 869–874. https://doi.org/10.1038/ng.890

Lopez, J., & Tait, S. (2015). Mitochondrial apoptosis: killing cancer using the enemy within. *British Journal of Cancer*, 112, 957 - 962.

Mamczur, P., Dus, D., & Dzugaj, A. (2007). Colocalization of aldolase and FBPase in cytoplasm and nucleus of cardiomyocytes. *Cell biology international*, 31(10), 1122–1130. https://doi.org/10.1016/j.cellbi.2007.03.029

Mamczur, P., Rakus, D., Gizak, A., Dus, D., & Dzugaj, A. (2005). The effect of calcium ions on subcellular localization of aldolase-FBPase complex in skeletal muscle. *FEBS letters*, 579(7), 1607–1612. https://doi.org/10.1016/j.febslet.2005.01.071

Martin, E. W., & Mittag, T. (2018). Relationship of Sequence and Phase Separation in Protein Low-Complexity Regions. *Biochemistry*, 57(17), 2478–2487. https://doi.org/10.1021/acs.biochem.8b00008

Mathupala, S. P., Ko, Y. H., & Pedersen, P. L. (2009). Hexokinase-2 bound to mitochondria: cancer's stygian link to the "Warburg Effect" and a pivotal target for effective therapy. *Seminars in cancer biology*, 19(1), 17–24. https://doi.org/10.1016/j.semcancer.2008.11.006

Mohammad, R. M., Muqbil, I., Lowe, L., Yedjou, C., Hsu, H. Y., Lin, L. T., Siegelin, M. D., Fimognari, C., Kumar, N. B., Dou, Q. P., Yang, H., Samadi, A. K., Russo, G. L., Spagnuolo, C., Ray, S. K., Chakrabarti, M., Morre, J. D., Coley, H. M., Honoki, K., Fujii, H., … Azmi, A. S. (2015). Broad targeting of resistance to apoptosis in cancer. *Seminars in cancer biology*, 35 Suppl(0), S78–S103. https://doi.org/10.1016/j.semcancer.2015.03.001

Mor, I., Cheung, E. C., & Vousden, K. H. (2011). Control of glycolysis through regulation of PFK1: old friends and recent additions. *Cold Spring Harbor symposia on quantitative biology*, 76, 211–216. https://doi.org/10.1101/sqb.2011.76.010868

Mowbray, J., & Moses, V. (1976). The tentative identification in Escherichia coli of a multienzyme complex with glycolytic activity. *European journal of biochemistry,* 66(1), 25–36. https://doi.org/10.1111/j.1432-1033.1976.tb10421.x

Pan, X., Wilson, M., McConville, C., Arvanitis, T. N., Griffin, J. L., Kauppinen, R. A., & Peet, A. C. (2013). Increased unsaturation of lipids in cytoplasmic lipid droplets in DAOY cancer cells in response to cisplatin treatment. *Metabolomics, 9*(3), 722-729.

Park, J. S., Burckhardt, C. J., Lazcano, R., Solis, L. M., Isogai, T., Li, L., Chen, C. S., Gao, B., Minna, J. D., Bachoo, R., DeBerardinis, R. J., & Danuser, G. (2020). Mechanical regulation of glycolysis via cytoskeleton architecture. *Nature,* 578(7796), 621–626. https://doi.org/10.1038/s41586-020-1998-1

Perkins, G. A., & Frey, T. G. (2000). Recent structural insight into mitochondria gained by microscopy. *Micron,* 31(1), 97-111.

Perkins, G. A., Renken, C. W., Frey, T. G., & Ellisman, M. H. (2001). Membrane architecture of mitochondria in neurons of the central nervous system. *Journal of neuroscience research,* 66(5), 857-865.

Pette, D., Luh, W., & Buecher, T. (1962). A constant-proportion group in the enzyme activity pattern of the Embden-Meyerhof chain. *Biochemical and biophysical research communications,* 7, 419–424. https://doi.org/10.1016/0006-291x(62)90327-3

Rambold, A. S., Cohen, S., & Lippincott-Schwartz, J. (2015). Fatty acid trafficking in starved cells: regulation by lipid droplet lipolysis, autophagy, and mitochondrial fusion dynamics. *Developmental cell, 32*(6), 678-692.

Rizzuto, R., Pinton, P., Carrington, W., Fay, F. S., Fogarty, K. E., Lifshitz, L. M., ... & Pozzan, T. (1998). Close contacts with the endoplasmic reticulum as determinants of mitochondrial Ca2+ responses. *Science*, *280*(5370), 1763-1766.

Roy, D., Sheng, G. Y., Herve, S., Carvalho, E., Mahanty, A., Yuan, S., & Sun, L. (2017). Interplay between cancer cell cycle and metabolism: Challenges, targets and therapeutic opportunities. *Biomedicine & pharmacotherapy = Biomedecine & pharmacotherapie,* 89, 288–296. https://doi.org/10.1016/j.biopha.2017.01.019

Ruff, K. M., Roberts, S., Chilkoti, A., & Pappu, R. V. (2018). Advances in Understanding Stimulus-Responsive Phase Behavior of Intrinsically Disordered Protein Polymers. *Journal of molecular biology*, 430(23), 4619–4635. https://doi.org/10.1016/j.jmb.2018.06.031

Sanzey, M., Abdul Rahim, S. A., Oudin, A., Dirkse, A., Kaoma, T., Vallar, L., Herold-Mende, C., Bjerkvig, R., Golebiewska, A., & Niclou, S. P. (2015). Comprehensive analysis of glycolytic enzymes as therapeutic targets in the treatment of glioblastoma. *PloS one,* 10(5), e0123544. https://doi.org/10.1371/journal.pone.0123544

Schmitt, D. L., & An, S. (2017). Spatial Organization of Metabolic Enzyme Complexes in Cells. *Biochemistry*, *56*(25), 3184–3196. https://doi.org/10.1021/acs.biochem.7b00249

Sednev, M. V., Belov, V. N., & Hell, S. W. (2015). Fluorescent dyes with large Stokes shifts for super-resolution optical microscopy of biological objects: a review. *Methods and applications in fluorescence,* 3(4), 042004. https://doi.org/10.1088/2050-6120/3/4/042004

Senda, T., & Yoshinaga-Hirabayashi, T. (1998). Intermembrane bridges within membrane organelles revealed by quick-freeze deep-etch electron microscopy. *The Anatomical record*, 251(3), 339–345. https://doi.org/10.1002/(SICI)1097-0185(199807)251:3<339::AID-AR9>3.0.CO;2-Q

Shakya, A., King, J.T. (2021) Modern optical microscopy methods to study biomolecular condensates. *Current Opinion in Colloid & Interface Science*, 52, https://doi.org/10.1016/j.cocis.2021.101421.

Shao, L., Kner, P., Hesper Rego, E., Gustafsson, M.G.L. (2011) Super-resolution 3D microscopy of live whole cells using structured illumination. *Nature Methods*, (8) 1044-1046.

Shimon Weiss (1999) Fluorescence spectroscopy of single biomolecules. *Science*, 283 (5408), https://doi.org/10.1126/science.283.5408.1676

Shiratori, R., Furuichi, K., Yamaguchi, M., Miyazaki, N., Aoki, H., Chibana, H., Ito, K., & Aoki, S. (2019). Glycolytic suppression dramatically changes the intracellular metabolic profile of multiple cancer cell lines in a mitochondrial metabolism-dependent manner. *Scientific reports*, 9(1), 18699. https://doi.org/10.1038/s41598-019-55296-3

Simonnet, H., Alazard, N., Pfeiffer, K., Gallou, C., Béroud, C., Demont, J., ... & Godinot, C. (2002). Low mitochondrial respiratory chain content correlates with tumor aggressiveness in renal cell carcinoma. *Carcinogenesis*, 23(5), 759-768.

Sivitz, W. I., & Yorek, M. A. (2010). Mitochondrial dysfunction in diabetes: from molecular mechanisms to functional significance and therapeutic opportunities. *Antioxidants & redox signaling*, 12(4), 537–577. https://doi.org/10.1089/ars.2009.2531

Srere P. A. (1987). Complexes of sequential metabolic enzymes. *Annual review of biochemistry*, 56, 89–124. https://doi.org/10.1146/annurev.bi.56.070187.000513

Sullivan, D. T., MacIntyre, R., Fuda, N., Fiori, J., Barrilla, J., & Ramizel, L. (2003). Analysis of glycolytic enzyme co-localization in Drosophila flight muscle. *The Journal of experimental biology*, 206(Pt 12), 2031–2038. https://doi.org/10.1242/jeb.00367

Sullivan, L. B., Gui, D. Y., Hosios, A. M., Bush, L. N., Freinkman, E., & Vander Heiden, M. G. (2015). Supporting aspartate biosynthesis is an essential function of respiration in proliferating cells. *Cell*, 162(3), 552-563.

Sun, X., Peng, Y., Zhao, J., Xie, Z., Lei, X., Tang, G. (2021) Discovery and development of tumor glycolysis rate-limiting enzyme inhibitors. *Bioorganic Chemistry*, 112 (104891). https://doi.org/10.1016/j.bioorg.2021.104891

Uversky, V.N. (2017) Intrinsically disordered proteins in overcrowded milieu: Membrane-less organelles, phase separation, and intrinsic disorder. *Current Opinion in Structural Biology*, 44: 18-30. https://doi.org/10.1016/j.sbi.2016.10.015

Vander Heiden, M. G. (2011). Targeting cancer metabolism: a therapeutic window opens. *Nature reviews Drug discovery*, 10(9), 671-684.

Vegliante, R., Di Leo, L., Ciccarone, F., & Ciriolo, M. R. (2018). Hints on ATGL implications in cancer: beyond bioenergetic clues. *Cell death & disease*, *9*(3), 1-10.

Wang, J., Tolan, D. R., & Pagliaro, L. (1997). Metabolic compartmentation in living cells: structural association of aldolase. *Experimental cell research*, 237(2), 445–451. https://doi.org/10.1006/excr.1997.3811

Warburg, O., Wind, F., & Negelein, E. (1927). THE METABOLISM OF TUMORS IN THE BODY. *The Journal of general physiology*, 8(6), 519–530. https://doi.org/10.1085/jgp.8.6.519

Webb, B. A., Dosey, A. M., Wittmann, T., Kollman, J. M., & Barber, D. L. (2017). The glycolytic enzyme phosphofructokinase-1 assembles into filaments. *The Journal of cell biology*, 216(8), 2305–2313. https://doi.org/10.1083/jcb.201701084

Wei, S. P., Qian, Z. G., Hu, C. F., Pan, F., Chen, M. T., Lee, S. Y., & Xia, X. X. (2020). Formation and functionalization of membraneless compartments in Escherichia coli. *Nature chemical biology*, 16(10), 1143–1148. https://doi.org/10.1038/s41589-020-0579-9

Weiss S. (2000). Shattering the diffraction limit of light: a revolution in fluorescence microscopy? *Proceedings of the National Academy of Sciences of the United States of America*, 97(16), 8747–8749. https://doi.org/10.1073/pnas.97.16.8747

Wilson J. E. (2003). Isozymes of mammalian hexokinase: structure, subcellular localization and metabolic function. *The Journal of experimental biology*, 206(Pt 12), 2049–2057. https://doi.org/10.1242/jeb.00241

Yang, W., Xia, Y., Hawke, D., Li, X., Liang, J., Xing, D., Aldape, K., Hunter, T., Alfred Yung, W. K., & Lu, Z. (2012). PKM2 phosphorylates histone H3 and promotes gene transcription and tumorigenesis. *Cell*, 150(4), 685–696. https://doi.org/10.1016/j.cell.2012.07.018

Zancan, P., Sola-Penna, M., Furtado, C. M., & Da Silva, D. (2010). Differential expression of phosphofructokinase-1 isoforms correlates with the glycolytic efficiency of breast cancer cells. *Molecular genetics and metabolism*, 100(4), 372–378. https://doi.org/10.1016/j.ymgme.2010.04.006

Zhang, B. B., Wang, D. G., Guo, F. F., & Xuan, C. (2015). Mitochondrial membrane potential and reactive oxygen species in cancer stem cells. *Familial cancer*, *14*(1), 19–23. https://doi.org/10.1007/s10689-014-9757-9

Zhang, M. X., Hua, Y. J., Wang, H. Y., Zhou, L., Mai, H. Q., Guo, X., Zhao, C., Huang, W. L., Hong, M. H., & Chen, M. Y. (2016). Long-term prognostic implications and therapeutic target role of hexokinase II in patients with nasopharyngeal carcinoma. *Oncotarget*, 7(16), 21287–21297. https://doi.org/10.18632/oncotarget.7116

Zhao, S., Xu, W., Jiang, W., Yu, W., Lin, Y., Zhang, T., ... & Guan, K. L. (2010). Regulation of cellular metabolism by protein lysine acetylation. *Science*, 327(5968), 1000-1004.

Zheng J. (2012). Energy metabolism of cancer: Glycolysis versus oxidative phosphorylation (Review). *Oncology letters*, 4(6), 1151–1157. https://doi.org/10.3892/ol.2012.928